Non-Single Quantum MRI: A Cardiac Modulated Rhythm in the Brain Tissue

David López Pérez

Doctor of Philosophy

Trinity College Institute of Neuroscience, University of Dublin, Trinity College

Supervisor: Dr. Christian Kerskens

Submitted to University of Dublin, Trinity College, April 2018

Declaration of Authorship

I, David López Pérez, declare that this thesis titled, 'Non-Single Quantum MRI: A Cardiac Modulated Rhythm in the Brain Tissue' and the work presented in it are my own. I confirm that:

- This thesis has not been submitted as an exercise for a degree at this or any other university and it is entirely my own work.
- Where any part of this thesis has previously been submitted for a degree or any other qualification at this University or any other institution, this has been clearly stated.
- Where I have consulted the published work of others, this is always clearly attributed.
- Where I have quoted from the work of others, the source is always given. With the exception of such quotations, this thesis is entirely my own work.
- I have acknowledged all main sources of help.
- I agree to deposit this thesis in the University's open access institutional repository or allow the library to do so on my behalf, subject to Irish Copyright Legislation and Trinity College Library conditions of use and acknowledgement.

Signed: _____

Date: _____

"Every man can, if he so desires, become the sculptor of his own brain."

Santiago Ramón y Cajal

Abstract

The relation between pressure and flow is one of the key concepts to understand brain dynamics. The Navier-Stokes equations state how changes in flow are related to changes in pressure. In addition, the Monro-Kellie hypothesis shows that the cranium and its constituents create a state of volume equilibrium, such that any increase in volume of one of the cranial constituents must be compensated by a decrease in volume of another. Normally, pressure measurements are carried out in large arteries or CSF compartments and therefore these measurements are not able to estimate fast dynamics and pressure related changes in the brain tissue.

For that reason, the focus of this work is to introduce a new MRI-based technique called Non-Single Quantum MRI. This technique investigates brain dynamics in a completely new fashion and adds additional information to the flow-pressure relationship. This work focuses on the interplay between the cardiac pressure wave and the tissue response to it.

This thesis explains how the brain tissue reacts to the cardiac pressure wave. This thesis describes the basis of the author's hypotheses on the origin of the MRI contrast mechanism of the cardiac induced oscillation and presents the results of several studies carried out throughout the PhD research period. These results show that the obtained cardiac modulated MRI signal cannot be explained by conventional MRI. A model is proposed to justify the foundation of this signal. Moreover, differences in the tissue response were found among separated groups such as young, old or depressed participants.

Finally the author provides guidelines and recommendations for future research on cardiac induced oscillations in the brain tissue. Further research paths are identified and a roadmap for future research in this area is defined.

Acknowledgements

Firstly, I would like to thank my supervisor **Dr. Christian Kerskens** for his advise and guidance throughout this study. His support and approachable nature made for a great working relationship, particularly during the most difficult moments and in the latter stages of this thesis.

Thanks also to **Sojo Joseph** for his availability and assistance setting up and the sequences and acquiring the data.

I would like to say big thanks to **Friedrich Wetterling** for the helpful discussions about Matlab mathematical data analysis.

I am grateful to all the people in Room 336 in the Lloyd Building for making this journey more enjoyable during these four years. Mainly **Hazel McCarthy, Dimitris Bolis, Giorgia DeMaria, Ana Calvo, Mark Byrne and Eric O'Hanlon** for reminding me there was a world outside the Ph.D. Special thanks to **Katie Crowley** for her proofreading and the lengthy conversations we shared.

I cannot forget about my friends **Carmen Dorado**, **Tamara Aguilera** and **Beatriz García**, who shared the last miles of this path with me.

On a different note, many people have been part of my daily life in Dublin and I am highly grateful to all of them.

On a personal note, I am eternally grateful to my parents **Francisco Javier and María Dolores**, and my sister **Verónica**, for supporting me during these four years and because they never stop believing in me.

My final words go to my wife **Edyta Stanaszek**, not only for her assistance proofreading this thesis but also for her daily moral support and for not arguing too much over my late nights in front of the computer.

Contents

List of Figures

Abbreviations

BOLD	**B**lood **O**xygenation **L**evel **D**ependent
BSS	**B**lind **S**ource **S**eparation
CA	**C**erebral **A**utoregulation
CBF	**C**erebral **B**lood **F**low
CPP	**C**erebral **P**erfusion **P**ressure
CT	**C**omputed **T**omography
DU	**D**oppler **U**ltrasound
DQ	**D**ouble **Q**uantum
DWT	**D**iscrete **W**avelet Transform
ECG	**E**ectro **C**ardio**G**ram
EEG	**E**ectro **E**ncephalo**G**ram
EPI	**E**co **P**lanar **I**maging
EVD	**E**xternal **V**entricular**D**rainage
FA	**F**lip **A**ngle
fMRI	**f**unctional **M**agnet **R**esonance **I**maging
FFT	**F**ast **F**ourier **T**ransform
FOV	**F**ield **O**f **V**iew
GRE	**GR**adient **E**cho
ICA	**I**nter **C**omponent **A**nalysis
ICP	**I**ntra **C**ranial**P**ressure
MAP	**M**ean **A**rterial blood **P**ressure
MDD	**M**ajor **D**epression **D**isease
MFDFA	**M**ulti**F**ractal**D**etrended **F**luctuation **A**nalysis
MRI	**M**agnet **R**esonance **I**maging

MT	**M**agnetisation **T**ransfer
NIRS	**N**ear **I**nfra**R**ed **S**pectroscopy
NMR	**N**uclear **M**agnetic **R**esonance
NOE	**N**uclear **O**verhauser**E**ffect
ONSD	**O**ptic **N**erve **S**heath **D**iameter
REST	**RE**gional **S**aturation **T**echnique
RF	**R**adio **F**requency
SL	**S**lice **T**hickness
SPM	**S**tatistical**P**arametric **M**apping
SQ	**S**ingle**Q**uantum
TCD	**T**rans**C**raneal **D**oppler
TE	**T**ime **E**cho
TPM	**T**wo **P**hoton **M**icroscopy
TR	**T**ime **R**epetition
UEPIS	**U**ltrafast **E**co **P**lanar **I**maging with **S**labs
ZQ	**Z**ero **Q**uantum

To my parents, my sister and specially my wife Edyta
for their support . . .

Part I

Introduction

Chapter 1

Introduction

During the last decades techniques such as Two Photon Microscopy (TPM), Near-Infrared Spectroscopy (NIRS), Magnetic Resonance Imaging (MRI), Doppler Ultrasound (DU) and many others have been used to study brain dynamics [1–9]. These techniques separately and in many cases combined have helped understand the changes in the cerebral vasculature, which is an important step to gain insights in brain dynamics and specifically cerebral auto-regulation (CA). The classical view of CA was described in 1959 by Lassen stating that the cerebral blood flow (CBF) is maintained constant across a wide range of mean arterial blood pressure (MAP) [10]. However, the development of new techniques has proved that the CBF in rest is unexpectedly dynamic [11, 12]. From this, the concept of dynamic CA was derived. Dynamic CA refers to the mechanisms that constrict and dilate vessels in order to keep the cerebral blood flow constant during dynamic perfusion pressure changes [13]. It can be separated into two different components: metabolic auto-regulation, which is the cerebrovascular response to changes in the partial pressure of carbon dioxide and changes depending on the necessity of the tissue, and pressure auto-regulation, resulting from changes in the cerebral perfusion pressure (CPP) and the MAP [14]. On one hand, strong interest exists in detecting the mediators of CA. For this purpose, current studies using techniques such Multi-Photon Microscopy are looking into the role of endothelial cells, astrocytes or pericytes in the constriction and dilation of the vessels during changes in

blood flow or brain pressure [15–17]. On the other hand, recent studies in pressure auto-regulation have shown that blood pressure is a complex variable which fluctuates across a wide range of time scales. Over a short scale, blood pressure resembles a pulsatile waveform with several characteristics that are governed by intrinsic cardiovascular properties and pulse wave reflection. At larger scales, it exhibits occurring trends and oscillations that span over minutes, hours or days [18]. This complexity suggests that pressure auto-regulation cannot be described using the classical numerical averages of blood pressure. Hence, more advanced models are often used. The Navier-Stokes equations are a set of 3 nonlinear equations that express the momentum of a fluid [19, 20]. These equations, widely used in MRI, show how changes in flow are related to changes in pressure [19]. Therefore, the understanding of pressure changes in the brain is key to comprehend changes in brain dynamics.

CPP is generally calculated by its relation with the MAP and the Intra-Cranial Pressure (ICP) [21, 22]. Several techniques are used to quantify the ICP which are typically divided between invasive and non-invasive techniques [21]. Invasive techniques such as External Ventricular Drainage (EVD) [23] and micro-transducers [24, 25] are considered the gold standard for measuring ICP because of its accuracy. However, the cost is elevated and there are risks of the patient suffering from haemorrhages during the procedure which makes these techniques less attractive. Therefore, non-invasive techniques such as Transcranial Doppler Ultrasonography (TCD) [26, 27], Optic Nerve Sheath Diameter (ONSD) [28, 29], Computer Tomography (CT) [30] and even MRI have been used [31]. In addition to the invasiveness of the process, these techniques are economically and computationally more efficient. However, they are not able to produce reliable results [21, 22].

All these aforementioned methods measure pressure in large arteries or CSF compartments and therefore are not able to measure fast dynamics and pressure related changes in the brain tissue. For that reason, the focus of this work is to introduce a new MRI-based technique called Non-Single Quantum MRI. It investigates brain dynamics in a completely new fashion and adds additional information to the flow-pressure relationship, which is important for understanding the dynamic

CA. The aim of this work involves the development of this new sequence as well as proposing a model to explain the origin of the Non-Single Quantum MRI signal. The signal is described in detail during variations of the different sequence parameters. The final step of this dissertation involves the application of this new method and future work based on its results is recommended.

1.1 Thesis Outline

The thesis is divided in four parts and is structured as follows:

Part II- Background

Chapter 2 - The MRI Signal. Chapter 2 reviews the MRI signal and the factors that affect it.

Chapter 3 - Data Analysis of Time Series. Chapter 3 introduces some of the most widely used tools in the field of Signal Analysis. Wavelet Analysis, Inter-Component Analysis, Fractals and Spectral Clustering are briefly discussed. The theory behind these methods is briefly outlined.

Part III - The Cardiac Induced Modulated MRI signal

Chapter 4 - Material and Methods. Chapter 4 outlines the material and methods used to study the cardiac induced modulated MRI signal.

Chapter 5 - A Cardiac Induced Modulated MRI Signal in the Brain Tissue. Chapter 5 presents the cardiac induced modulated signal profile and its relation to pressure changes. The corresponding results are examined.

Chapter 6 - MRI contrast mechanism of the cardiac induced modulated signal. Chapter 6 consists of the study of cardiac induced modulated MRI signal under variation of the MRI sequence parameters. The appearance, timing and factors affecting the signal are presented. The MRI contrast mechanism is described, as well as, the results are discussed.

Part III - Applications of the Non-Single Quantum MRI Sequence

Chapter 7 - Non-Single Quantum MRI in Ageing. Chapter 7 shows the analysis of the MRI signal and its variation through ageing. All results are analysed.

Chapter 8- Non-Single Quantum MRI in Major Depression Disorder. Chapter 8 presents the preliminary results of the cardiac induced modulated MRI signal applied to Major Depression Disorder (MDD) patients. The corresponding results are examined.

Chapter 9- Non-Single Quantum MRI in fMRI. Chapter 9 presents the preliminary results of the cardiac induced modulated signal applied to a fMRI study. The results concerning this chapter are discussed.

Chapter 10- Sleeping in the Magnet. A Case Study. Chapter 10 presents a case study of a participant who reported to have fallen asleep in the scanner. The results are briefly analysed.

Part IV - Conclusions

Chapter 11 - Conclusions and Further Research. Chapter 9 lists the contributions to the field highlighted in this thesis. The chapter presents recommendations and guidelines for future research using this sequence. It also suggests future studies that can shed light on brain dynamics and cerebral auto-regulation.

Part II

Theoretical Background

Chapter 2

Theoretical Background

2.1 The MRI signal

Let us consider a volume of tissue containing protons, where each proton has a spin vector of equal magnitude. First, all the spins are randomly oriented in all directions so that a vector addition of these spins produces a zero sum (Figure 2.1a), i.e., no net magnetisation [32]. If the tissue is placed inside a magnetic field B_0 the individual protons begin to rotate perpendicular to, or precess about, the magnetic field (Figure 2.1b). This precession is at a constant rate and occurs because of the interaction of the magnetic field with the spinning positive charge of the nucleus. The rate of frequency is proportional to the strength of the magnetic field and is expressed using the Larmor equation:

$$\omega_0 = \gamma B_0 \tag{2.1}$$

where γ is the gyromagnetic radio whose value for the proton is 42.6 MHz/T and B_0 is the static magnetic field in Tesla (T).

If a vector addition is done for all the spins inside the magnetic field, it will be found that in the direction perpendicular to B_0, no net magnetisation is found because the spins orientations are still randomly distributed and that in the direction

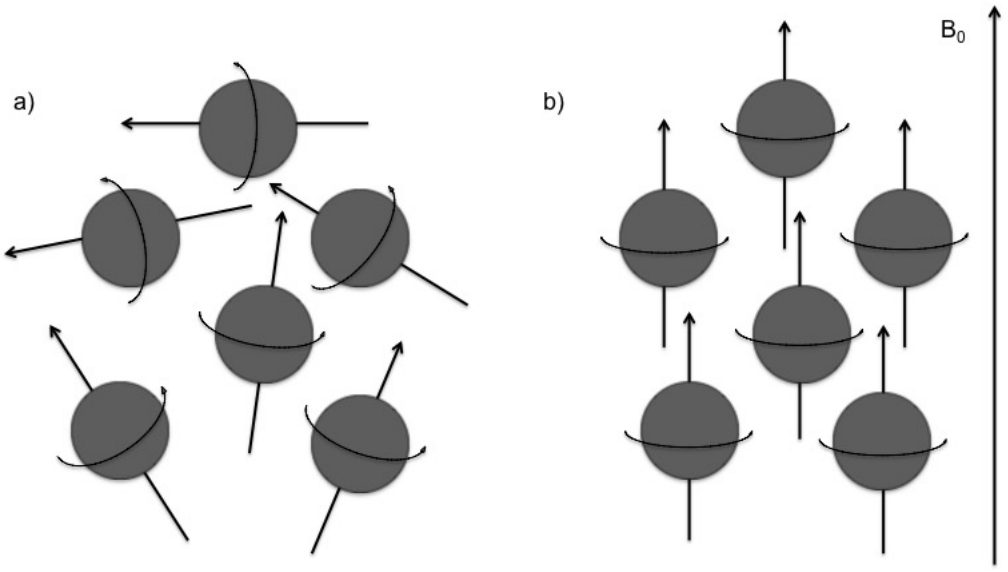

FIGURE 2.1: With no external magnetic field present spins rotate about their axes in random direction (a) In the presence of a magnetic field spins align parallel to the main magnetic field B_0 (b) [32].

parallel to the magnetic field, there is an orientation to the precessional axis of the proto n that causes a constant, non-zero interaction between the proton and B_0 [33]. This is known as Zeeman interaction and causes a difference in energy, ΔE, between protons aligned parallel to B_0 and protons aligned antiparallel to it (Figure 2.3) [33]. Due to the energy difference, a small excess of nuclei populate the lower state (Boltzmann statistic). This excess of spins accounts for the entire

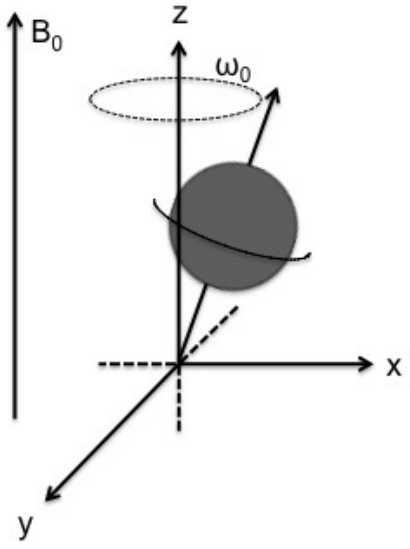

FIGURE 2.2: In the magnetic field, a proton precesses about the magnetic field and the x and y components vary with time at a frequency ω_0[33].

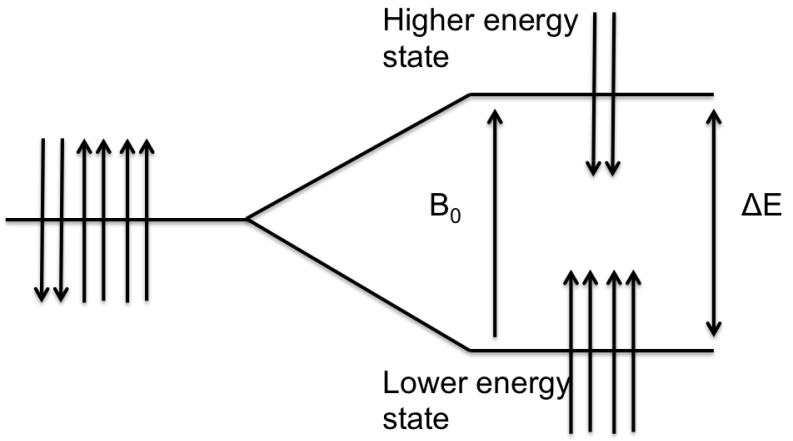

FIGURE 2.3: Zeeman diagram. In the absence of a magnetic field (left), a collection of protons will have the configuration of z components equal in energy so that there is no preferential alignment. In the presence of magnetic field (right), the spin up orientation is of lower energy and its configuration contains more protons than the higher energy, spin dow configuration. The difference in energy ΛE between the tow levels is proportional to B_0 [33].

net magnetisation, which is used in the NMR experiment [34]. For MR imaging, let us consider the bulk magnetization M that arises from all of the magnetic moments in a sample, which can be treated classically. The classical description is based on the Bloch equations [35]. For a static magnetic field in z-direction, the Bloch equations become:

$$\frac{M_x(t)}{dt} = -\gamma M_z(t) B_y(t) - \omega M_y(t) - \frac{M_x(t)}{T_2} \tag{2.2}$$

$$\frac{M_y(t)}{dt} = \gamma M_z(t) B_x(t) - \omega M_x(t) - \frac{M_y(t)}{T_2} \tag{2.3}$$

$$\frac{M_z(t)}{dt} = \gamma [M_x(t) B_y(t) - M_y(t) B_x(t)] - \frac{M_z(t) - M_0}{T_1} \tag{2.4}$$

where T_1 and T_2 are the longitudinal (spin-lattice) and transversal (spin-spin) relaxation rates, respectively and B is the magnet field. The MRI signal possesses its highest intensity right after the RF excitation pulses have been switched off and decreases together with the relaxation processes [33, 34].

2.1.1 Longitudinal and Transverse Relaxation

Each component in the brain tissue is characterised by its longitudinal, T_1, and its transverse, T_2, relaxation rates. The former is the process by which the net magnetisation, M, relaxes back to its original maximum value parallel to the M_0, while the latter is the process by which the transverse magnetisation dephase or decays [35]. As mentioned before, the tissues are characterised by different T_1 and T_2 values. First, T_1 refers to the interaction between the excited protons and the lattice (i.e. the molecules which make up the surrounding structure). The more static these excited protons are the better they exchange with the lattice, which leads to shorter T_1 values. The protons can be found in three states: free, bound to macromolecules by one bond or bound by two bonds [37]. On the one hand, free protons move a lot and therefore they possess a long T_1 and on the other hand, bound protons spend longer times interacting and therefore have shorter T_1. In the same fashion, T_2 is also strongly determined by molecular rotation speeds. Thus, if the molecular rotation is very fast, the influence of neighbours

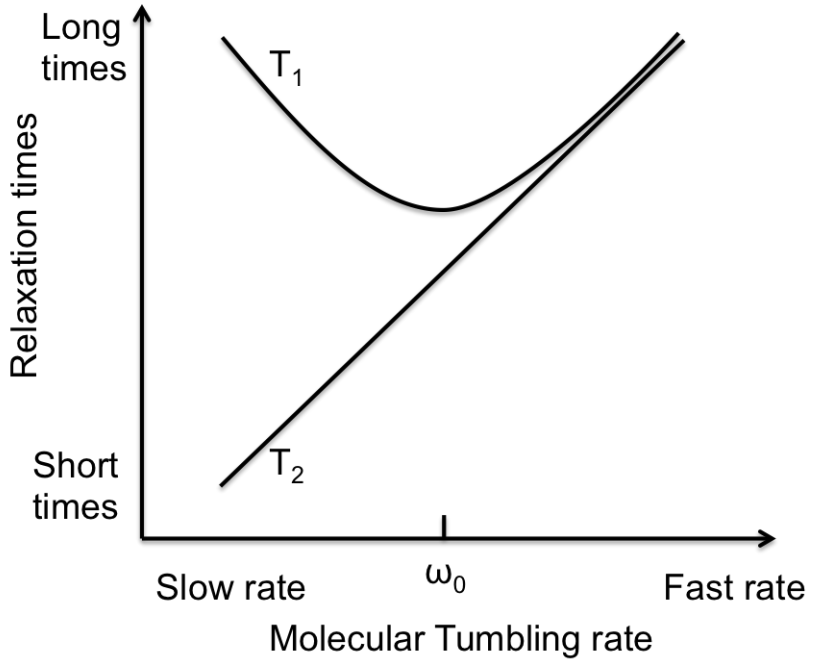

FIGURE 2.4: Variation of the relaxation rates with the tumbling rate, where ω_0 is the Larmor frequency. The molecular tumbling rate is slow for solids, large for molecules and bound protons and fast for liquids, small molecules and free protons [36]

will be rapidly changing. A proton pointing in one direction at one instant will be pointing an entirely different direction the next; overall, the effects will tend to cancel out. This is why free protons have a very long T_2 relaxation time, while solids or large molecules have a short T_2 relaxation because their motion is constrained. These relaxation rates are related to the rate of molecular movement or tumbling rate [38]. As molecules tumble they generate a fluctuating magnetic field to which protons in neighbouring molecules are subjected. Energy exchange is more favourable when this fluctuating magnetic field is close to the Larmor frequency (Fig. 2.4) [36].

The mathematical description of both relaxation times can be extracted from the Bloch equations in the absence of a RF pulse ($B_x = 0$ and $B_y = 0$)[39]

$$M_z(t) = M_0(1 - 2exp(\frac{-t}{T_1})) \tag{2.5}$$

$$M_x(t) = M_0 cos(\omega t) exp(\frac{-t}{T_2}) \tag{2.6}$$

$$M_y(t) = M_0 sin(\omega t) exp(\frac{-t}{T_2}) \tag{2.7}$$

It may be extracted from equation 2.5 that T_1 represents the time required by M to reach $1 - \frac{1}{e}$ or 63% of the original magnetisation (Fig. 2.5a). Accordingly, the T_2 relaxation process may be explained using equations 2.6 and 2.7. Thus, T_2 is

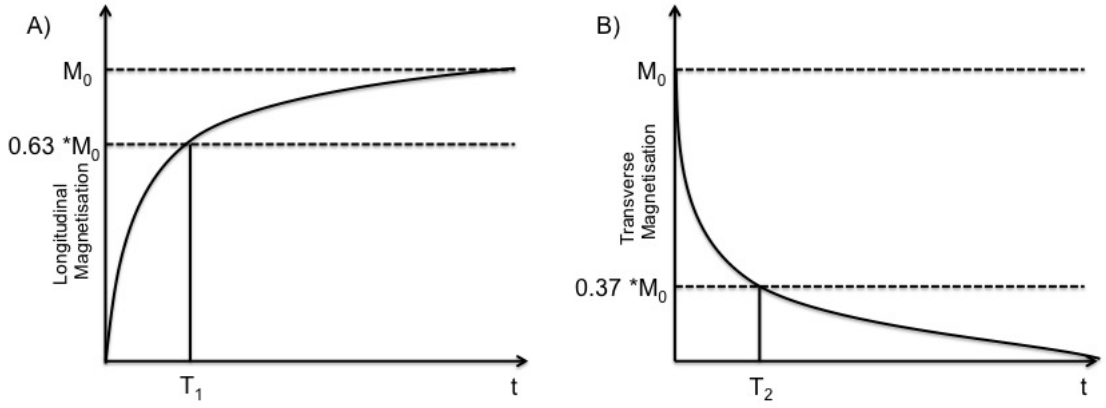

FIGURE 2.5: a) The recovery of longitudinal magnetisation (M_z) and its relation with the value of T_1 and b) The recovery of transverse magnetisation (M_{xy}) and its relation with the value of T_2 [36]

the time required by the transverse magnetisation to fall approximately $\frac{1}{e}$ or 37% of its original value (Fig. 2.5b). The longitudinal magnetisation always goes back to M_0 while the transverse magnetisation always decays to 0.

When an MRI sequence is applied the origin of the signal may vary depending on the values of the sequence. In other words, adjusting the sequence parameters might help to measure the different T_1 or T_2 components in tissue. However, this is a more complex process because the composition of a voxel is not homogeneous and a wide range of factors affect the signal. This heterogeneity has been traditionally explained using a 2 or 3 compartment model [40]. During the past decades, a more accurate understanding of the tissue components has been developed and this model has been expanded as shown in Figure 2.6 [37].

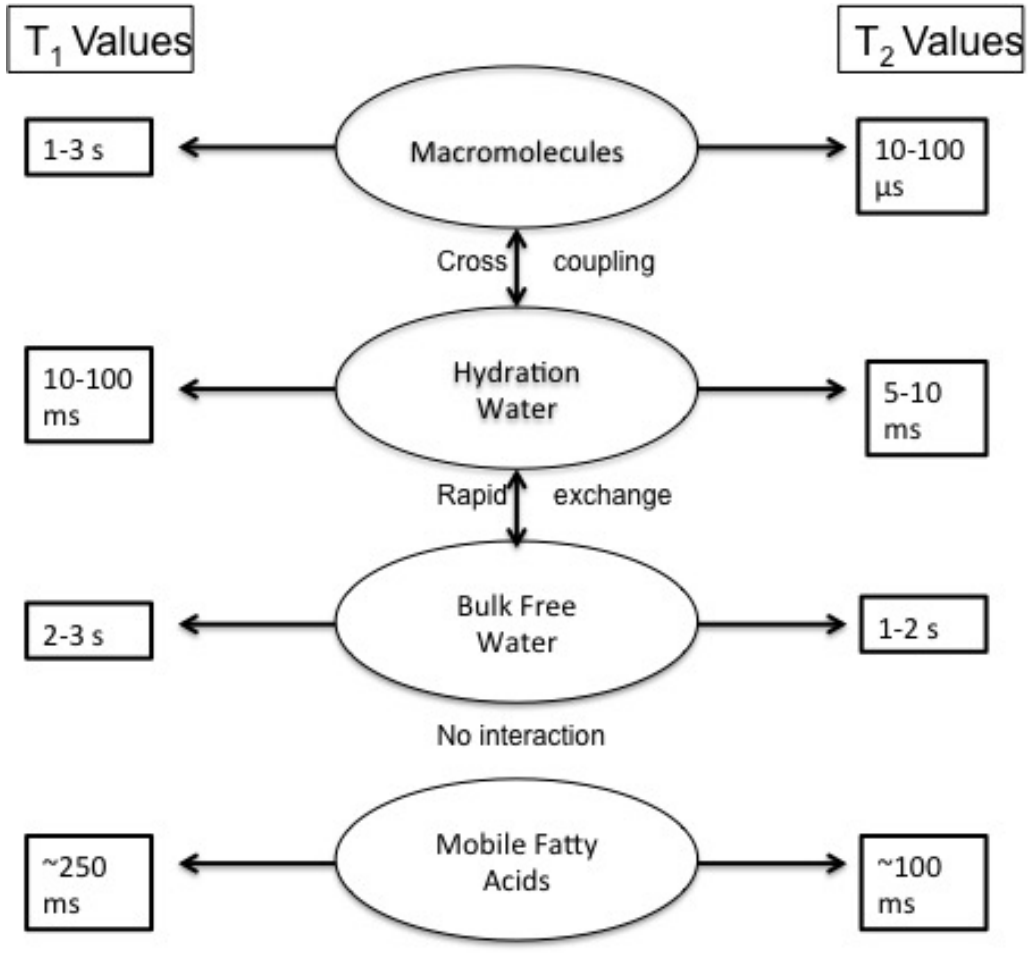

FIGURE 2.6: Compartment model which illustrates the different contributions from to T_1 and T_2 values [37].

In most tissues, and using the standard MRI sequences, protons generate most of the MRI signal. This water protons can be found either free or bound to other molecules. Under these conditions the T_1 and T_2 values differ dramatically. Bulk or free protons, which are the main component in brain tissue, have a $T_1 = 2 - 3$ seconds and a $T_2 = 1 - 2$ seconds. On the other hand, bound protons count with a $T_1 = 10 - 100$ ms and a $T_2 = 5 - 10$ msec. Nevertheless, water protons are not the only components and contributions from macromolecules and mobile fatty acids need to be included in the whole picture. Macromolecules have typically a T_1 close to bulk protons but a T_2 in the order of μseconds which makes them generally invisible in T_1 (due to its similarity to water) and T_2 (due to its extremely short values) maps. Lipids, however, possess a T_1 in the order of 250ms and a T_2 around 100ms.

2.1.1.1 T_2^* Relaxation

T_2^* relaxation refers to the decay in transverse magnetisation due to the spin-spin relaxation and magnetic field inhomogeneities. These inhomogeneities are introduced due to differences in magnetic susceptibilities among the different tissues,

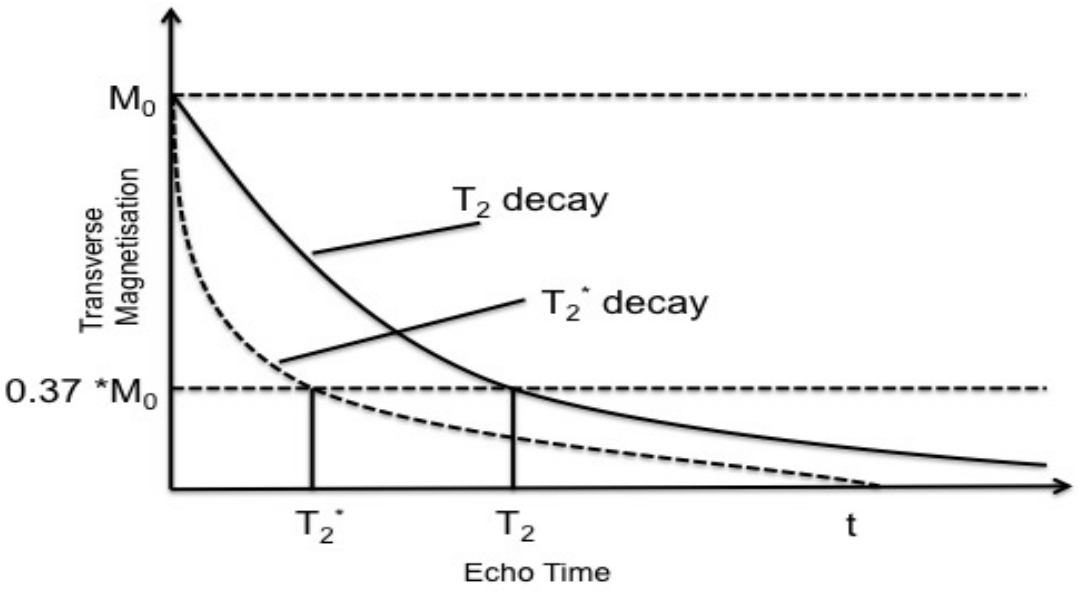

FIGURE 2.7: Graph shows T_2 and T_2^* relaxation curves. T_2^* is shorter than T_2 [41]

chemical shifts and gradients applied for spatial encoding [41]. This relaxation can be only observed with GRE sequences because spin-echo sequences use a refocusing RF pulse that corrects for these dephasing effects. Therefore, T_2^* relaxation is a combination of the T_2 relaxation and the additional relaxation $T_2^{'}$ caused by the magnetic field inhomogeneities [41]:

$$T_2^* = \frac{1}{T_2} + \frac{1}{T_2^{'}} \tag{2.8}$$

The introduction of the field inhomogeneities makes T_2^* shorter than the T_2 value (Fig. 2.7).

2.1.2 Sequence Parameter Influencing the MRI Signal

A pulse sequence is the measurement technique by which an image is acquired and contains the hardware instructions to gather the data in the desired manner.

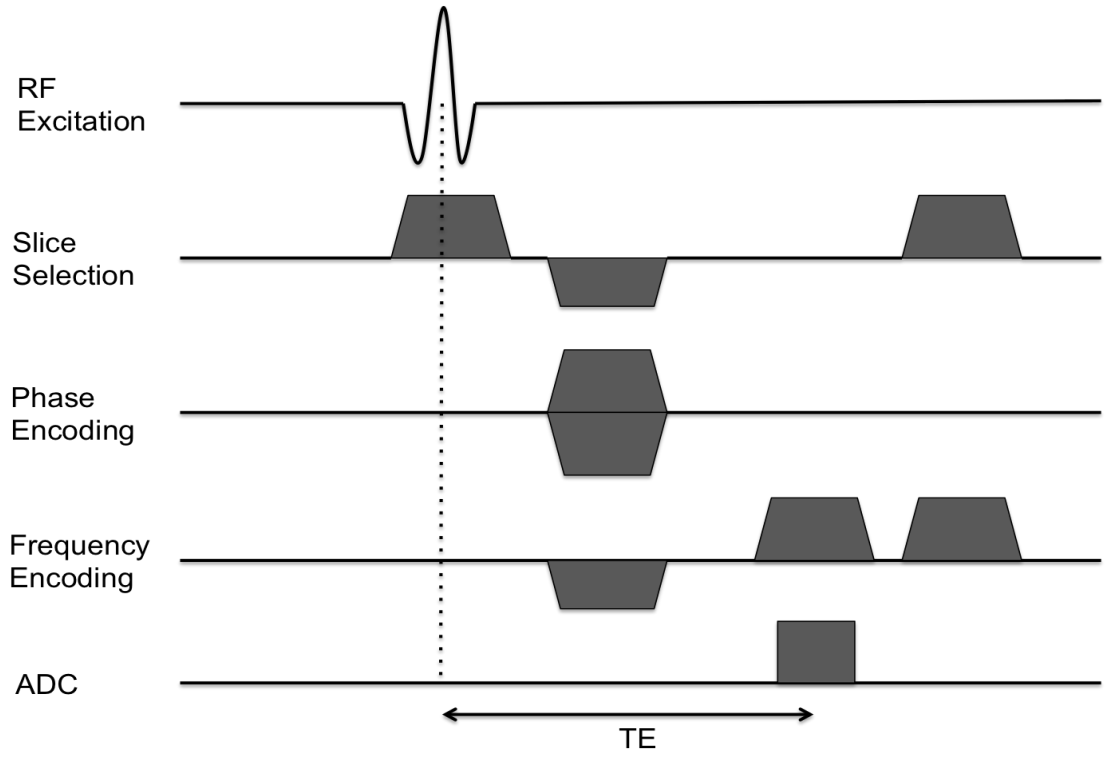

FIGURE 2.8: Example of a timing diagram corresponding to spoiled gradient-echo sequence [33].

These sequences are normally represented through the timing diagrams which are schematic representations of the basic steps performed by the different hardware components during sequence execution. An example may be seen in Figure 2.8. The first line represents the RF transmitter, then there are three lines, one for each gradient (i.e., slice selection, phase encoding and frequency encoding gradients) used in the sequence and finally the activity of the analog-to-digital converter is shown.

There are several imaging sequences in MRI (e.g., Gradient Echo sequences or Spin Sequences). Within those sequences numerous parameters can be altered causing changes in the origin of the signal. Here, the most relevant parameters will be briefly reviewed.

2.1.2.1 Repetition and Echo Time

The repetition time (TR) and echo time (TE) are the most basic parameters. The TR represents the time between the application of an RF excitation pulse and the start of the next RF pulse. Meanwhile, the TE, measured in ms, is the time between the excitation pulse and the echo (signal) maximum. The TR determines the amount of T_1 weighting contributing to the imaging. On the other hand, TE determines the amount of T_2 or T_2* weighting contributing to the imaging.

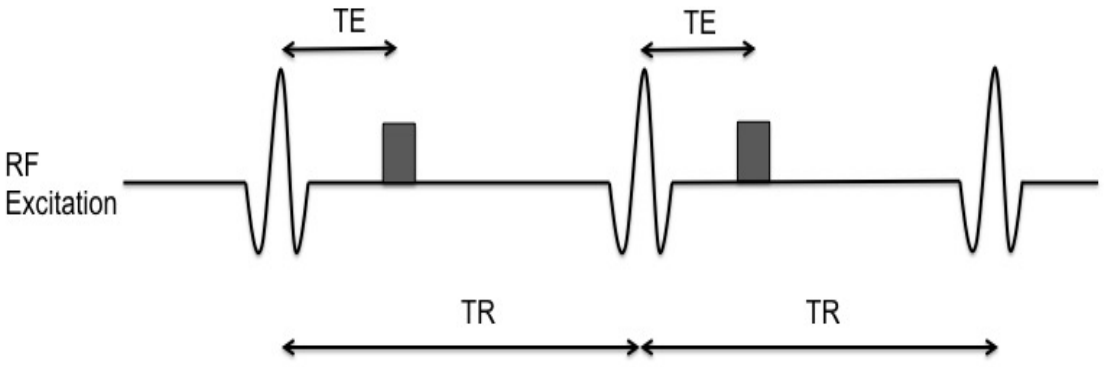

FIGURE 2.9: Example of an imaging sequence. The TR represents the time between consecutive points on a repeating train of pulses and echoes and the TE represents the time from the centre of the RF-pulse to the centre of the echo.

The combination of the both TE and TR may produce completely different contrasts [42]. For example, short TR and short TE generates a T_1-weighted image; short TR allows differences in longitudinal magnetisation to develop before the next 90 excitation pulse while short TE limits the T_2 effects. Long TR and long TE produces a predominantly T_2 -weighted image; where long TR allows recovery of longitudinal magnetisation (thus limiting T_1 effects) and long TE pronounces T_2 effects (Fig. 2.10a). A different type of image is produced at long TR and short TE. Long TR and short TE limit T_1 and T_2 effects, respectively. When this occurs, the signal is predominantly influenced by the proton density of the tissues [42].

Saturation Effects As aforementioned, short TR allows differences in T_1 to develop earlier. This situation, after the first TR pulse has been applied, when the next one comes only part of the longitudinal magnetisation has been recovered. Therefore, if we have a train of pulses with a very short TR, the signal will saturate those components with long T_1 and reach a steady state and the signal will arise from short T_1 components (Fig. 2.10b).

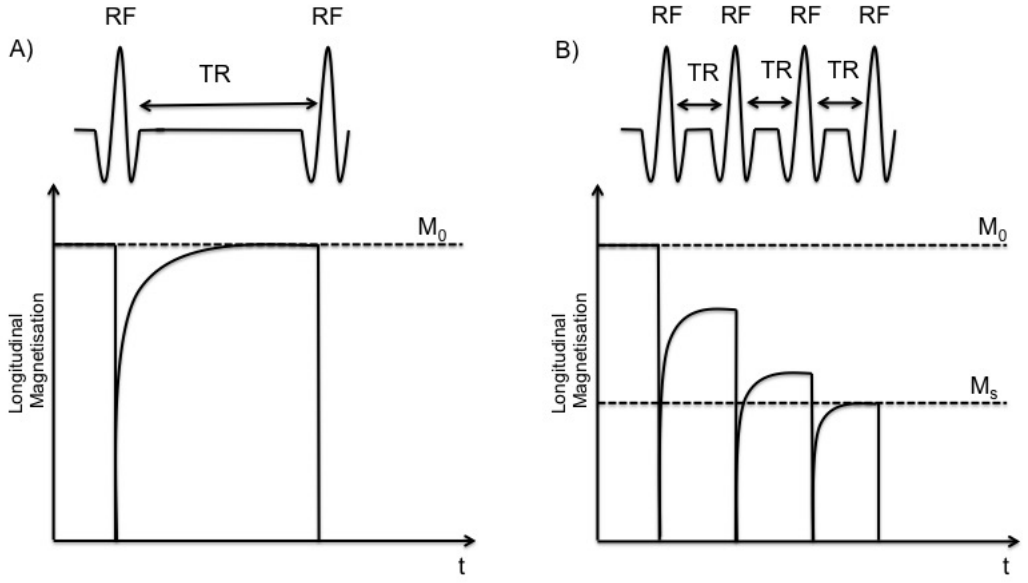

FIGURE 2.10: Long TR allows for full T_1 recovery (a), while short TR leads to saturation of the signal until a steady state has been reached (b).

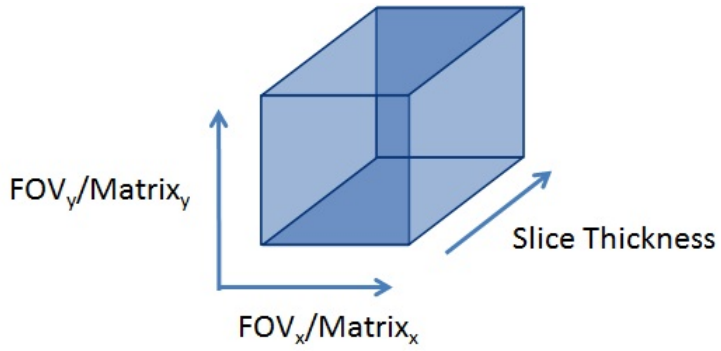

FIGURE 2.11: A voxel is a small volume element that represents the spatial resolution. It is determined by the pixel size (FOV/Matrix size in x and y direction) and the slice thickness.

2.1.2.2 Voxel Size

The voxel size determines the spatial resolution in three dimensions. The size of the voxel and therefore the resolution depends on matrix size, the field-of-view (FOV), and the slice thickness. The matrix size is the number of frequency encoding steps, in one direction; and the number of phase encoding steps, in the other direction of the image plane. Assuming everything else is constant, increasing the number of frequency encodings or the number of phase steps results in improved resolution (i.e., smaller voxel size). The FOV is the size of the area that the matrix of phase and frequency encoding cover. Dividing the FOV by the matrix size gives the in-plane voxel size; hence, increasing the FOV in either direction increases the size of the voxels and decreases the resolution. Decreasing the FOV improves the resolution. The depth of the voxel is determined by the slice thickness [32].

Although low spatial resolution can be achieved, the signal-to-noise (SNR) of the signal decreases proportionally. Therefore, sometimes it is better to increase the the voxel size in order to obtain a good MRI signal.

2.1.2.3 Flip Angle

The choice of the flip angle (FA) is important for obtaining both signal intensity as well as image contrast. It refers to the angle required to tip the magnetisation when a RF pulse is used. A partial FA (i.e., $<90°$) pulse creates an appreciable transverse

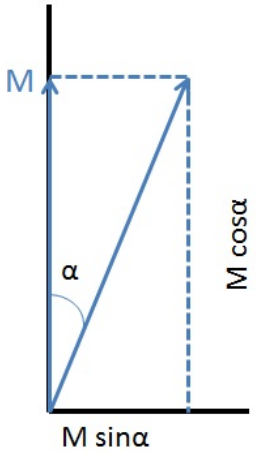

FIGURE 2.12: A flip angle pulse creates an appreciable transverse magnetisation. When a magnetisation vector M initially aligned with the z-axis is flipped by angle α, the transverse and longitudinal components of magnetisation after the flip will be $Msin\alpha$ and $Mcos\alpha$, respectively.

magnetisation while disturbing the longitudinal magnetisation only slightly (Fig. 2.12).

Sometimes when the TR is very short, the best flip angle to maximise signal can be quite small. This optimum angle is called the Ernst Angle [43]. This flip angle can be calculated from the equation:

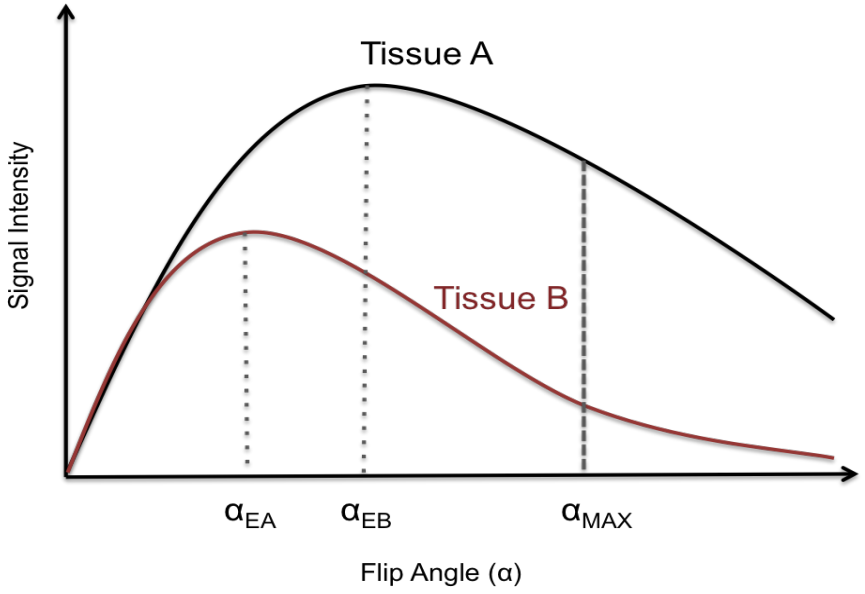

FIGURE 2.13: Example where two tissues have a maximum signal intensity at a relatively low FA, but the maximum tissue contrast is obtained at a higher FA [37].

$$\alpha_E = arcos(e^{\frac{-TR}{T_1}}) \tag{2.9}$$

However, depending on the sequence, we may choose a non-optimal flip angle that sacrifices maximal signal. The reason for this is that FA maximises the contrast between tissues that may be different to the FA that maximises the signal [37]. An example can be seen in Figure 2.13 where, although the tissues have a maximum signal intensity at a relatively low FA, the maximum tissue contrast is obtained at a higher FA.

2.2 Magnetisation Transfer

In conventional MRI, tissue contrast is generated from variations of the proton density and relaxation times of the free protons. In biological tissues, there are protons with free mobility and other restricted to macromolecules and membranes. Magnetisation Transfer (MT) imaging generates tissue contrast depending on the exchange between free and bound protons. This concept was first introduced by Wolff and Balaban in 1989 to describe the exchange rate between free and bound protons in kidneys and muscular tissue in vivo [44].

The MT concept has been extensively used in MRI, for instance, in Magnetic Resonance Angiography (MRA), where the signal contrast between the blood and the signal is enhanced using MT techniques [45, 46]; in mammography, where MT effects combined with fat suppression may be useful to study inflammatory carcinomas [47, 48]; or in the characterisation of white matter diseases in the brain such as Multiple Sclerosis [49–51]. Furthermore, some studies have reported incidental MT effects as those produced in Multi-slice EPI acquisition measurements [52, 53] or due to fat suppression pulses [54]. Others have additionally analysed the behaviour of the transition to steady state, which was proved to be useful for quantitative evaluation of the kinetic exchange of in vivo MT experiments [55].

2.2.1 Two-Pool Component Model

When a radio-frequency (RF) is applied, the excited protons release the absorbed energy to the free water, bound water, and macromolecules by mechanisms such dipole-dipole and chemical exchange interactions (Fig. 2.14). This MT effect has been traditionally described by a two-pool model. First, the so-called free pool consists of mobile protons in bulk water. These protons are characterised by a narrow spectral line (Δf = 10 - 100 Hz) and a relatively long transverse magnetisation (i.e., T_2 = 10/100 ms). Second, the so-called bound pool consists of protons attached to large macromolecules or cellular membranes. These protons are characterised by a very broad spectral line (Δf = 10 - 5 kHz) and a short transverse magnetisation (i.e., $T_2 < 0.1$ ms). MT is the interaction between the free protons and the bound protons and vice versa, resulting in an equilibrium situation characteristic for the type of tissue [57]. If the magnetisation is perturbed in either pool of protons (e.g. by RF excitation), energy is transferred between the free and bound protons leading to a difference in magnetisation, which will vary depending on the exchange between both pools at the excitation frequency [57, 58].

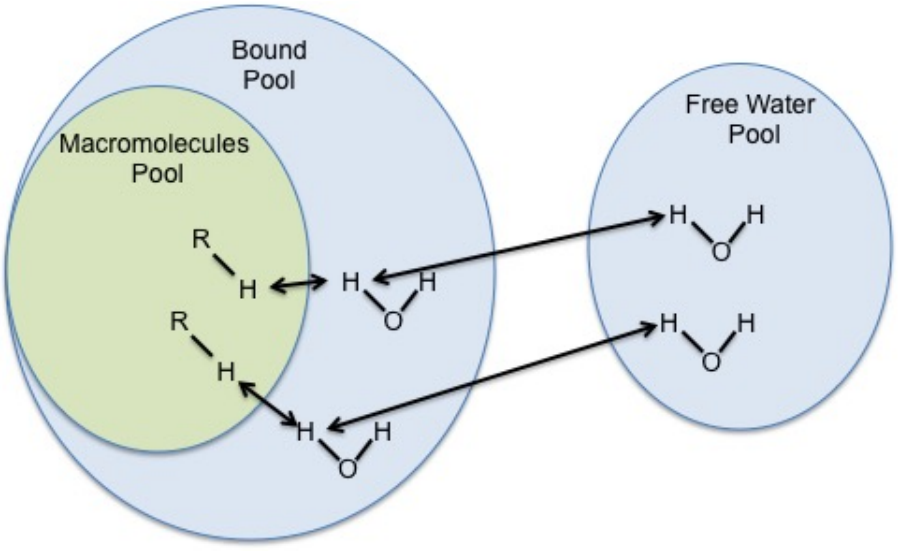

FIGURE 2.14: Molecular model for Magnetisation Transfer. In the first pathway, magnetisation is transferred via exchangeable protons or amine groups. In the second pathway, MT is mediated by hydration layer molecules [56].

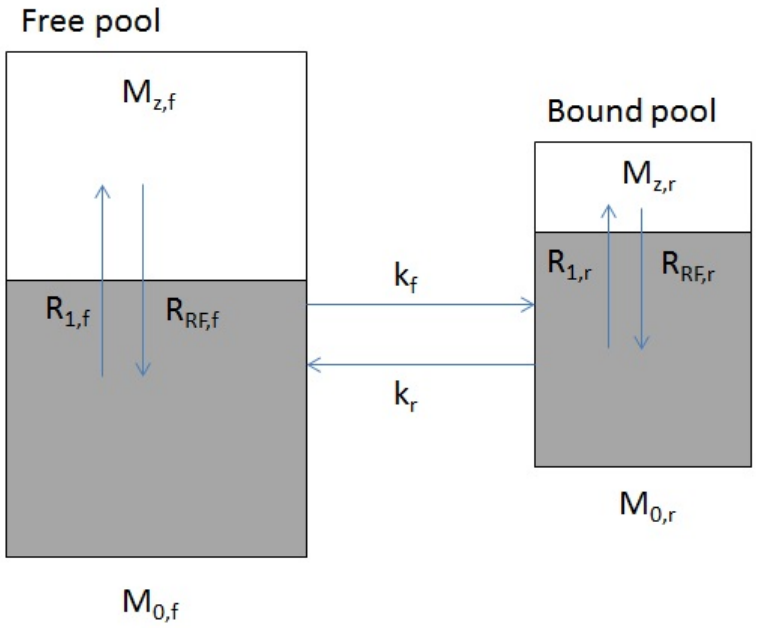

FIGURE 2.15: A two-pool model of magnetisation transfer exchange. The shaded region in each pool represents saturated spins. $R_{RF,f}$ and $R_{RF,r}$ represent longitudinal relaxation rates in liquid and macromolecular pools respectively. k_f and k_r denote magnetisation transfer exchange between the pools [57].

The two component model is represented in Figure 2.15. The shaded areas represent the saturated spins while the unshaded areas are the spins in the longitudinal orientation state. The equilibrium magnetisation of the free pool is given by $M_{0,f}$ and the equilibrium magnetisation of the restricted pool is given by $M_{0,r}$. The longitudinal relaxation is characterised by the relaxation rates of each pool, being R_1, f the relaxation rate of the free pool and R_1, r; whereas the rate of loss of longitudinal magnetisation due to off-resonance radiation is governed by $R_{RF,f}$ and $R_{RF,r}$. Finally, K_r represents the exchange rate from the free pool to the bound pool and K_f represents the exchange rate from the bound pool to the free pool.

There are two types of MT depending on the excitation frequency of the bound pool. When the RF pulse is around the central frequency it is called on-resonance MT and when it is outside the central frequency it is named off-resonance MT.

2.2.2 On-resonance MT

On-resonance MT has been studied as an alternative to off-resonance MT [59]. The on-resonance pulse consists of a series of block [60] or binomial pulses with a net flip angle of 0 [61, 62]. These binomial pulses can be considered as transparent to the free pool and the higher order binomial pulses, with a shorter duration and larger B1, will result in a larger transparent bandwidth [58].

2.2.3 Off-resonance MT

Off-resonance MT selectively deposits energy into the macromolecular pool, without affecting the water pool, using a specially designed RF pulse. This process is called selective excitation (Fig. 2.16). This RF pulse saturates the bound protons without affecting the free pool. To return to equilibrium, this energy would need to be transferred to nearby unaffected spins, some of which are in the free water pool. These free water protons would be driven to higher energy states, partially saturating and hence reducing the net magnetisation of the free water pool. If a second RF pulse were applied to the free water pool to generate an

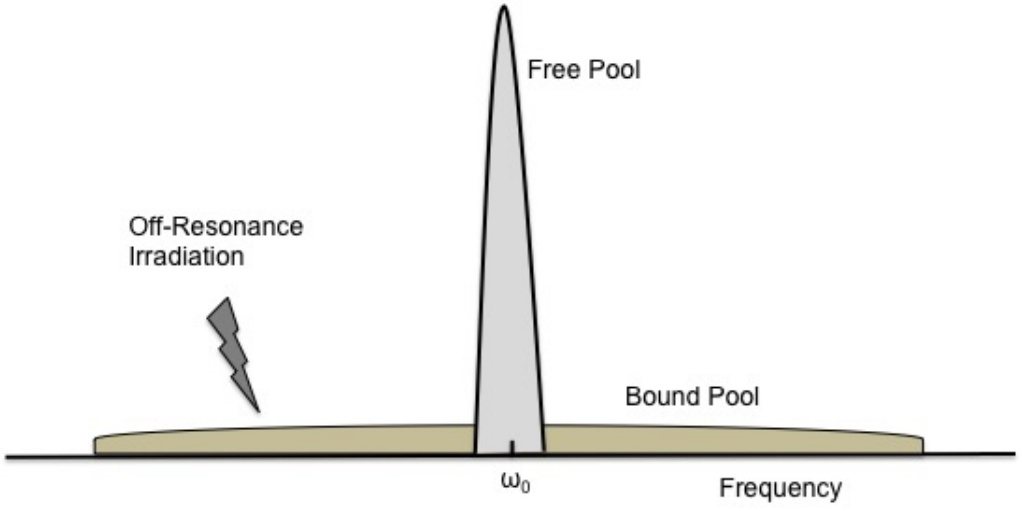

FIGURE 2.16: The spectral lines of free and the bound pools are both centered at the Larmor frequency f_0. The spectral line of the free protons is narrow in comparison to the line of the bound protons which is broad. Selective excitation of the bound pool by an off-resonance excitation leads to a variation in the magnetisation [58].

NMR signal, that signal would be smaller than it would have otherwise been due to magnetisation transfer of energy from the MT pulse [57, 58].

Since free protons are weakly coupled due to motional narrowing, the effect of an off-resonance irradiation is governed by the Bloch equations [57] as follows,

$$\frac{\partial M_f}{\partial t} = R_1 f(M_{0f} - M_f) - K_f M_f + K_r M_r \tag{2.10}$$

$$\frac{\partial M_r}{\partial t} = R_1 r(M_{0r} - M_r) - K_r M_r + K_f M_f \tag{2.11}$$

where $M_{0f}/M_{0r} \equiv K_f/K_r$.

2.3 Flow Effects in MRI

In the human body there are several levels of physiological flow present, for example, macroscopic flow (flowing blood in larger blood vessels), diffusion and perfusion (capillary flow) [63]. Flowing effects can be separated in two main types: Time-of-flight (TOF) effects and phase effects. TOF effects arise from the fact that flowing spins that were present at the start of the imaging sequence are no longer there at the end of it. Phase changes rise because different velocities lead to blood being affected by different field strengths, with consequent dephasing [36].

TOF effects are different depending on the sequence used (i.e., Spin-Echo or GRE sequences). In Spin Echo a 90° degree pulse is followed by a refocusing 180° pulse. If in the time between the 90° RF pulses and the 180° RF refocusing pulse the flowing spins have left the imaging slice, a signal washout will be produced. On the other hand, GRE does not use refocusing pulses, but repetitive RF pulses. In this case, if the blood affected by the first RF has left the slice and has been replaced by new flowing spins when the next RF pulses is applied, an increase of the signal will be observed (Fig. 2.17) [36, 38].

Phase effects appear because the stationary spins close to vessels have a different phase in comparison to the flowing spins inside the vessel. Within each voxel the

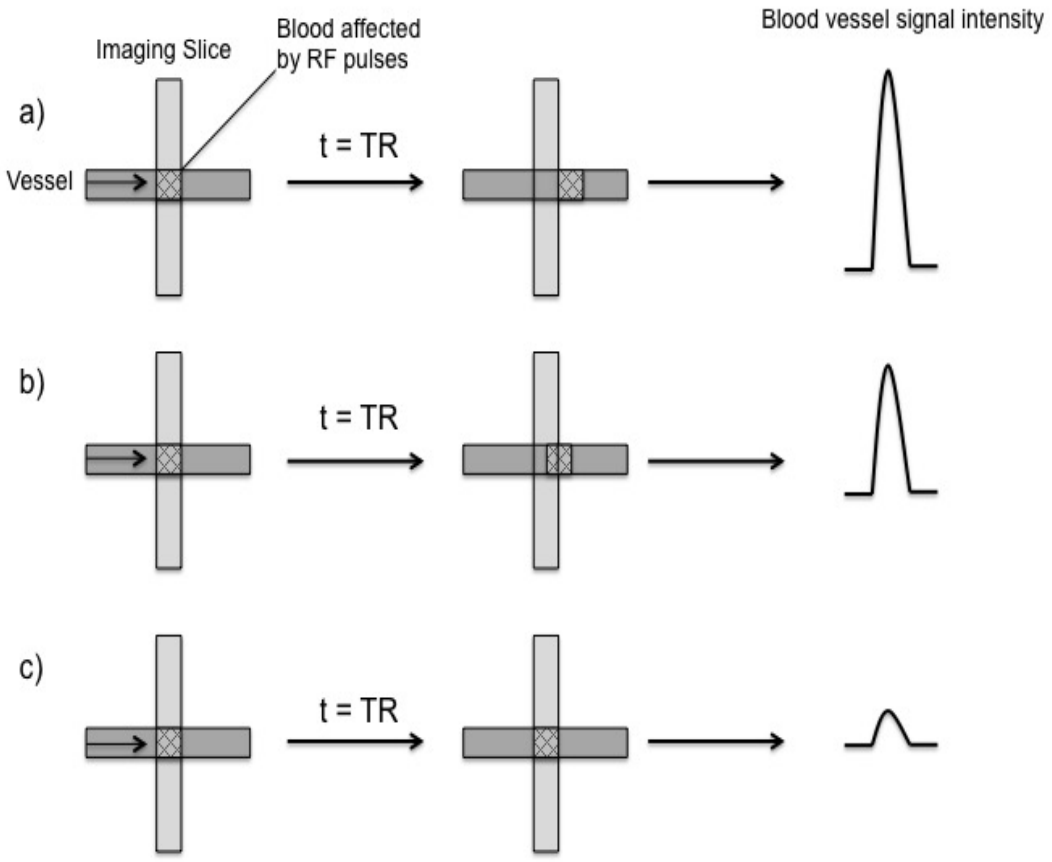

FIGURE 2.17: Inflow effect in gradient-echo imaging. The velocity of flow in the blood vessel is different for (a), (b), and (c). (a) Flow is fast in this case and at time t = TR, when the next RF pulse is applied, all the blood that had received the previous RF pulse has left the slice, and has been replaced by blood where the spins have a larger M_z component, as they have not previously been subject to any RF pulses. This means that a large signal is obtained. (b) Flow is slower than in (a) and as a result, not all the blood that received the previous RF pulse has left the slice, since only a proportion has been replaced by spins not previously subject to any RF pulses. This means that the signal from the blood vessel is strong, but not as strong as when all of the blood is replaced. When there is no flow (c), all the blood remains in the slice and is subject to repeated RF pulses which lowers the signal from the flow. [36].

range of different phase shifts can be large enough for complete dephasing to take place, leading to signal loss [36].

These inflow effects are normally unwanted and therefore techniques such REgional Saturation Technique (REST) are applied. Spins flowing through REST saturation bands are flipped into the transverse plane and then have their transverse magnetisation dephased by spoiler gradients. When these spins flow into the imaging slice they are already saturated and give zero signal [64].

2.4 The BOLD Effect

The BOLD (Blood Oxygenation Level Dependent) effect was first observed by Ogawa et al. in 1990 [65] proving in animals that variations in the MRI signal were present depending on the hemodynamic changes. A few years later the first studies using BOLD contrast were applied to humans by motor task [66] and visual perception task [67]. BOLD fMRI has emerged as the foremost method for visualising the vascular correlates of brain activity analysing, for instance, activation in motor cortex [68], visual cortex [69] or in the frontal cortex [70].

The BOLD signal is based on the paramagnetic properties of the deoxyhemoglobin (dHb). During activation the increase in the consumption of oxygen is accompanied by an increase in the fully oxygenated blood (Figure 2.18) [71]. The net effect is a local increase in oxyhemoglobin (diamagnetic) and a local decrease in deoxyhemoglobin (paramagnetic). Consequently, the decrease in paramagnetism leads to an increase in transversal relaxation rate $T2^*$ and $T2$, which can be detected

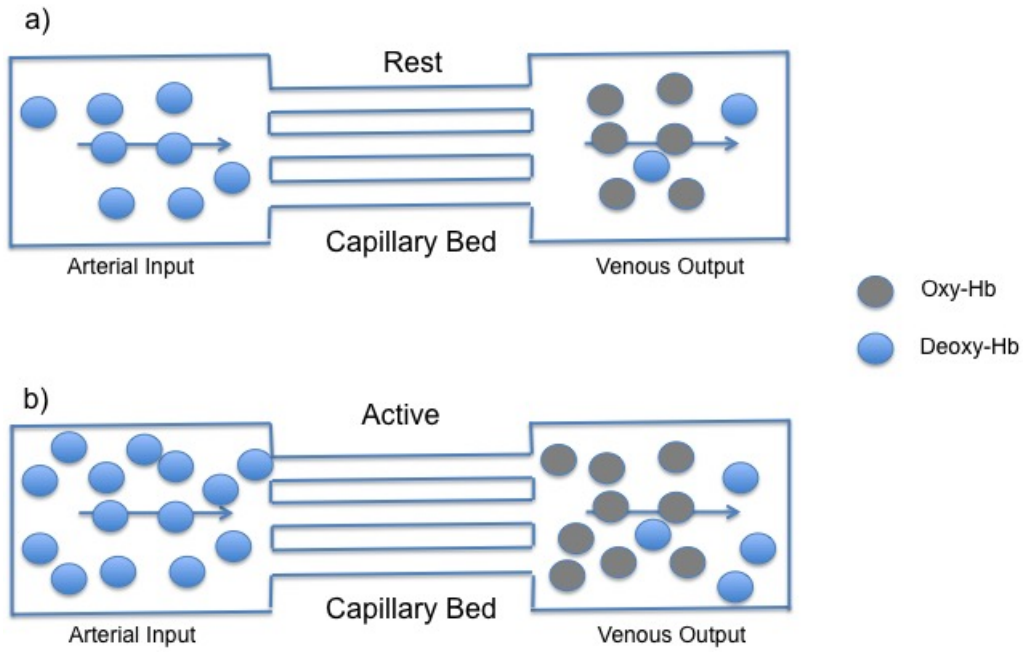

FIGURE 2.18: The origin of the BOLD effect. In activation (below) the overprovision of fully oxygenated blood leads to a reduction in dHb and an increase in local T_2^* in the draining veins compared with the rest condition (above) [38].

with optimised MRI sequences [39]. The optimum TE_{opt} to detect changes in the transversal relaxation is given by

$$TE_{opt} = ln(\frac{T_2c}{T_2a})(\frac{1}{T_{2a}} - \frac{1}{T_{2c}})^{-1} \tag{2.12}$$

where T_{2a} and T_{2c} denote the relaxation time during activation and control, respectively. For small changes in T_2/T_2^*, the optimum TE to maximise signal changes is found to be equal to T2/T2* [39, 72]. The assumption of small activation-induced changes in T_2/T_2^* might generally be true for the extravascular compartment, but for example the T_2 of venous blood can change significantly during activation. The consequence of this is that at lower field strengths, the T_2 of venous blood is longer than that of the tissue and its contribution to the BOLD signal change will be over-weighted. At very high field strengths T_2 is very short, and at the optimum TE for tissue the intravascular signal may be neglected [39, 72].

2.5 The Nuclear Overhauser Effect

Previously, it has been shown that molecular motion of two dipoles could create locally fluctuating magnetic fields resulting in T_1 and/or T_2 relaxation. This dipole-dipole interaction can be expanded with a quantum mechanical approach: the Nuclear Overhauser Effect (NOE). To understand the NOE let us considered a pair of protons AX, close in space but not J coupled to each other, whose spin difference is given by Δ [74]. At equilibrium, such a system has four energy states, corresponding to the $\alpha\alpha$, $\alpha\beta$, $\beta\alpha$ and $\beta\beta$ spin states (Fig. 2.19). There will be three kinds of transitions posible [75]:

- $\omega_{1A,X}$: the single quantum (SQ) transition probability that spin A will go from α to β (or viceversa) while the state of the spin X remains unchanged. Or the single quantum transition probability for spin X while A remains unchanged ($\alpha\alpha$/ $\alpha\beta$, $\alpha\alpha/\beta\alpha$, $\alpha\beta/\beta\beta$ and $\beta\alpha/\beta\beta$).

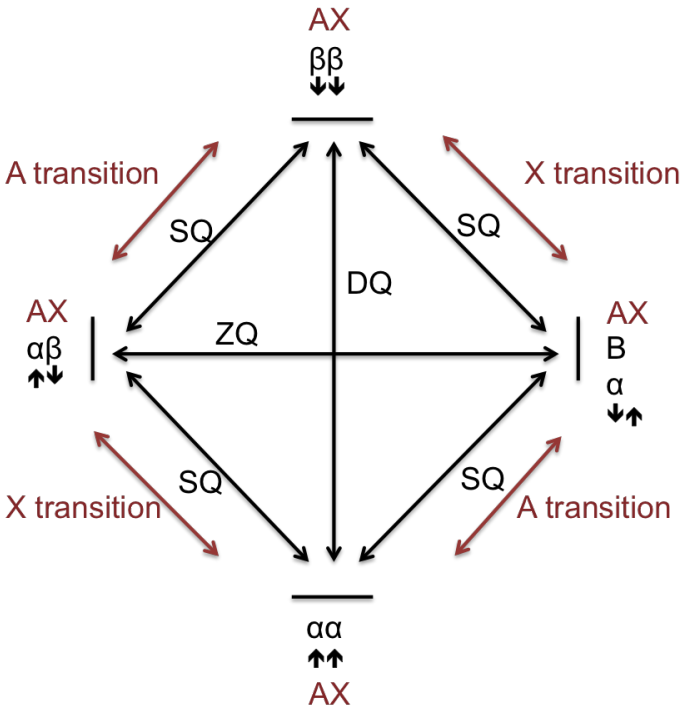

FIGURE 2.19: Quantum mechanical approach of the dipole and dipole interaction. The allowed single quantum (SQ) transitions and forbidden zero-quantum (ZQ) and double quantum (DQ) transitions are indicated.[73, 74].

- ω_2: the two quantum (DQ) transition probability for the two the spins to relax in the same direction ($\alpha\alpha/\beta\beta$ or $\beta\beta/\alpha\alpha$).

- ω_0: the zero quantum (ZQ) probability for a mutual spin flip ($\alpha\beta/\beta\alpha$ or $\beta\alpha/\alpha\beta$).

The frequencies of the ω_1 represent the Larmor frequencies of the two nuclei. The frequencies of the ω_0 transition is the difference in the chemical shifts of the two nuclei and is therefore relatively small. Finally, the frequencie of the ω_2 transition is the sum of the chemical shifts of the two nuclei and therefore it is approximately twice of the Larmor frequency [76].

When the X-transition is irradiated, the populations of the $\alpha\alpha$ and $\alpha\beta$ states get saturated, as do the $\beta\alpha$ and $\beta\beta$ states. The population difference across A must remain Δ, but the population across X must be zero. After the irradiation, relaxation occurs, therefore the difference in these two populations depends on the three possible relaxation processes. If $\omega_2 > \omega_1$, ω_0, then the $\beta\alpha/\beta\beta$ population

will tend to that of the $\beta\beta$ state, and the $\alpha\beta/\alpha\alpha$ states will tend that of the $\alpha\alpha$ state, hence there will be a larger population difference for the A transition (2Δ) than the equilibrium difference (Δ). Conversely, if ω_0 dominates, then the $\beta\alpha/\ \beta\beta$ will tend to the $\beta\alpha$ population, and the $\alpha\beta/\alpha\alpha$ will tend to the $\alpha\beta$ population, i.e., the population difference will tend to 0 [74–76].

The differential equations governing the population of the different states are the Solomon equations [77]:

$$\frac{d\Delta P_{\alpha\alpha}}{dt} = -(\omega_{1A} + \omega_{1X} + \omega_2)\Delta P_{\alpha\alpha} + \omega_{1A}\Delta P_{\beta\alpha} + \omega_{1X}\Delta P_{\alpha\beta} + \omega_2\Delta P_{\beta\beta} \quad (2.13)$$

$$\frac{d\Delta P_{\alpha\beta}}{dt} = -(\omega_0 + \omega_{1A} + \omega_2)\Delta P_{\alpha\beta} + \omega_0\Delta P_{\beta\alpha} + \omega_{1A}\Delta P_{\beta\beta} + \omega_{1X}\Delta P_{\alpha\alpha} \quad (2.14)$$

$$\frac{d\Delta P_{\beta\alpha}}{dt} = -(\omega_0 + \omega_{1A} + \omega_2)\Delta P_{\beta\alpha} + \omega_0\Delta P_{\alpha\beta} + \omega_{1A}\Delta P_{\alpha\alpha} + \omega_{1X}\Delta P_{\beta\beta} \quad (2.15)$$

$$\frac{d\Delta P_{\beta\beta}}{dt} = -(\omega_{1A} + \omega_{1X} + \omega_2)\Delta P_{\beta\beta} + \omega_{1A}\Delta P_{\alpha\beta} + \omega_{1X}\Delta P_{\beta\alpha} + \omega_2\Delta P_{\alpha\alpha} \quad (2.16)$$

where ω_0, $\omega_{1A,X}$ and ω_2 are the transition probabilities, $\Delta P_{\beta\beta}$, $\Delta P_{\alpha\beta}$, $\Delta P_{\beta\alpha}$ and $\Delta P_{\alpha\alpha}$, are the deviation of the population from the equilibrium of the $\beta\beta$, $\alpha\beta$, $\beta\alpha$ and $\alpha\alpha$ states respectively [77, 78].

Let us consider now the A_z and X_z, which represent the fluctuating longitudinal interactions for the spins A and X. Now utilising $< A_z > (t) = P_{\alpha\alpha}+P_{\alpha\beta}-P_{\beta\alpha}-P_{\beta\beta}$ and $< X_z > (t) = P_{\alpha\alpha} - P_{\alpha\beta} + P_{\beta\alpha} - P_{\beta\beta}$, it is possible to transform equations 2.13-16 into [77, 78]

$$\frac{d\Delta A_z(t)}{dt} = -(2\omega_{1A} + \omega_0 + \omega_2)\Delta A_z(t) - (\omega_2 - \omega_0)\Delta X_z(t) \quad (2.17)$$

$$\frac{d\Delta X_z(t)}{dt} = -(2\omega_{1X} + \omega_0 + \omega_2)\Delta X_z(t) - (\omega_2 - \omega_0)\Delta A_z(t) \quad (2.18)$$

where $\Delta A_z(t) =< A_z > (t) - A_z^0$ and $\Delta X_z(t) =< X_z > (t) - X_z^0$. A_z^0 and X_z^0 are the equilibrium magnitudes of the A_z and X_z respectively. The Solomon equations for a two spin system can be obtained by introducing the identifications $\rho_A = 2\omega_{1A} + \omega_0 + \omega_2$, $\rho_X = 2\omega_{1X} + \omega_0 + \omega_2$ $\sigma_{AX} = \omega_2 - \omega_0$ and into equation 2.19 and 2.20 [77, 78]

$$\frac{d\Delta A_z(t)}{dt} = -\rho_A \Delta A_z(t) - \sigma_{AX} \Delta X_z(t) \tag{2.19}$$

$$\frac{d\Delta X_z(t)}{dt} = -\rho_X \Delta X_z(t) - \sigma_{AX} \Delta A_z(t) \tag{2.20}$$

where rho_A and ρ_X are the auto-relaxation rate (i.e. spin-lattice relaxation rates) constants and σ_{AX} is the cross-relaxation term for exchange magnetisation between both spins [75].

2.5.1 Free Radicals

The NOE has been developed for dipole - dipole interactions of the water proton spins. However, the NOE can also be mediated by polarisation of bonding electrons in the molecule (i.e., free radicals). Free radicals are molecules present in the human body typically found at very low concentrations. Each electron possesses an intrinsic magnetic-dipole moment that arises from its spin [79]. In most systems electrons occur in pairs such that the net moment is zero. Hence, only species that contain one or more unpaired electrons possess the net spin moment necessary for suitable interaction with an electromagnetic field [80]. These free radicals unpaired electrons exhibit a quantum mechanical spin and therefore have a magnetic moment [81]. This means that an MRI signal can be generated in a way analogous to the detection of the proton spins in MRI. Although NMR and MRI are powerful approaches, the small energy splitting of the spin states even in a strong magnetic field results in low thermal polarisation of the nuclei (due to Boltzmann statistics), and only a fraction of the nuclei contribute to the observed

signal [81]. Therefore, several techniques have been developed to overcome this issue and quantify free radicals.

Electro Spin Resonance (ESR) uses continue irradiation to measure the resonance response of the unpaired electrons [80–82]. This response is measured by slowly increasing the strength of the magnetic field and when an ESR appears the combined effect of the unpaired electrons alters the electrical properties of the resonator and a reflected signal can be measured. The second one is the Chemical Induced Dynamic Nuclear Polarisation (CIDNP) which is based on electro-nuclear cross relaxation. It relies on the interplay between the nuclear-spin of radical pairs, modulated by the dynamics of inter-diffusion, and electron-spin reactivity of the pairs in the reaction pathway [83–86]. Finally, the Overhauser MRI (OMRI) appears, which consists of a double resonance technique that couples the advantages of MRI with the sensitivity of the aforementioned ESR. By saturating the EPR transition of the paramagnetic agent, the signal arising from the water spins is enhanced due to Overhauser Effect [87, 88]. This is due to the dipolar coupling existing between the unpaired electron of the free radicals and the proton of the water spins [88].

Chapter 3

Analysis of Time Series

3.1 Data Analysis of Time Series

The analysis of temporal signals has been always an issue in several disciplines like astronomy (e.g., array signals), geology (e.g., seismic signals), telecommunications (e.g., television signals) or medicine (e.g., biomedical signals). A broad spectrum of methods, not only in temporal but also in frequency domain, has been applied to interpret biomedical signals (e.g., MRI signals, electroencephalograms or electrocardiograms). For example, in MRI activation studies, time series data are more commonly investigated using Statistical Parametric Mapping (SPM) [89] or Analysis of Functional NeuroImages (AFNI) [90] to determine the regions under activation. Time series derived from electroencephalograms (EEGs) are evaluated using, for instance, topographic mapping [91] or transforming signal into ordinal patterns [92]. Another example could be electrocardiogram signals (ECGs), which may bear certain similarity to the signals obtained with the Non-single quantum MRI sequence. Analysis of ECGs includes classifying signals using beat-to-beat intervals, mean heart rate or standard deviation of the whole time series (i.e., Heart Rate Variation analysis) [93] or methods based on nonlinear or symbolic dynamics [94]. Between the wide range of possible methods, this thesis will focus on a few tools, which have been broadly used in different fields during recent decades to

analyse temporal signals: wavelet analysis, Inter-Component Analysis (ICA) and fractal analysis.

3.1.1 Wavelet Analysis

Wavelet transform is the frequency representation of a temporal signal at different time scales. The wavelet coefficients represent a measure of the similarity in the frequency content between a temporal signal and a chosen wavelet function [95]. A Wavelet is a wave-like oscillation with an amplitude that starts out at zero, increases and then decreases back to zero (Fig. 3.1). These functions are normally more concentrated on time and have a band-pass like spectrum, therefore acting as a dilated band-pass filter. The wavelet transform $X(a, b)$ is computed by convolution of signal, $x(t)$ and the scaled mother wavelet ,$\psi(t)$, as :

$$X(a,b) = \frac{1}{\sqrt{a}} \int_{-\inf}^{\inf} \psi(\frac{t-b}{a}) x(t) dt \tag{3.1}$$

where a is the scale that corresponds to frequency information, b is the translation parameter that relates the location of the wavelet function as it is shifted through the signal, giving the time information in the transform [96]. The scales are proportional to the radian frequency, and consequently, they are similar to the scales used in maps, meaning that high scales offer a non-detailed view of the signal and low scales correspond to a more detailed view. In terms of frequency, low frequencies (i.e., high scales) correspond to the non-detailed view, while high frequencies (i.e., low scales) correspond to a detailed information of a hidden pattern in the signal.

Once the mother wavelet is chosen, the computation starts with the scale a equal to 1 and the continuous wavelet transform is computed for all values of a. The procedure will continue for the increasing values of a, i.e., the analysis will start from high frequencies and proceed towards low frequencies. This first value of a

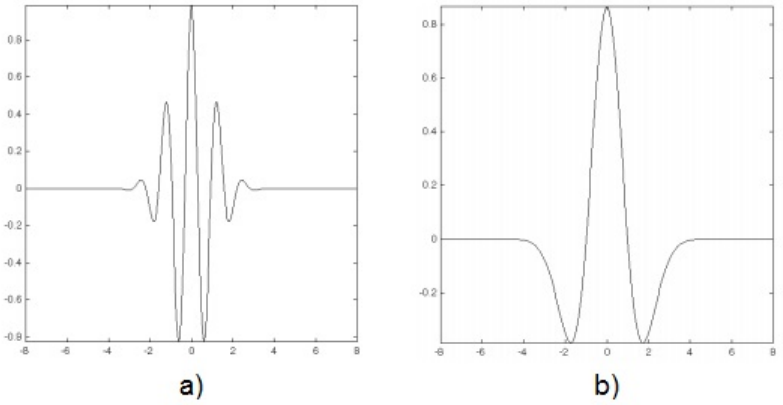

FIGURE 3.1: Mother wavelet examples. a. Morlet Wavelet and b. Mexican Hat Wavelet [96]

will correspond to the most compressed wavelet. As the value of a is increased, the wavelet will dilate.

The wavelet is placed at the beginning of the signal at the point which corresponds to t equal to 0. The wavelet function at a is multiplied by the signal and then integrated over all times. The result of the integration is then multiplied by the constant number $\frac{1}{\sqrt{a}}$. This multiplication is for energy normalisation purposes so that the transformed signal will have the same energy at every scale. The final result is the value of the transformation, i.e., the value of the continuous wavelet transform at time zero and scale $a = 1$. In other words, it is the value that corresponds to the point $b = 0$, $a = 1$ in the time-scale plane.

The wavelet at scale $s = 1$ is then shifted towards the right by τ amount to the location $t = b$, and the equation 3.1 is computed to get the transform value at $t = b$, $a = 1$ in the time-frequency plane. This procedure is repeated until the wavelet reaches the end of the signal at each scale.

3.1.1.1 Signal Denoising

One of the multiple applications of the DWT is the denoising of temporal signals in order to remove the noise in the signal [97–99]. Noise acts as an additive term that decreases the performance of visual and computerised analysis. The denoising

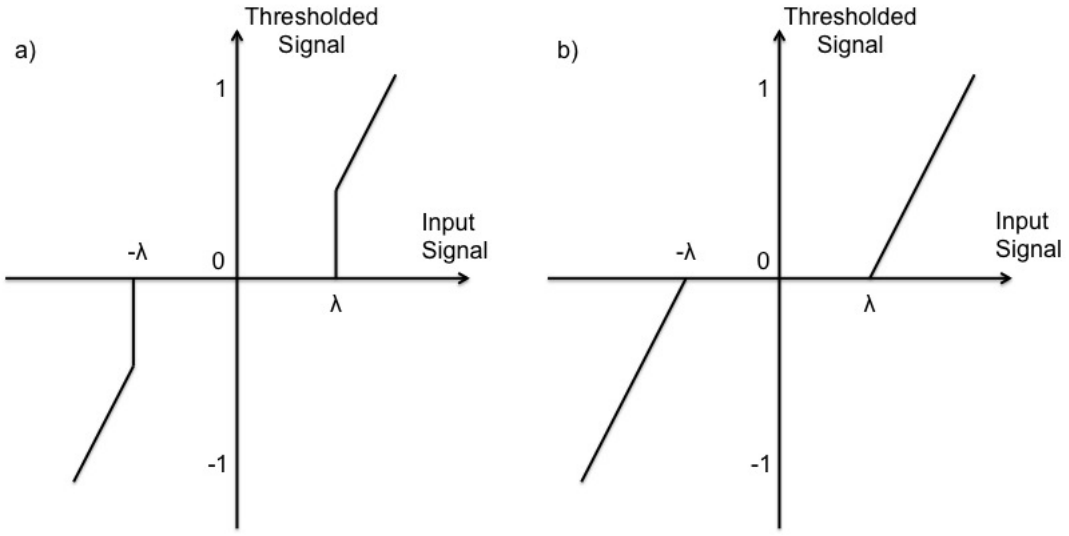

FIGURE 3.2: Representation of the hard(a) and soft (b) thresholding methods. λ represents the threshold value [103]

process consists of removing the noise without affecting the quality of the signal. A noisy signal, $x(t)$, might be described by

$$x(t) = y(t) + \sigma\epsilon(t) \tag{3.2}$$

where $y(t)$ is the noise free signal, $\epsilon(t)$ are independently normal variables and σ represents the intensity of the noise [100]. In equation 3.2 the noise is asssumed to be stationary, independent, zero-mean white Gaussian [101, 102]. This usual approach is to treat noise as a high frequency additive term that may be removed in frequency domain after applying an adequate filter to the Fourier transform of the signal. However, this leads to the loss of important signal information. In order to avoid this, methods like the DWT are used to denoise signals.

The wavelet signal denoising process is normally done in three steps:

- Apply the chosen wavelet to the noisy signal to produce the wavelet coefficients to the selected level. The choice of the mother wavelet is important because it can affect not only the noisy part of the signal but also its spectrum [103].

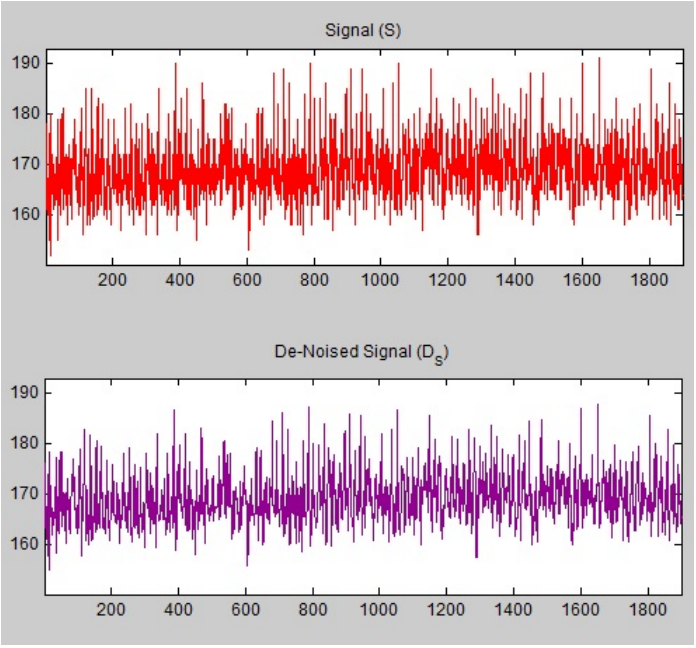

FIGURE 3.3: Example of an input noisy signal (a) and its correspondent de-noised signal after applying a two level decomposition using a Debauchy 5 mother Wavelet.

- Select a threshold limit and method to remove the noises. The idea of thresholding requires the estimation of the noise level which will be used to threshold the small coefficient assumed as noise. Since linear thresholding is only suitable for homogeneous signals, Donoho and Johnstone [104] proposed a nonlinear strategy for thresholding. The two main approaches are called hard and soft thresholding (Fig. 3.2). In the hard thresholding, the wavelet coefficient under a certain value λ is set to zero, whereas soft thresholding shrinks the coefficients with high amplitude towards zero.

- Inverse wavelet transform of the thresholded parameters to obtain the de-noised signal.

An example of the results after denoising the signal may be seen in Fig. 3.3 where the original and the denoised signals are shown.

3.1.2 Independent Component Analysis

Independent Component Analysis (ICA) is a computational method for finding underlying factors or components from multivariate (multi-dimensional) statistical data [105]. The problem of separating and estimating the original sources, without knowing signal characteristics and the source can be briefly expressed as problems related to Blind Source Separation (BSS). In BSS blind means that we do not know how the signals were mixed or how they were generated. Jutten and Heraulz [106] proposed that, in a artificial neural-network-like architecture the separation could be done by reducing redundancy between signals. This approach initially led to what is known as independent component analysis today. It was not until 1995, when Bell et al. [107] published a relatively simple approach to the problem named infomax, that many became aware of the potential of ICA. ICA is used today in many different applications, e.g., medical signal analysis [108], financial analysis [109], image processing [110] or in telecommunications [111]. In the last decade, ICA has been successfully applied to brain imaging studies, for example with data recorded at rest [112–114], or during natural stimulation [115, 116], and has received a lot of recent attention.

3.1.2.1 ICA Model

In the general ICA model, the sources are generated through a linear basis transformation, where additive noise might be present. The idea is to obtain the original sources, $s(t)$, from the measured signals, $x(t)$. These measured signals are a mixture of the original processes and they have to fulfill that they are spatially distributed so each signal is made from a different mixture of signals. The model can therefore be explained as:

$$x(t) = As(t) \tag{3.3}$$

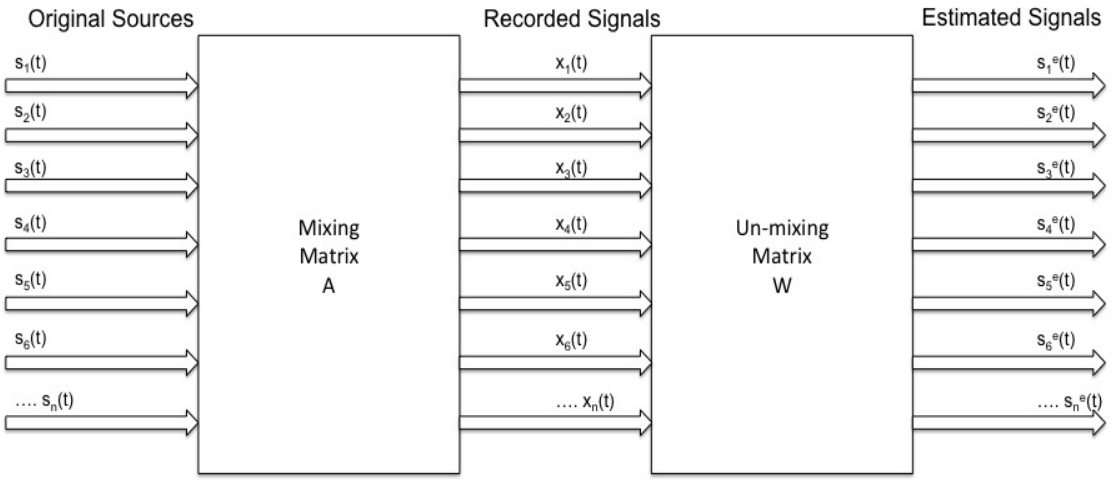

FIGURE 3.4: ICA model. The recorded signals are created from all the sources signals with the mixing matrix. The estimation of the separated sources signals is created by estimating the unmixing matrix [117].

where A is the unknown mixing matrix [105]. In order to estimate the sources we have to derive the unmixing matrix $W = A^{-1}$. We can thus estimate the independent sources as:

$$s^e(t) = Wx(t) \tag{3.4}$$

This ICA model can be summed up in Figure 3.4. The more accurate the unmixing matrix, the better estimation of the sources signals.

ICA is distinguished from other approaches of source separation in that it requires relatively few assumptions on the sources and on the mixing process. The assumptions are the following [117]:

- The sources are statistically independent.
- The components do not have Gaussian distribution. This is neccesary because ICA does not identify Gaussian sources and the sum of Gaussians would give a Gaussian. Since ICA is not able to identify a Gaussian all components will subsequently be non-Gaussian.
- The mixing matrix is irreversible. If it was not irreversible, then it would be impossible to be estimated.

As long as these assumptions are satisfied, then the sources may be estimated. Additionally, there are some ambiguities to be taken into account. The most important one is the permutation ambiguity which means that the order of the estimated independent components is not specified but this is inherent in the BSS [117]. Given no restrictions are applied in ICA, all possible permutations are equally valid.

3.1.2.2 ICA Preprocessing

There are a few steps that are commonly used prior to the ICA analysis. These effects are centering and whitening [105, 117]. An observed signal is centred by subtracting its mean vector $m = Ex$ so

$$x_c = x - m \tag{3.5}$$

By performing this we can assume a zero mean [105]. Once the unmixing matrix has been calculated, the independent components can be then estimated as:

$$s^e(t) = W(x_c(t) + m) \tag{3.6}$$

Whitening involves linearly transforming the observation vector such that its components are uncorrelated and have unit invariance [105, 108]. Let x_w be the whitened vector which satisfies the following equation:

$$Ex_w x_w^T = I \tag{3.7}$$

where $Ex_w x_w^T$ is the covariance matrix of x_w. Given that any restriction is set to the order of the sources, it is possible to assume that the source vector s is also white. In order to perform the whitening, an eigenvalue decomposition of x is carried out.

$$Exx^T = VDV^T \tag{3.8}$$

where V is the matrix of eigenvectors of Exx^T and D is the diagonal matrix of eigenvalues. Then we can whiten the observation vector by doing the following

$$x_w = VD^{-1/2}V^T x = VD^{-1/2}V^T A_s = A_w s \tag{3.9}$$

hence,

$$Exx^T = A_w Ess^T A_w^T = A_w A_w^T = I \tag{3.10}$$

Whitening transforms the mixing matrix in a new one, which is orthogonal, thus reducing the number of parameters to be estimated to $n(n-1)/2$ degrees of freedom instead of n^2 [108].

3.1.2.3 ICA Algorithms

Several approaches have been developed to determine the different independent components such Maximum Likelihood Estimation and Infomax [107], Projection Pursuit or FastICA [108]. In this thesis the Infomax method combined with a bayesian information criterion is used to estimate the number of components with the maximum likelihood [118].

It was formulated by Pham et al., 1992 [119] how to estimate the likelihood in a noise free ICaA model and then estimate the model by a maximum likelihood. The log-likelihood may be estimated as

$$L = \sum_{t=1}^{T} \sum_{i=1}^{n} log f_i(w_i^T x(t)) + T log|detW| \tag{3.11}$$

where W is the unmixing matrix, f_i are the density functions of the s_i and $x(t), t = 1, ..., T$ are the realisations of x [120]. For any random vector x with density p_x and for any matrix W, the density of $y = W_x$ is given by $p_x(W^{-1}|detW^{-1}|)$. Once the number of independent components had been estimated, the Infomax method was applied.

Infomax is a gradient-based neural network algorithm, with a learning rule for information maximisation [105, 107]. Under perfect conditions, Infomax provides the best estimation of ICA components. The algorithm is directly related to the information theory and is derived through an information maximisation principle applied between the inputs and the non linear outputs. The information maximisation is attained by maximising the joint entropy of a transformed vector [105]. Given the form of joint entropy:

$$H(s_1, s_2) = H(s_1) + H(s_2) - I(s_1, s_2) \tag{3.12}$$

here for two variables $s = g(Bx)$, it is clear that maximising the joint entropy of the outputs amounts to minimising mutual information I(y1,y2), unless it is more interesting to maximise the individual entropy than to reduce the mutual information [107]. The idea of maximisation is to match the slope of the nonlinear function with the input probability distribution. That is:

$$s = g(x, \theta) \simeq \int_{inf}^{x} f_x(t)dt \tag{3.13}$$

In the case of perfect matching, $f_x(t)$ looks like an uniform variable whose entropy is large [107]. If this is not possible because the shapes are different, the best solution found in some cases is to mix the input distributions so that the resulting mix matches the slope of the transfer function better than a single input distribution. In this case the algorithm does not converge, and the separation is not achieved.

3.1.3 Spectral Clustering

Clustering is a technique widely use in data analysis to identify groups of similar behaviour in the data. Among the traditional clustering methods such k-means or single linkage, spectral clustering emerges as a technique which often outperforms those traditional methods [121].

Spectral clustering was used throughout this thesis and therefore a brief introduction will follow. Spectral clustering is carried out in a few steps [121]:

- Data preprocessing: if the chosen clustering algorithm requires normalised data, a first step in which the data is normalised is required. In this thesis all datasets are normalised.

- Similarity graphs calculation: a similarity graph is an undirected graph $G = (V, E)$ with a vertex set $V = v_1, ..., v_n$ in where each vertex represents a data point. It is said that two vertices are connected if the similarity, $s(i, j)$, between two data points, v_i and v_j, is positive or larger than a certain threshold and that the edge E is weighted by the similarity value $w_{i,j}$. By means of these similarity graphs it is possible to search for a partition of the similarity graph where the edges among the different groups have very low weights (the points in different clusters are dissimilar from each other) and the edges within a group have high weighs (points within the same cluster are similar to each other)[121]. The similarity graphs can be constructed using different methods:

    1. The ϵ-neighbourhood graph: all the points whose pairwise distance is smaller than ϵ are connected.

    2. k-nearest neighbour graph: the idea is to connect one vertex with others if those are included in the k-nearest neighbours. There are two ways to do it. The first one consists in ignoring the direction of the edges and connecting the two vertices, v_i and v_j, with an undirected edge if the first vertex is among the k-nearest neighbours of the second vertex

or vice versa (k-nearest neighbours). The second involves connecting two vertices if both are between the k-nearest neighbours of each other (mutual k-nearest neighbours.)

3. The fully connected graph: here all points with positive similarity are connected with each other and all edges are wieghted by $s_{i,j}$.

Here, a k-nearest neighbour algorithm was used because it has been proven to be solid classifying signals in frequency domain [121].

- Laplacian graphs calculation: since we are working with normalised data, only two Laplacian graphs will be under consideration: the symmetric matrix (L_{sym}) and the random walk matrix (L_{rw}) [122].

$$L_{sym} = D^{-1/2} L D^{1/2} = I D^{1/2} W D^{1/2} \tag{3.14}$$

$$L_{rw} = D^{1} L = I D^{1} W \tag{3.15}$$

Both Laplacians differ slightly from each other but are based on the degree matrix D (diagonal matrix formed from the vertex matrix) and the weighted Adjacency Matrix W (a matrix of 1s or 0s depending if two vertex are adjacent or not). D is defined as the diagonal matrix with the degrees $d_1, ..., d_n$ on the diagonal. On the other hand, the weighted adjacency matrix of the graph is the matrix $W = (w_{ij}) i, j = 1, ..., n$. If $w_{ij} = 0$ this means that the vertices v_i and v_j are not connected [121].

- Spectral clustering algorithm: once the similarity and the Laplacian graphs are calculated, then the clustering algorithm is applied. Since the data is normalised only two methods will be described here:

1. Normalised spectral clustering according to Shi and Malik (2000) [123]: the first k generalised eigenvectors, $u_1, ..., u_k$, are calculated from L_{rw} and a matrix U is constructed containing the eigenvectors as columns. These eigenvectors are calculated from the generalised eigen-problem

$Lu = \lambda Du$. Finally, the vectors corresponding to each row of U are clustered using a k-means algorithm [124].

2. Normalised spectral clustering according to Jordan and Weiss (2002) [125]: the first k generalised eigenvectors, $u_1, ..., u_k$, are calculated from L_{sym} and a matrix U is constructed containing the eigenvectors as columns. These eigenvectors are calculated from the generalised eigenproblem $Lu = \lambda Du$. A matrix T is calculated from U by normalising the rows to 1. Finally, the vectors corresponding to each row of T are clustered using a k-means algorithm [124].

3.1.4 Fractal Analysis

The idea of fractals was first developed by Mandelbrot to explain objects whose complex geometry cannot be characterised by a single integral [126]. This idea was initially applied to the brain for geometrical purposes, for instance, the brain shape [127–129]. Moreover, the concept of fractals has been applied in the last decade to biomedical signals, since they have usually a large range of scale invariant structure (i.e., when the structure repeats itself on subintervals of the signal) [130]. Fractal analysis estimates for each time series the power law exponent that defines its particular kind of scale invariant structure [130]. This concept has been employed to study, for instance, alterations in disease and ageing [131, 132], variations during task and rest [133], the characteristics of sleep encephalograms [134] or to model the human neural activity [135]. Fractal analysis relies on the examination of the singularity spectrum by determining its fractal parameters. These are, for instance, the width (i.e., the width on the spectrum) [130, 134, 136, 137], the asymmetry (i.e., the indicator if the spectrum is located in the region of strong or weak singularities) [134, 138] or the position of the spectrum maxima [137].

The fractal parameters should vary in the presence of smaller or larger amount of singularities within the time series. Therefore, it might be possible to characterise the existent differences between time series. For this purpose the MultiFractal Detrended Fluctuation Analysis (MFDFA) method was selected.

3.1.5 Multifractal Detrended Fluctuation Analysis

MFDFA is a powerful technique used that can estimate the multifractal spectrum of power law exponents from a biomedical time series. The acquittance of the fractal parameters is carried out following the next steps [130, 139]:

1. Noise and random walk like variation in a time series: the detrended fluctuation analysis can only be applied to random like signals, therefore the first step consists of determining if the biomedical signal has a random walk or not. In case it is not a random walk, it is the time series that has to be converted by subtracting the mean and integrating.

$$Y(i) = \sum_{k=1}^{n} [x_k - \langle x \rangle] \tag{3.16}$$

2. Computing the Root Mean Square (RMS) variation of a time series.

3. Local variation in the time series: the time series is cut into equal size non-overlapping segments, N_s, and the RMS is calculated for each segment to determine the local variations.

$$N_s = int(N/s) \tag{3.17}$$

   where N is the length of the time series and s is the scale size.

4. Local detrending of time series: the detrending of time series is necessary to quantify the scale invariant structure of the variation around the slow trends presented in the biomedical signals. This process is carried out by a least-square fit of the time series:

$$F^2(s, v) = \frac{1}{s} \sum_{i=1}^{s} \{Y[(v-1)s + 1] - y_v i\}^2 \tag{3.18}$$

5. Monofractal Detrended Fluctuation Analysis (DFA): fast changing variations in the time series will influence segments with shorter lengths and slow

changing variations will influence larger segments. Therefore, the trends will be calculated for different scales.

$$F^2(s,v) = \frac{1}{s}\sum_{i=1}^{s}\{Y[N-(v-N_s)s+1]-y_v i\}^2 \tag{3.19}$$

DFA identifies the monofractal structure of a time series as the power law relation between the overall RMS computed at different scales.

$$F_q(s) = \{\frac{1}{N_s}\sum_{v=1}^{2N_s}[F^2(s,v)]^{q/2}\}^{1/q} \tag{3.20}$$

The power law relation between the overall RMS fluctuations F_q is indicated by the slope of the regression line (Hurst exponent, H).

$$F_q(s) \propto s^{H(q)} \tag{3.21}$$

The generalised Hurst exponent defines the monofractal structure of the time series by determining how fast the whole RMS of local fluctuation grows with increasing the segment size. The value will be between 0 and 1 for noise time series, whereas it will be above 1 for random walk series.

6. Multifractal detrended fluctuation analysis of time series: multifractal time series have local fluctuations that are both extreme and small, while this is an effect that is not present in monofractal time series. Thus, inside the multifractal time series, local fluctuations will be large for segments with periods of large fluctuations and small for small periods. Consequently, all the q-order moments have to be considered. With this, every Hurst exponent ($H(q)$) will be computed as the regression line of the RMS associated with each q-order. As mentioned above, at short segment sizes the small and large fluctuations are stronger and therefore the correspondent $H(q)$ will be larger. However, at large segment sizes the small and large fluctuations cancel each other out and the it becomes nearly impossible to distinguish between multi

and the monofractal time series. For this reason, the selection of the segment sizes is a critical component in the analysis.

7. The multifractal spectrum of time series: the spectrum is calculated from the $H(q)$ previously obtained. From each $H(q)$ the mass exponent t_q can be obtained.

$$t_q = H(q) * q - 1 \tag{3.22}$$

This is consequently transformed via Legrende transform into q-order singularity exponent (hq) and dimension (D_q).

$$h_q = t'_q \tag{3.23}$$

$$D_q = \frac{t_q}{q-1} = \frac{H_q * q - 1}{q-1} \tag{3.24}$$

The plot of the latter versus the former gives the multifractal spectrum. It is this spectrum which allows us to understand the properties of the time series. For example, the spectrum can have either right or left truncation that originates from levelling the h_q from positive to negative q_s. A multifractal spectrum will have a long left trail when the time series has a structure which is insensitive to the local fluctuations with small properties. On the other hand, multifractal spectrum will have a long right trail when the time series has a structure insensitive to the local fluctuations with large magnitudes. Thus, the width and shape of the multifractal spectrum is able to classify a wide range of different scale invariant structures of biomedical time series.

Part III

The Cardiac Induced Modulated MRI Dignal

Chapter 4

Material and Methods

4.1 Data Acquisition

First, in order to understand the origin of the signal, 40 subjects in total (between 18 and 30 years old) were scanned with the protocols approved by the Trinity College School of Medicine Research Ethics Committee. Each participant was imaged in a 3.0 T Philips whole-body MRI scanner (Philips, The Netherlands) using a standard single-shot GE EPI sequence. Two RF array coils of 8 and 32 channels were used. The parameters of the EPI sequence were varied in the following fashion:

1. When the RF array coil of 32 channel was in use, participants were scanned with FA = 35 degrees, TR = 45 ms and the TE = 5 ms with a voxel size was 3.5 x 3.5 x 3 mm. The SENSE factor was set to 3.

2. When the RF array coil of 8 channels was in use, participants were scanned with FA = 30 degrees, TR = 60 ms and the TE = 18 ms with a voxel size was 3.5 x 3.5 x 3 mm. The SENSE factor was set to 2.

Two REST slabs of 5 mm in thickness were placed parallel to the imaged slice. The first one was located above the imaged slice at a distance equal to 15mm.

The second one was placed below separated by 20 mm. These slabs were applied to suppress unwanted flow artifacts from vessels entering the imaged slice [64]. Additionally, the excitation of the REST slabs induced an RF off-resonance pulse leading and thus introduce the MT effects. MT effects were introduced in both cases by a negative (-13411 ± 2290Hz) and a positive off frequency (17882 ± 2290 Hz) RF pulse. The imaging slice was placed away from the ventricle to avoid pulsation effects. Two different configurations were used. When the 8-channel coil receiver was used, the imaging slice was placed with angulation above the ventricle (Fig. 4.1a). Data from this coil was part of a bigger study which needed information about the anterior circulate cortex. The reason of the angulations is to avoid the ventricle pulsation. On the other hand, when the 32-channel coil receiver was used, the imaging slice was set without angulation above the ventricle (Fig. 4.1b). Throughout this thesis, UEPIS (Ultrafast EPI with Slabs) will referred to those cases where the REST slabs are present.

Secondly, for the purpose of determining the contrast mechanism a variation of some of the MRI sequence parameters was performed. 30 subjects in total (between 24 and 42 years old) were scanned with the protocols approved by the Trinity

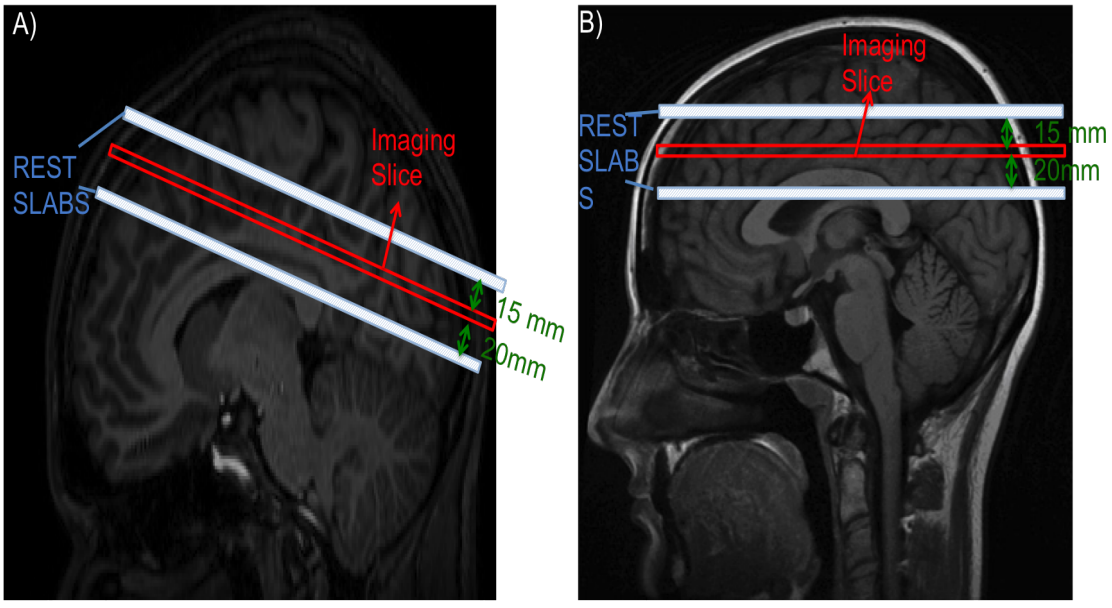

FIGURE 4.1: Acquisition model which includes the imaging slice (red) and the REST slabs (light blue) both 5mm thick and separated 15 mm and 20 mm respectively. a) corresponds to the protocol used with 8-channel coil and b) to the 32-channel coil.

College ethics committee and the Irish Department of Health. Each participant was imaged in a 3.0 T Philips whole-body MRI scanner (Philips, The Netherlands) using a standard single-shot GE EPI sequence. A 32-channel array receiver coil was used in all cases. The parameters of the EPI sequence were varied in the following fashion:

1. Five participants were scanned while the FA was varied between 5 and 60 in steps of 5 degrees, while the TR = 45 ms and the TE = 5 ms and the voxel size was 3.5 x 3.5 x 3 mm.

2. Five participants were scanned while the FA was varied between 5 and 60 in steps of 5 degrees, while the TR = 60 ms and the TE = 5 ms and the voxel size was 3.5 x 3.5 x 3 mm.

3. Five participants were scanned while the TR was changed with values [38, 43, 48, 53, 58, 63, 68 and 73] ms, while the TE= 5 ms, the FA = 35° and the voxel size was 3.5 x 3.5 x 3 mm.

4. Five participants were scanned while the voxel size was changed by increasing the slice thickness from 3 mm to 7 mm in steps of 0.5 mm, while TR = 45 ms, the TE= 5 ms and the FA= 35°.

5. Five participants were scanned while the distance of the REST slabs were varied between 0.8 mm and 50 mm to alter the off-resonance frequency while the voxel size was 3.5 x 3.5 x 3 mm, the TE = 5 ms, TR = 45ms and the FA = 35°. The off-resonance frequency was calculated using the following equation:

$$Freq = \gamma F_{strength} d \tag{4.1}$$

   where γ is the gyromagnetic ratio equal to $42.57E^3 Hz/mT$, $F_{strength}$ is the field strength (i.e., $21mT/m$) and d is the distance is meters between the centre of the imaging slice and the centre of the REST slab.

6. Five participants were scanned while the TE was varied between 5 and 21 ms in steps of 2 ms, while the TR = 45 ms, flip angle (FA) = 35° and the

voxel size was 3.5 x 3.5 x 3 mm. Partial Fourier of the k-space equal to 0.71 was used to allow having the same bandwidth at all TEs.

The duration of each run varied between 38 and 73 seconds.

In all scans two REST slabs of 5 mm in thickness were placed parallel to the imaged slice. The imaging slice was placed away from the ventricle to avoid pulsation effects (see Figure 4.1b).

Additional scans were acquired without REST slabs above and below:

1. Five participants were scanned while the FA was varying between 5 and 90 in steps of 5 degrees, while the TR = 37, the TE = 5 ms and the voxel size was 3.5 x 3.5 x 3 mm.

2. Five participants were scanned while the TR was changed with values between 26 and 51 ms in steps of 2.5 ms, while the TE= 5 ms, the FA = 35° and the voxel size was 3.5 x 3.5 x 3 mm.

The duration of each run varied between 26 and 51 seconds. Again, the imaging slice was set without angulation and placed above the ventricle to avoid artefacts due to its pulsation.

Anatomical MRI images in all studies included a high-resolution sagittal, T1-weighted MP-RAGE (TR = 2.1 s, TE = 3.93 ms, flip angle = 7°).

4.1.1 Additional Scans

Three participants took part in an hyper and hypoventilation experiments. Three scans were acquired for each case. The two first scans consisted in a hypoventilation with and without MT effects and the last scan during hyperventilation with MT effects. Each hypoventilation scan had 6600 repetitions while the hyperventilation scan had 8000 repetitions. MT effect was introduced by a negative (-13411

± 2290 Hz) and a positive off frequency (17882 ± 2290 Hz) RF pulse. The same parameters were established for each scan: TR = 45 ms, FA = 35°, voxel size was 3.5 x 3.5 x 3 mm and TE = 5 ms. The hypoventilation protocol was designed as follows: after one minute of rest, the participants were asked to hold the breath during 20 seconds. This was repeated three times and at the end 1 minute rest was added. The hyperventilation protocol was designed the same way but the hyperventilation lasted 40 seconds. An image was shown in the screen to indicate the start and end of each period of hypo or hyperventilation.

In addition, five participants were scanned for 5 minutes at rest using the same parameters as in the hypo and hyperventilation experiment.

9 slices were acquired at different positions for five participants, with each slice matching from bottom to the top the position of those acquired in the anatomical scan. Each scan had 1000 repetitions, with TR = 45 ms, FA = 35°, voxel size was 3.5 x 3.5 x 3 mm and TE = 5 ms. The experiment was carried out with and without the REST slabs.

Finally, anatomical MRI images in all studies included a high-resolution sagittal, T1-weighted MP-RAGE (TR = 2.1 s, TE = 3.93 ms, flip angle = 7°).

4.2 Data Analysis

All calculations were developed in a Dell Optiplex 790 with 12 Gb RAM using Matlab 2014a (http://www.mathworks.co.uk/). All the calculations were carried out with an in-house built Toolbox (see Appendix C).

4.2.1 Preprocessing

Prior to any calculation motion correction could not be applied due to the single slice nature of the experiment. First, each average time series was visually inspected in search for movement. Since movement produces abrupt changes in

the time series (i.e. much higher than the cardiac related peaks), these movement related peaks were manually removed from the analysis leaving the rest of the time series unaltered. In addition, the data was not smoothed to avoid removing low frequencies which may lead to the loss of information [140].

Manual segmentation was used to create a mask to remove cerebral spinal fluid (CSF) contributions. The first 100 scans were removed to avoid signal saturation effects. The manual segmentation of the masks was eroded to avoid partial volume effects at the edges.

All images within a time series have the same scaling values. However, differences appear between separate acquisitions. Therefore, rescaling was applied to all datasets before any analysis. The signal intensity of all voxels at each PAR/REC and normal DICOM files was computed using:

$$PV = \frac{DV - RI}{RS} \tag{4.2}$$

where PV is the pixel value, DV is the displayed valued, RI is the rescale intercept and RS is the rescale slope. In enhanced DICOM each acquired slice has its own scaling/rescaling functions. Therefore, in this case is each slice was corrected individually.

4.2.2 Linear Regressions

Linear models were constructed in the data using the *LinearModelFit* function in Mathematica (Wolfram Research, Champaign, Illinois). This function provides the individual parameter estimates, tests of parameter significance (t-test and p-values), and confidence intervals obtained using the error estimates.

4.2.3 Mean Maximum Peak Detection

The detection of the peak maxima is based on the method proposed in Gomes and Pereira 2013 [141]. The method uses the open function *peakdet* implemented in Matlab, to detect all the local maxima of the temporal signals. The mean baseline signal will be the mean value of the remaining time points (i.e., the peak maxima were excluded to compute the mean baseline). The peak-to-signal value for each time series will be calculated by computing the % signal change in comparison to the baseline at each peak position.

For each time series the error was calculated by standard deviation between the % signal changes of all peaks within the time series. When averaging across subjects the error was amounted using a standard Gaussian error propagation where the average standard deviation was calculated as the square root of the sum of all variances.

To calculate the spatial distribution in the whole slice of the maxima in the oscillation, the signal at each voxel was treated individually. Then, the % signal change for each voxel was calculated using the *peakdet* function aforementioned. An intensity map was created with all the values.

4.2.4 Fourier Transform

Fourier transform were computed to decompose the time signals into separate frequencies. In all calculations, a zero-padding of 4096 points was applied to calculate the power spectra. Zero padding allows one to use a longer FFT, which will produce a longer FFT result vector. A longer FFT result has more frequency bins that are more closely spaced in frequency [142].

4.2.5 ICA Analysis

Temporal Independent Component Analysis (tICA) was used to decompose the UEPIS signal into independent non-Gaussian components. The number of source components was estimated for each subject by using Bayesian Information Criterion (BIC) [118]. The maximum number of possible source components was set to 30 to reduce computational times. Singular value decomposition was used for dimension reduction. Finally, the temporally independent components were computed using the estimated number of source components and a maximum likelihood, square mixing matrix and no noise algorithm [107].

The different components were visually classified into three main groups: pulsation or physiological components, artefacts and other signals. tICA time courses were Fourier transformed to compute power spectra.

4.2.6 Wavelet Analysis

Wavelet analysis was used to study transient effects in the UEPIS signal. The average signal across the slice was decomposed into separate wavelet coefficients using a Mexican Hat mother wavelet. This wavelet was selected because of its similarity with the shape of the oscillation in the UEPIS signal. The coefficients were calculated using a continuous wavelet transform, with scales ranging from 1 to 64 in steps of 0.1. The frequency of the wavelet was 1/TR of the signal acquisition.

The first coefficient(i.e. calculated with the lowest scale), corresponds to a detailed information of a hidden pattern in the signal. This was used to determine the frequency of the UEPIS wavelet. The reason for this is that a mother wavelet with the fastest frequency (i.e., lower scales) offers a more detailed description of the signal. The frequency of the cardiac induced oscillation was determine following the next steps:

- Find the position of the oscillation maxima inside the first wavelet coefficient.

- Locate the first peak to the left and to the right within a time period of 250 ms and average across all the cardiac induced oscillations
- In the time series, the peaks were located using the *peakdet* function of Matlab.
- The inverse of the mean time between peaks gives the frequency of the oscillation.

The frequency of the cardiac induced oscillation was compared to the cardiac frequency of the average signal. Fourier Transform was used to find the cardiac frequency of the time series. The linear correlation coefficient was calculated using a Pearson's correlation coefficient and the p-values using a Student's t distribution for a transformation of the correlation.

Chapter 5

The Cardiac Induced Modulated MRI Signal

5.1 Results

5.1.1 The Cardiac Induced Modulated MRI Signal

The characteristic cardiac induced modulated MRI signal time series is shown in Figures 5.1 and 5.2. In the brain of healthy subjects, the signal is characterised by relatively constant modulated oscillation with a similar frequency as the cardiac cycle.

Although both images clearly show a strong cardiac behaviour, there are slightly differences between them. In Figure 5.1, the cardiac induced oscillation has a relatively wide curve with one or sometimes two peaks. Additionally, the relation between the peak os the oscillation and the mean baseline value is approximately 5% of the whole signal. However, in Figure 5.2, the main peak is followed in most cases by smaller ones before and after it. The peak to mean baseline relation in this case is larger than 10%.

In Figure 5.3a, the typical peaks are unveiled. The main signature of the cardiac induced oscillation cycle is defined by a sharp peak followed by smaller peaks that

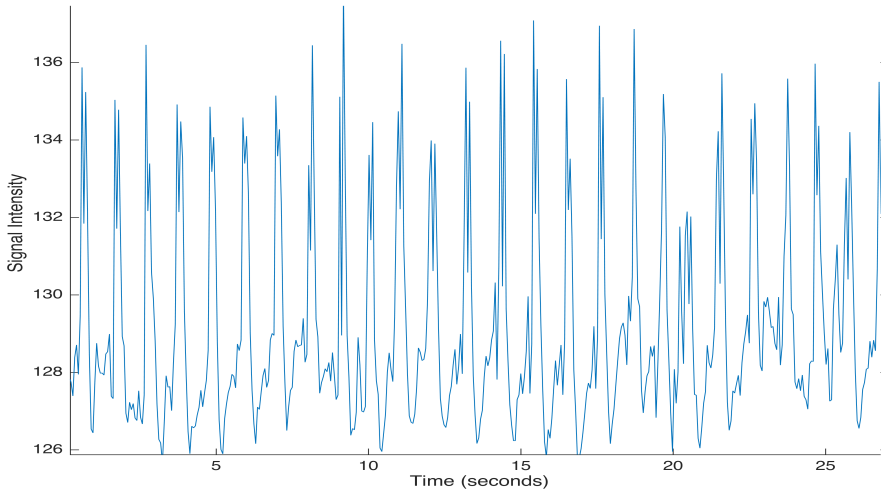

FIGURE 5.1: Example of the UEPIS time series obtained with the 8-channel coil receiver.

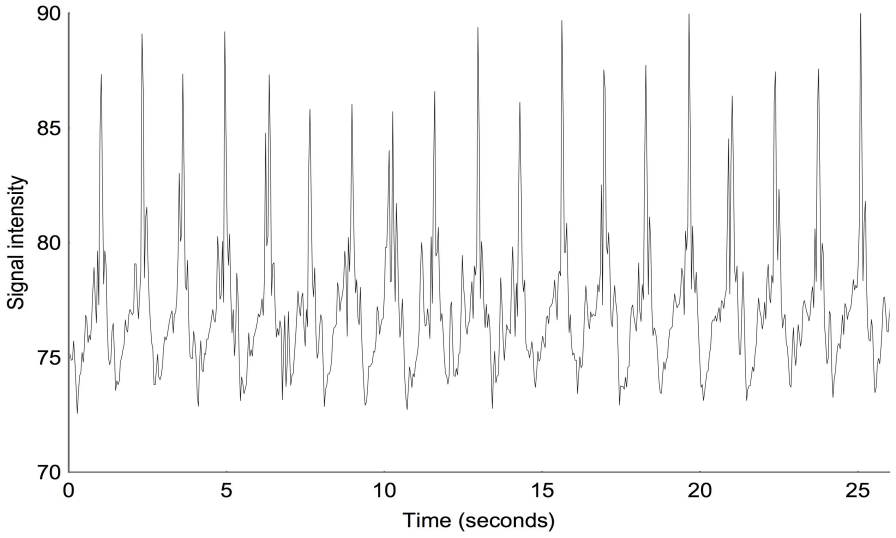

FIGURE 5.2: Example of the UEPIS time series obtained with the 32 channel coil receiver.

can be found before the signal decays into the baseline level. In addition, Figure 5.3b illustrates the comparison between the temporal signal of cardiac induced oscillation and the wavelet coefficients with the lowest scale. As expected, the first coefficient of the wavelet analysis correlates with the UEPIS signal.

Figure 5.4 illustrates the differences between the presence or absence of the REST slabs. The differences between both sequences are visible not only in time domain (Fig. 5.4a) but also in frequency domain where the UEPIS signal generates a larger

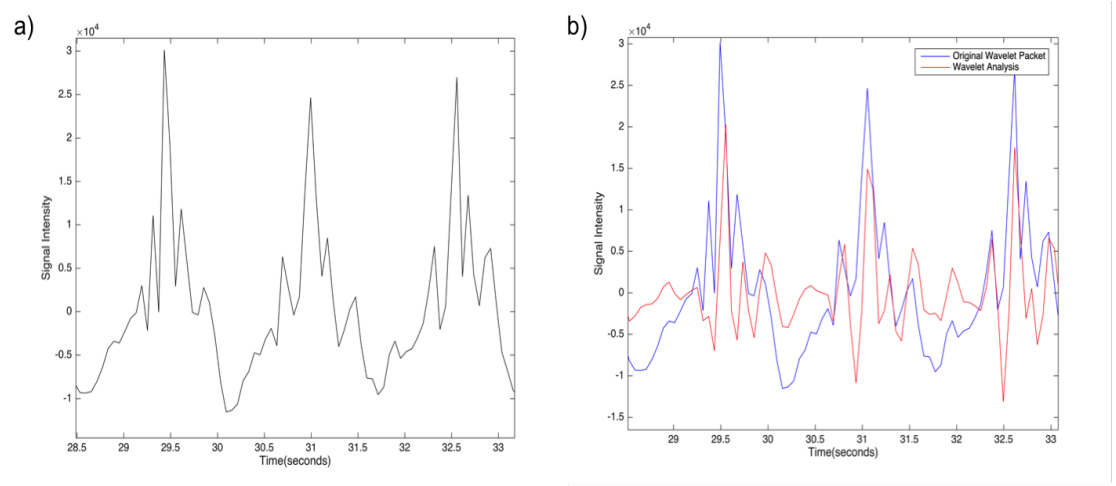

FIGURE 5.3: The main signature of the cardiac induced oscillation is defined by a sharp peak followed by smaller peaks that can be found before the signal decays into the baseline level.

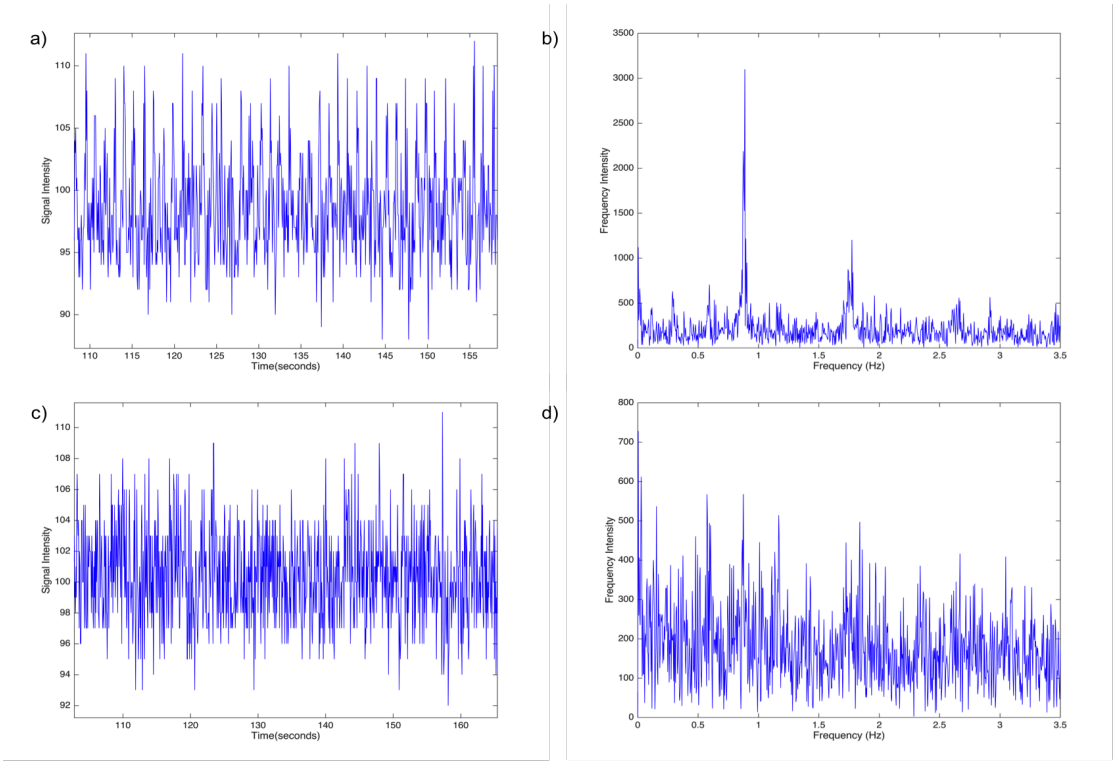

FIGURE 5.4: Differences in time and frequency domain between the presence (a and b) or absence (c and d) of the REST slabs.

cardiac frequency and in some cases harmonics (Fig. 5.4b). When no REST slabs are present, the profile of the oscillation can be sensed but it is not clear any more (Fig. 5.4c). Additionally, no cardiac frequencies are observed in frequency domain (Fig. 5.4d).

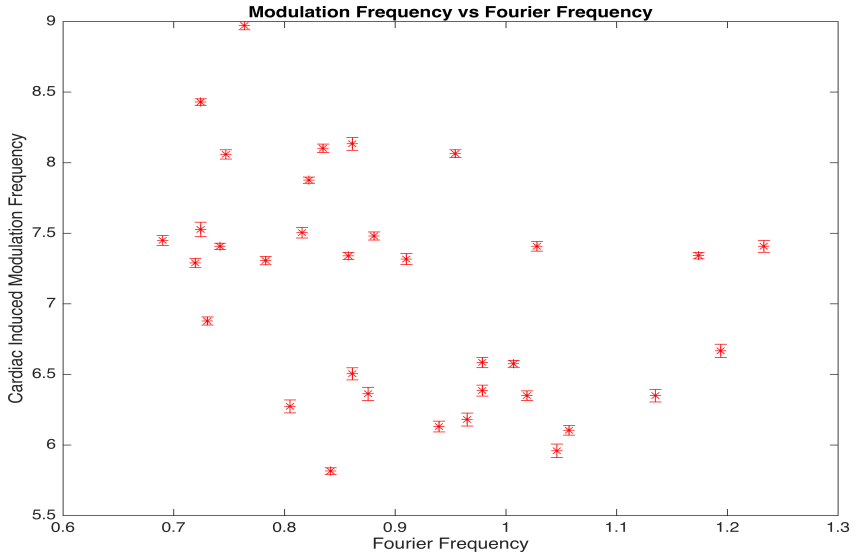

FIGURE 5.5: Comparison of the frequency of the cardiac induced oscillation and the Fourier frequency of the time series of different subjects.

Finally, the average cardiac induced oscillation frequency was computed from the first wavelet coefficient and compared to the Fourier frequency of the average time series. The correlation between both frequencies is shown in Figure 5.5. The Pearson Correlation coefficient was -0.4099 with a p-value of 0.0161 revealing a little but significant correlation between the cardiac frequency and the frequency of the oscillation. The mean average oscillation frequency among all participants was 7.1037 ± 0.7911 Hz.

5.1.2 Spatial Distribution of the UEPIS Signal

Further comparison appears in Figure 5.6 where the same 4x4 voxels region was extracted from the acquired slice and each temporal series was represented. As shown in this figure all the signals from UEPIS (Fig. 5.6a) have strong cardiac dependency while those acquired with non-UEPIS exhibited a noisy behaviour (Fig. 5.6b).

The distribution of the cardiac induced oscillation maxima was calculated using the average signal at each voxel in different slices (Fig. 5.7). The distribution was practically homogeneous with only high values in big vessels and CSF areas. As it

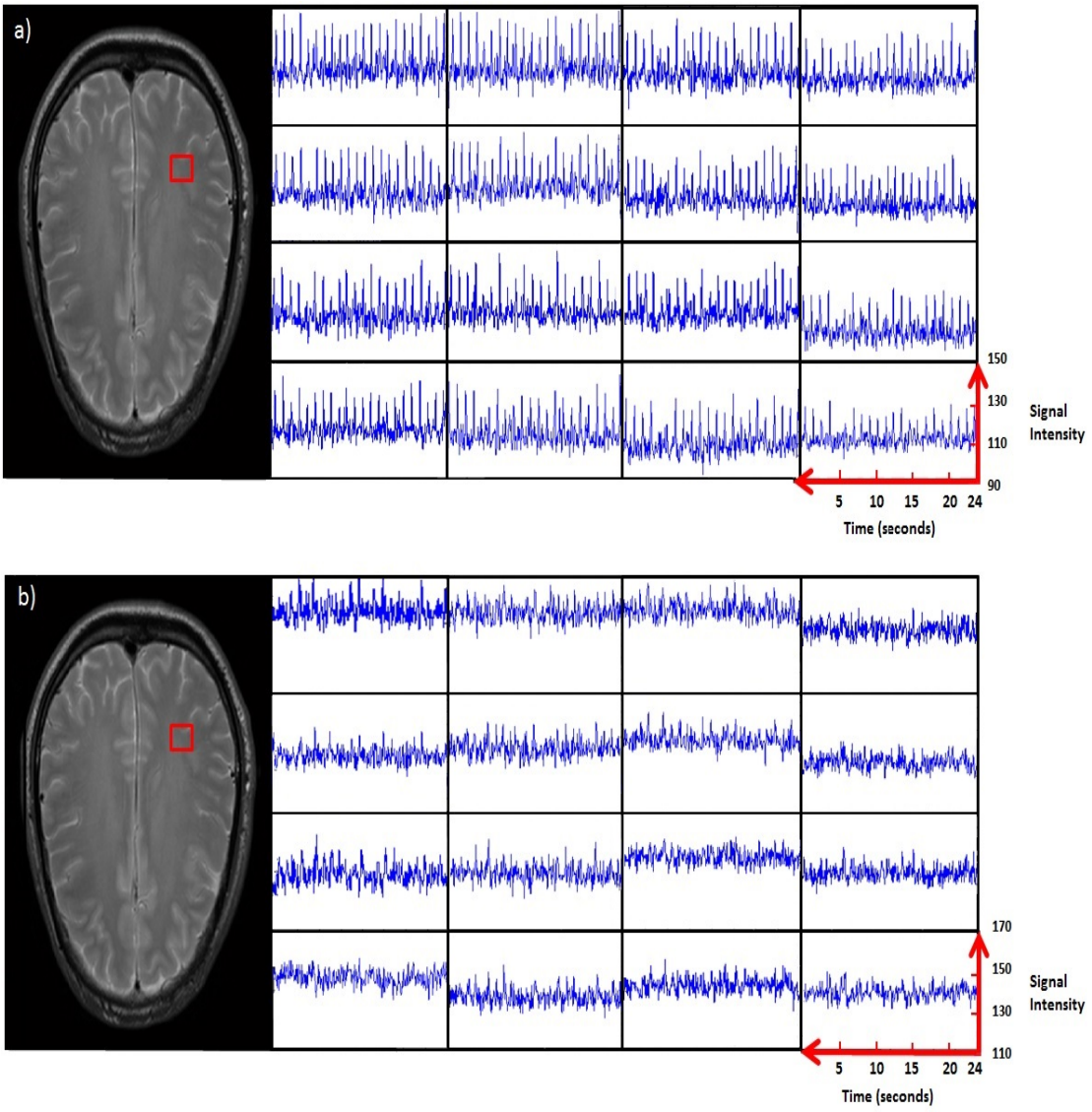

FIGURE 5.6: Representation of the time series of each voxel inside a 4x4 region. 5.6a represents the slice acquired with the UEPIS sequence while 5.6b represents the slice acquired with the non-UEPIS sequence. The scale in the bottom right corner is applicable to all 16 images in each case.

may be seen, the intensity of peak in white matter looks apparently higher than the intensity in grey matter.

Figure 5.8 illustrates the difference between the signal obtained in a voxel in tissue and the signal from pixels located at the skull. The pixels located at the skull provide a noisy signal without any cardiac induced oscillation which contrasts with the signal in tissue that has a cardiac behaviour.

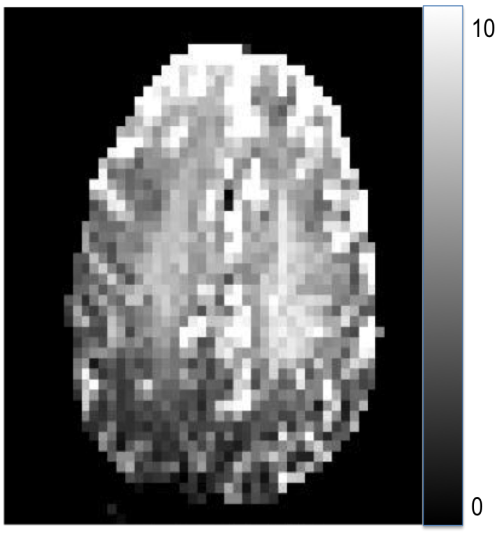

FIGURE 5.7: Example of the peaks distribution calculated using the overall signal.

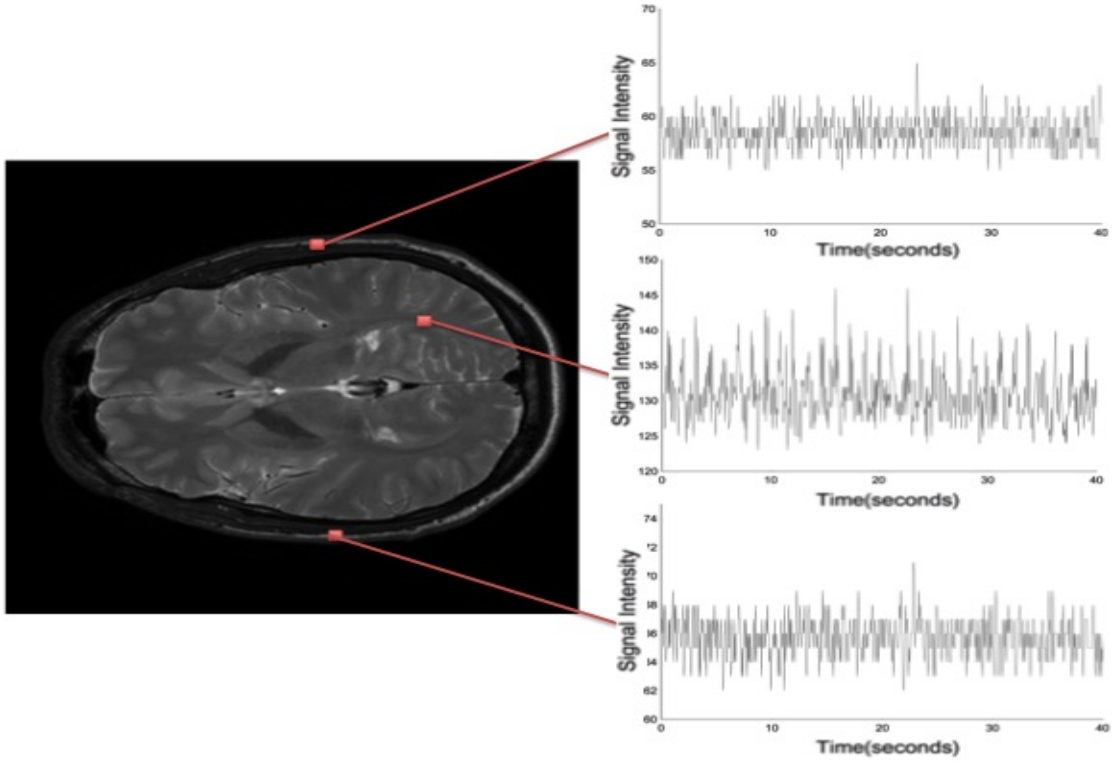

FIGURE 5.8: Comparison between the time series of a voxel located at the tissue with the voxels located in the skull.

5.1.3 Temporal Distribution of the UEPIS Signal

A slice crossing through an artery and the sinus vein was used to determine the time of arising of the cardiac modulated oscillation. ICA analysis was used to extract the time course containing the main peak of the oscillation. Figures 5.9

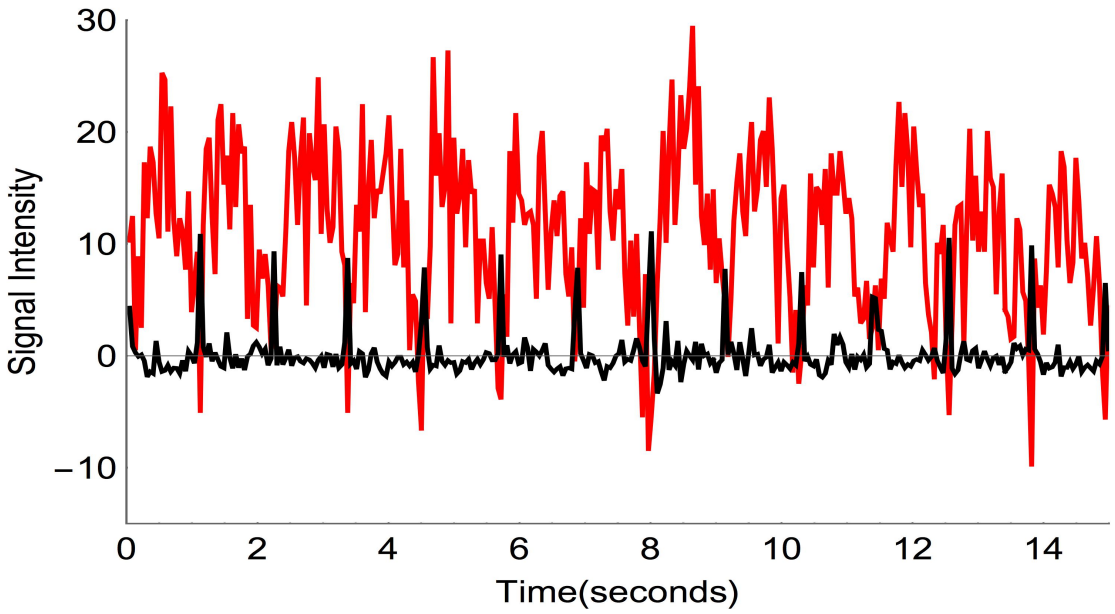

FIGURE 5.9: Comparison between the time series of a voxel in a small artery and a voxel located in tissue. The red line represents the moment in which there is a maximum in the tissue.

and 5.10 show the comparison of the time series with the signal arising from the vessels. In the first picture it can be observed that the maximum value of the oscillation emerges (black) just before or sometimes at the same time as the signal from the artery (red). However, Figure 5.10 outlines that the UEPIS peak

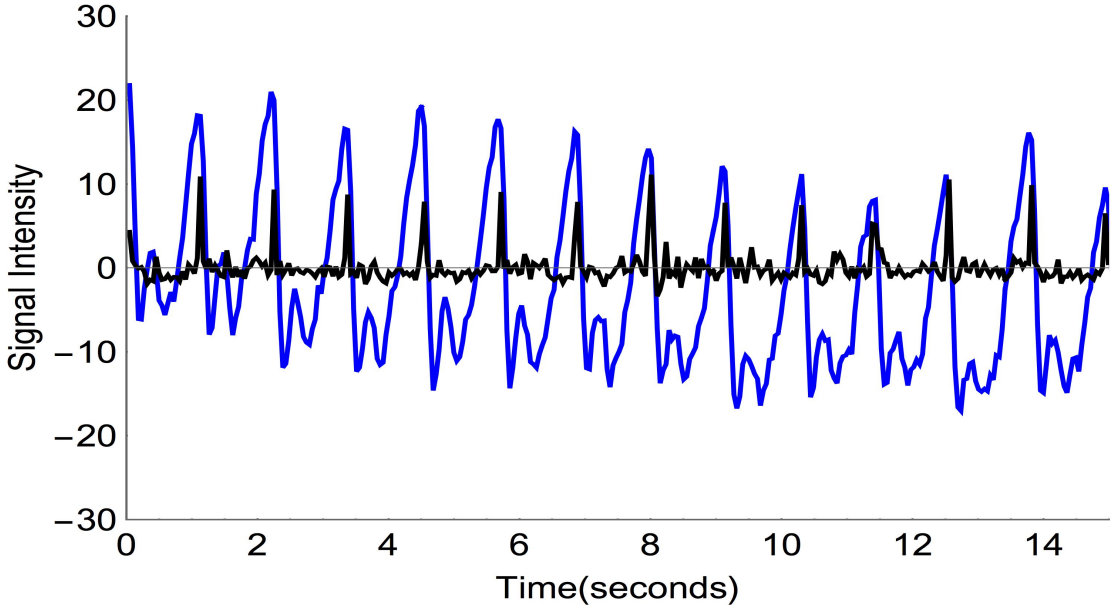

FIGURE 5.10: Comparison between the time series of a voxel in the sinus vein and a voxel located in tissue. The blue line represents the moment in which there is a maximum in the tissue.

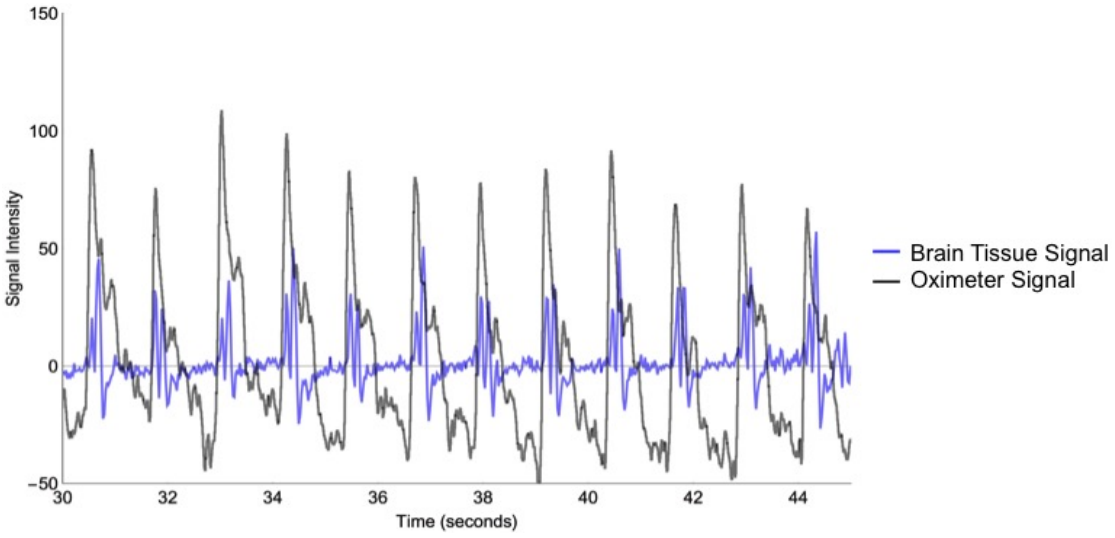

FIGURE 5.11: Comparison of the signal located in the tissue with the signal measured in the oximeter.

manifests itself just after the signal vein disappears. The profiles of the artery and the vein are inverted due to the effect of the REST slabs.

The comparison between the signal from a oximeter located in one finger and the cardiac modulated oscillation can be found in Figure 5.11. Both signals arose practically at the same time.

5.1.4 A Propagating Wave or a Pilot Wave?

Figure 5.12 gives an example of the signals obtained in several pixels located across the imaging slice without any angulation. The signals from a pixel located at the front, at the middle and at the back of the slice are shown. As it may be appreciated the signal in all cases arises at the same time (See Appendix A for further examples).

In the same fashion, Figure 5.13 gives an example of a few pixels located across the imaging slice with angulation on it. The signal of the pixel at front arrives at separate points in comparison to the pixel located at the back (See Appendix A for further examples).

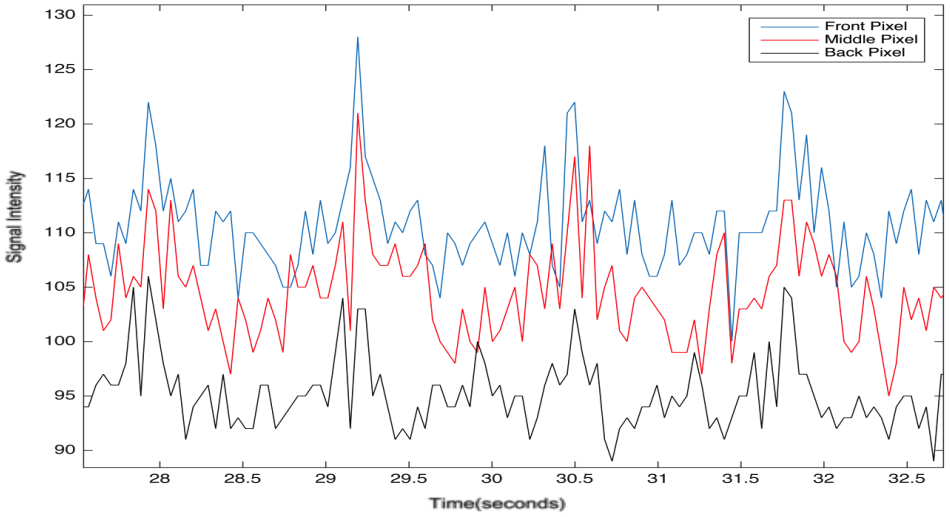

FIGURE 5.12: Comparison of the signal of three pixels located at different areas without angulation in the horizontal imaging slice. One pixel was located at the front, the second at the middle and the last one at the back of the slice.

5.1.5 ICA vs Wavelet Analysis

Wavelet analysis carried out to extract the first wavelet coefficient from the average signals. Example of the first wavelet coefficient is shown in Figure 5.14. The first wavelet coefficient is constituted by cardiac induces oscillations of three or four

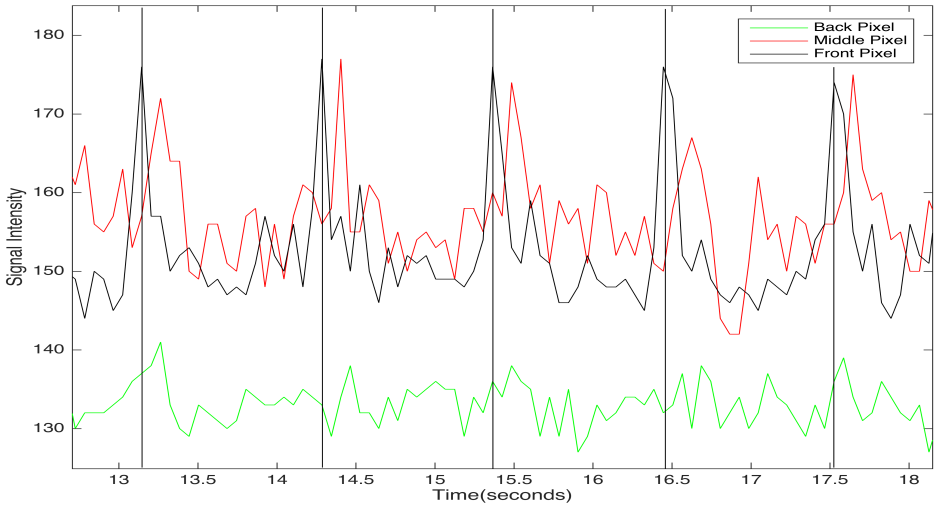

FIGURE 5.13: Comparison of the signal of three pixels located at different areas in an angulated imaging slice. One pixel was located at the front, the second at the middle and the last one at the back of the slice.

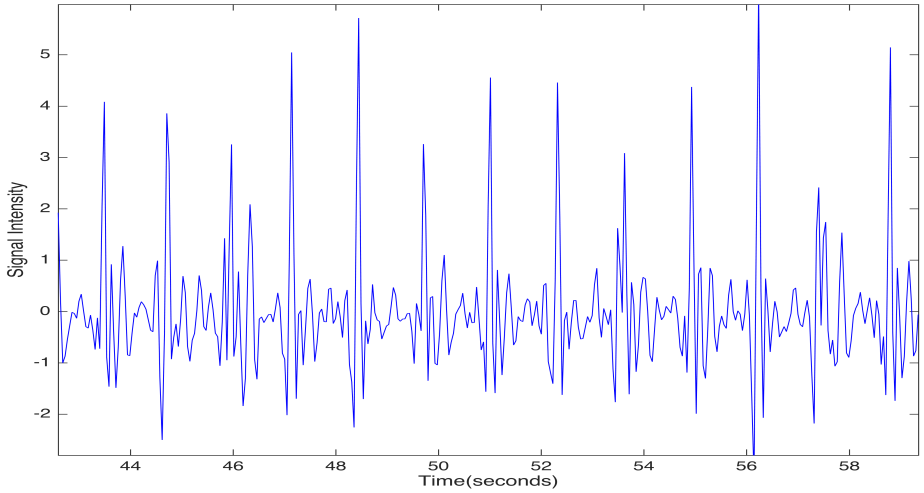

FIGURE 5.14: Example of the first wavelet coefficient time series.

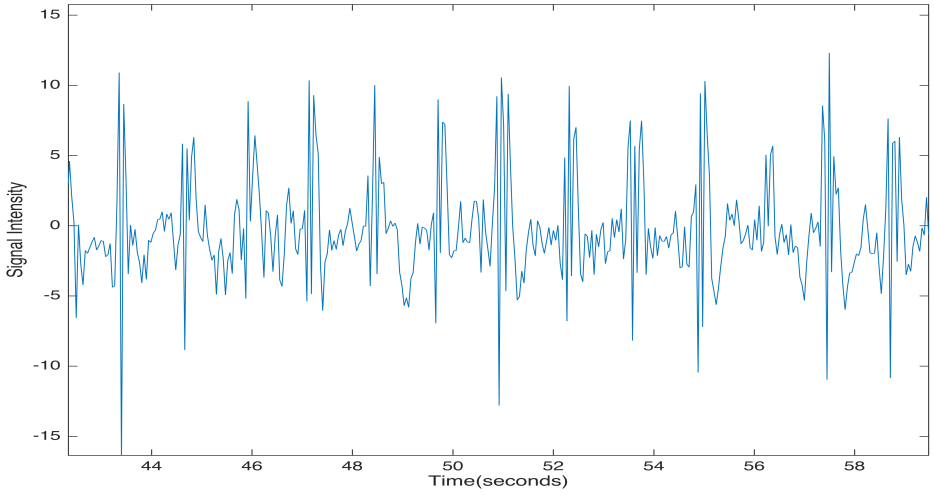

FIGURE 5.15: Reconstructed oscillation from the ICA cardiac components that exhibited strong cardiac behaviour.

peaks separated between times of reduced noise.

The cardiac components obtained from the ICA analysis where combined into one time series (Figure 5.15). The signal resembles a cardiac induced oscillation as the one obtained with the first wavelet coefficient.

5.2 Discussion

In this chapter, the physiological aspects of the cardiac induced modulated signal have been observed and can be summarise as follows. With UEPIS if has been found during every cardiac cycle a time window of around 300-400ms (depending on the volunteer) in which a dynamic signal change of up to 15% has been observed. This enhanced signal also carries a frequency of 7.1037±0.7911 Hz. Figures 5.1 and 5.2 showed the typical time course, which also demonstrated periodical behaviour with the cardiac frequency. The timing of signal during the cardiac cycle occurs at a moment between the depletion of the venous output and the increase in the arterial input.

The signature from a single imaging voxel remains very similar even when averaged over all voxels of the slice if it was horizontally angulated. This means that the signal changes are in coherence over most of the slice. If the slice angulation was changed, a shift between frontal and back areas was observed. The shift in time is always in the range of a full oscillation cycle of around 120ms. From that we conclude that we observe a carrier frequency that is in most area of the brain in phase like a standing wave which is modulated by the cardiac pressure wave. The pressure wave is on the other hand a traveling wave. Therefore, it can be hypothesised that the carrier frequency is a synchronised tissue response to a cardiac pressure modulation. Its behaviour is remarkably similar to de-Broglie's concept of the pilot wave [143].

5.2.1 The Cardiac Induced Modulated MRI Signal

The cardiac induced modulated MRI signal is characterised by a cardiac induced oscillation with an oscillation frequency of 7.1037 ± 0.7911 Hz. Fourier transform showed that it coincides with the arterial blood flow pulsation. This oscillation is characterised by a sharp peak followed by smaller peaks that can be found before the signal decays into the baseline level.

The frequency of the oscillation was found in the range between theta and alpha waves [144, 145]. Figure 5.5 illustrated the relationship between the frequency of the oscillation and the cardiac frequency, where little correlation was found among them. In spite of being small, this correlation cannot be ignored since 16.8% of the variance of the wavelet frequency can be explained through the variance of cardiac frequency. In addition, this plot might suggest that there are two defined oscillation frequencies, i.e., one below 7Hz and one above 7Hz. If that is true, it would be able to distinct between theta and alpha values, or between participants falling asleep and awake participants.

In order to determine the frequency of the oscillation, the average signal across the slice was separated into different wavelet coefficients. Coefficients at lower scales provide a more detailed description of underlying effects within the time series [95]. Therefore, the first wavelet coefficient was the one used to estimate the frequency of the oscillation. A Mexican hat mother wavelet was used due to its similarity to the main peak in the oscillation. Nevertheless, the problem was that the fastest possible wavelet had a central frequency of 5.5 Hz which is below the value obtained for the oscillation. This could represent a limitation to the accuracy of the results and the efficiency obtaining the hidden patterns in the data. A possible solution could be to increase the sampling frequency (i.e., reduce the TR) but the use of REST slabs represents a limitation to it. Another option would be to use ICA to detect all the components from the oscillations. It was shown that it is possible to reconstruct the oscillation from the ICA cardiac related components. However, the problem with ICA is that the sign of the components is not known. This could lead to erroneous interpretation in the position of the peaks within the cardiac induced oscillation. Further research has to be carried out in this area.

5.2.2 Spatial Distribution of the Cardiac Induced Modulated MRI Signal

The cardiac induced oscillation was equally distributed across the imaging slice. This oscillation was found in every voxel of the brain tissue when the REST slabs were applied. In fact, areas outside the brain tissue, such as the skull, did not produce any cardiac behaviour. This strengthens the idea that the signal is delimited to the brain tissue. Additionally, it discards the possibility that the signal is due to phase shifts artefacts (i.e., artefacts are due to moving protons at the time of the echo collection). Otherwise, a signal loss and ghosting effects associated with such movement would appear.

Although it is not clear in the peak intensity maps, a slight contrast between white and grey matter can be sensed. In these maps, white matter appears to be more hyper-tense than grey matter. This can be explained by the use of the REST slabs. The off-resonance frequency needed to excite the REST slabs induced MT effects into the imaging slice. Since MT effects affect white matter in a higher extent that in grey matter [57], a higher variance could be expected in white matter.

5.2.3 Temporal Distribution of the UEPIS Signal

The arising of the temporal signal was shown to appear right before the arterial blood input arrives and before the venous output arises. In addition, it is known by the Monro-Kellie hypothesis that the cranium and its constituents create a state of volume equilibrium, that any increase in volume of one of the cranial constituents must be compensated by a decrease in volume of another, i.e., if the arterial input flow arrives, the CSF leaves the brain system to compensate the incoming volume [146, 147]. In the same fashion, when the blood leaves the brain through the venous system, the CSF comes in again [146, 147]. The process happens in a fast and rhythmic way always triggered by the heart. This could suggest that the peak arises at the moment of less movement in the brain since the arterial input has already gone into the venous stream and the arterial input has still not spread

through the capillaries. In fact, Chapter 6 will show that movement affects the signal from the oscillation. However, the Monro-Kellie hypothesis is concerned about the volume equilibrium over all compartments which is possible cancelling in and outflow [146, 147]. But flow and pressure are related to each other through a set of nonlinear equations (i.e., Navier-Stokes equations) and therefore they can not cancel each other out [20]. Hence, the importance of understanding this cardiac induced oscillations.

5.2.4 A Propagating Signal in Brain Tissue?

The cardiac induced oscillations emerge at the same in each voxel of the imaging slice when the slice is place perpendicular to z-direction. However, when the imaging slice was angulated differences were found among the timing between peaks at different locations of the slice. It could be thought that there is a rhythm travelling in the brain that gets modulated through the input cardiac pressure wave. However, in this case, some differences in the timing of the peak should have be observed when the slice was placed horizontally. Thus, the most likely explanation is that the cardiac pressure wave is the travelling wave and modulates the rhythms present in the brain. Hence, the differences between areas when the slice was angulated. So far, the significance of the slice position is not clear.

Furthermore, there is not an equal rhythm for the whole brain, but separate regions might have different rhythms. An important implication of this is that these different rhythms would imply different maxima for the cardiac induced oscillation. Therefore, this question remains to be addressed and further study of the issue is still required.

Chapter 6

The Contrast Mechanism of the Cardiac Induced Modulated Signal

6.1 Results

All contrast related MRI parameters which were changeable without manipulation of the MRI system had been varied to identify the origin of the signal mechanism. These parameters are: (a) TR, (b) slice thickness, (c) flip angle, (d) off frequency of the magnetisation transfer pulse and (e) TE.

6.1.1 Variation of UEPIS Sequence Parameters

6.1.1.1 Repetition Time

The maximum signal change was found across all subjects at the shortest TR in both, with and without MT effects (Figure 6.1a and 6.1b respectively), which contrasts with the minimum baseline values obtained at those TRs (Figure 6.2a and 6.2b). The signal change of the wavelet packet in % in comparison to the

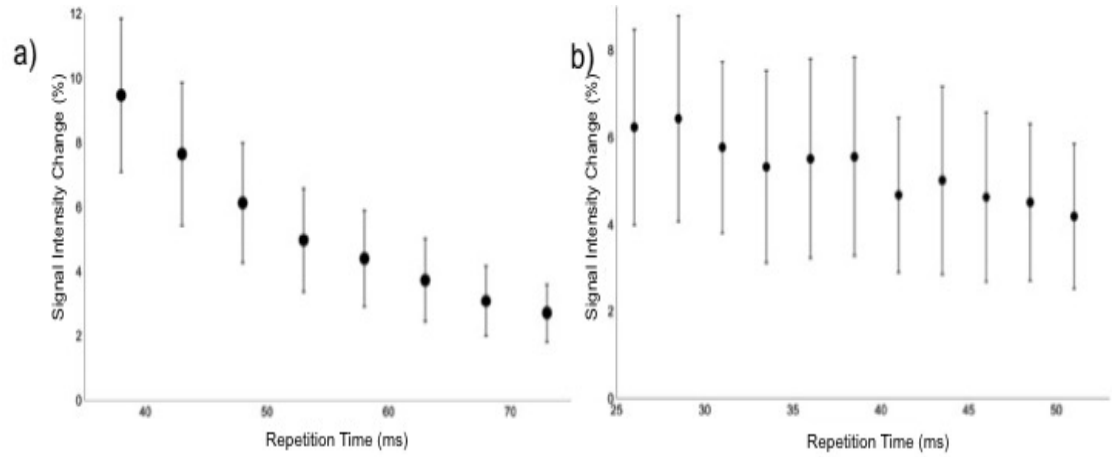

FIGURE 6.1: % of the average peak signal change of signal intensity across 5 participants with TR variations ranging from 38 to 73 ms with REST slabs (a) and ranging form 26 to 51ms with the REST slabs (b).

baseline proved to be higher with the REST slab present. In fact, as it may be seen in Figure 6.1b, the peaks strongly diminish at relatively long TR when the REST slabs are not present. However, at even longer TRs, a cardiac behaviour (i.e. a wavelet packet) is still observed with the non-UEPIS signal. In both cases, the signal intensity of the baseline increased with longer TR.

Regression of the logarithm of the signal changed amounted to $4.57713 - 0.0510129x$ and p-value (0.0734144) with the slab and $2.20359 - 0.01319x$ and p-value (< 0.001) without the REST slabs.

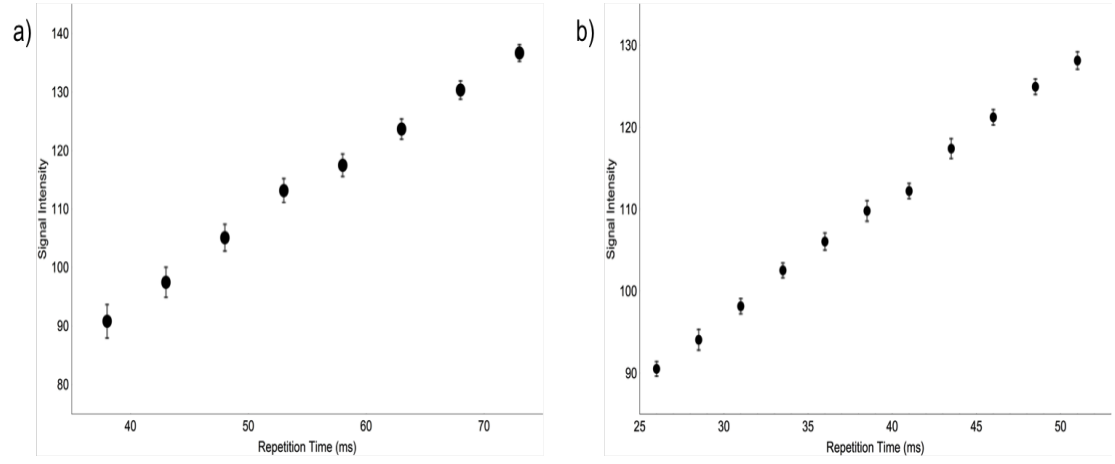

FIGURE 6.2: Average baseline signal intensity across 5 participants with TR variations ranging from 38 to 73 ms with REST slabs (a) and ranging form 26 to 51ms with the REST slabs (b).

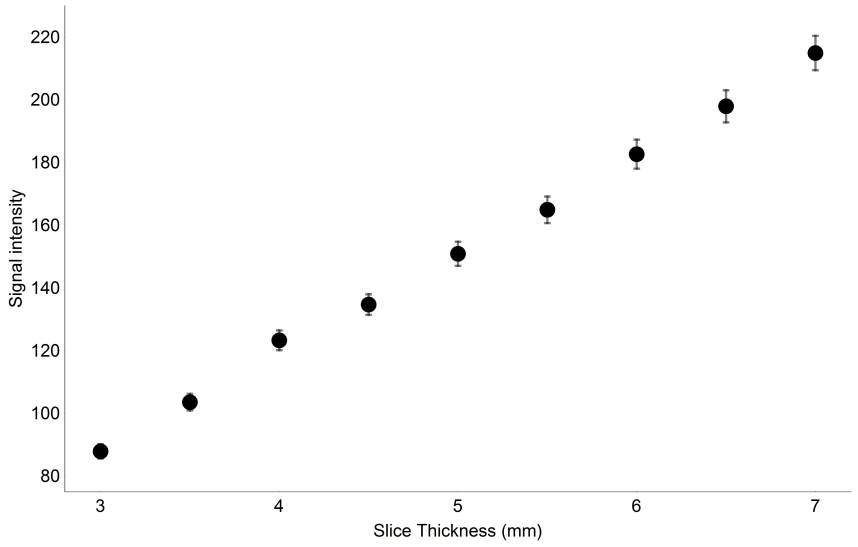

FIGURE 6.3: Average baseline signal intensity across 5 participants with slice thickness variations ranging from 3 to 7 mm.

6.1.1.2 Slice Thickness

The slice thickness evidenced a linear increase over all participants in the baseline as a consequence of the increase of the voxel size (Fig. 6.3). Despite that, the signal change due to the peak remained constant at all thicknesses suggesting that there is no dependency with the slice thickness (Fig. 6.4). A linear regression on the % of the signal change was calculated with a value of $7.14267 - 0.00709105x$

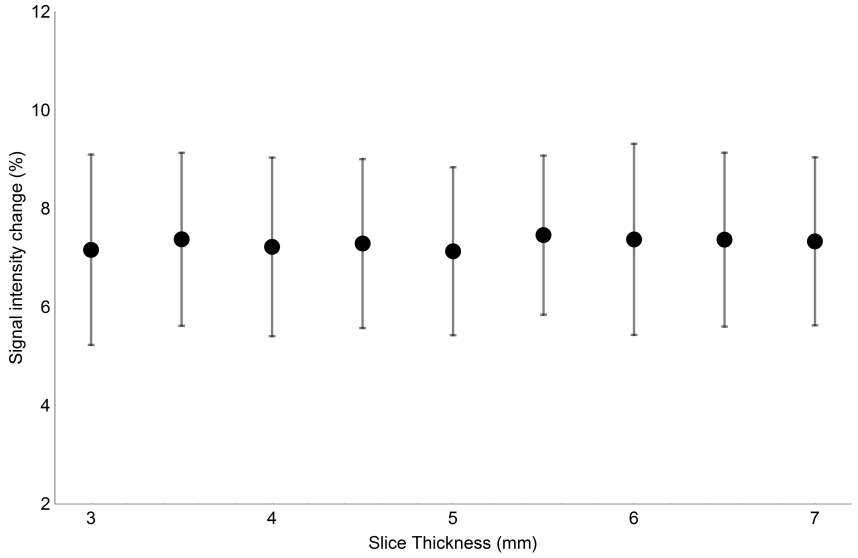

FIGURE 6.4: % of the average peak signal change of signal intensity across 5 participants with slice thickness variations ranging from 3 to 7 mm.

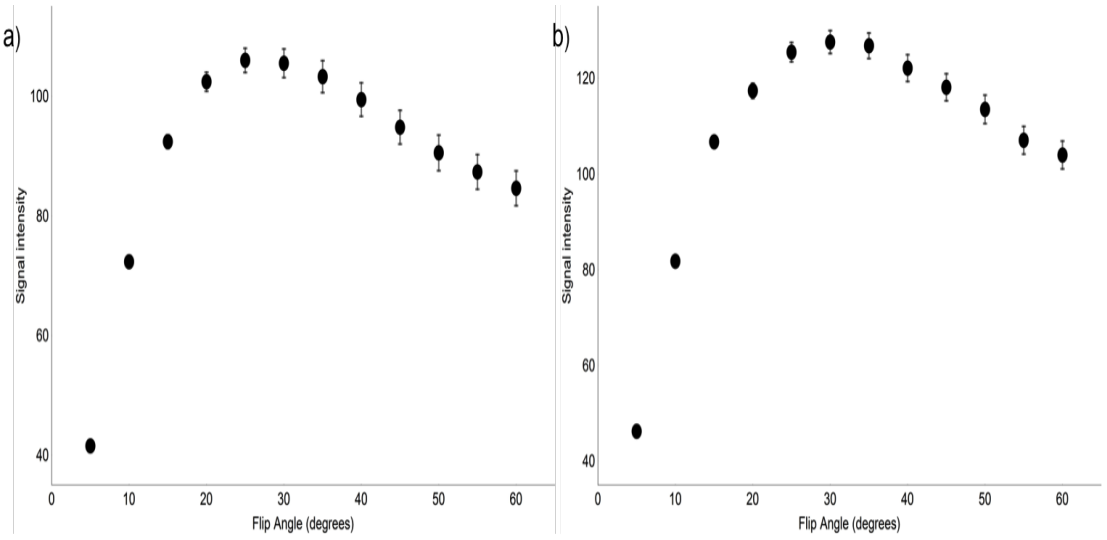

FIGURE 6.5: Average baseline signal intensity across 5 participants with flip angle variations between 5 and 60 and TR = 45 ms (a) and TR = 60 ms (b).

and p-value equal to 0.737518 proving there are not statistical differences between slice thicknesses.

6.1.1.3 Flip Angle

The baseline in the cases with the slabs kept a similar profile with a maximum around 25 and 30 degrees respectively (Figure 6.5a and 6.5b). The estimated T_1,

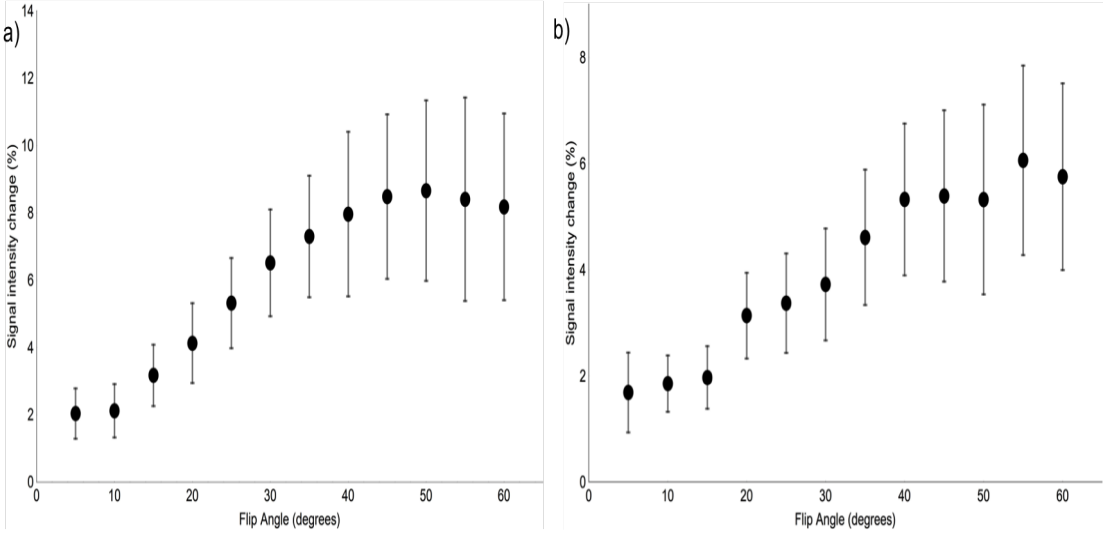

FIGURE 6.6: Average peak signal intensity change at different FA across 5 participants with flip angle variations between 5 and 60 and TR = 45 ms (a) and TR = 60 ms (b).

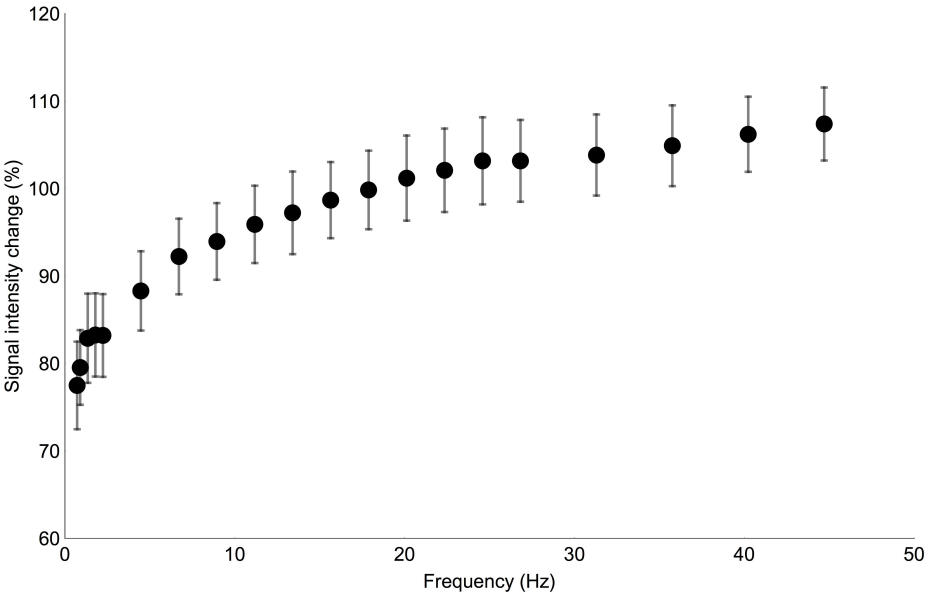

FIGURE 6.7: Average baseline signal intensity across 5 participants with frequency variations ranging from 0.7145 to 44.699 kHz.

using the Ernst able formula, with TRs equal to 60 and 45 is equal to 417.24 and 457.31 ms respectively. The wavelet peak intensity, however, displayed a delayed response in comparison to the baseline because its maxima occurred at higher values than the baseline (Fig 6.6a and 6.6b). In fact, the intensity peaks have their maximum at around 55 degrees at TR equal to 60 ms and 50 degrees at TR equal to 45 ms. The consequent T_1 values amounted 107.9340 and 101.8350 ms respectively.

6.1.1.4 Offset Frequency

Subsequently, the frequency offset of the RF pulse used to excite the REST slabs was analysed. The baseline slightly increased with higher frequency, tendency which was also in accordance with the peak intensity. The baseline of the signal changed, like one would expect, from MT saturation with stronger changes at lower frequencies (Figure 6.7). The % of the average peak signal change of signal intensity remained practically constant except at the beginning where slightly larger values were found (Figure 6.8). The linear regression was $7.36165 + 0.0508118x$ with p-value equal to 0.000720722 showing some statistical significance in terms of off-resonance frequency.

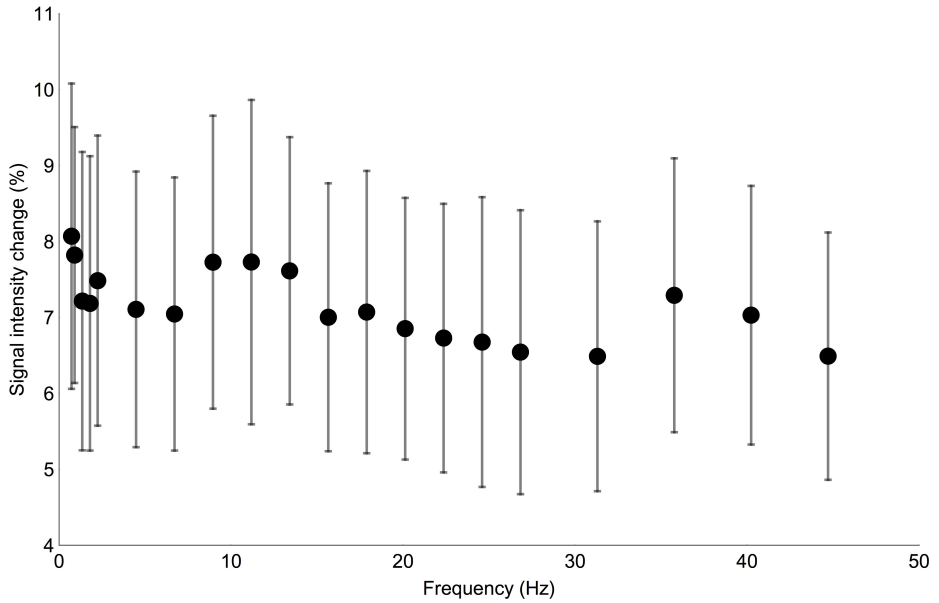

FIGURE 6.8: % of the average peak signal change of signal intensity across 5 participants with frequency variations ranging from 0.7145 to 44.699 kHz.

6.1.1.5 Echo Time

As it may be expected, it can be observed that the baseline of the signal decreased with longer TE (Figure 6.9). Following the same trend as the slice thickness, the wavelet peak signal change remained constant at all TEs (Figure 6.10). This % in signal change remained constant with a linear regression of $3.64689 + 0.00964573x$

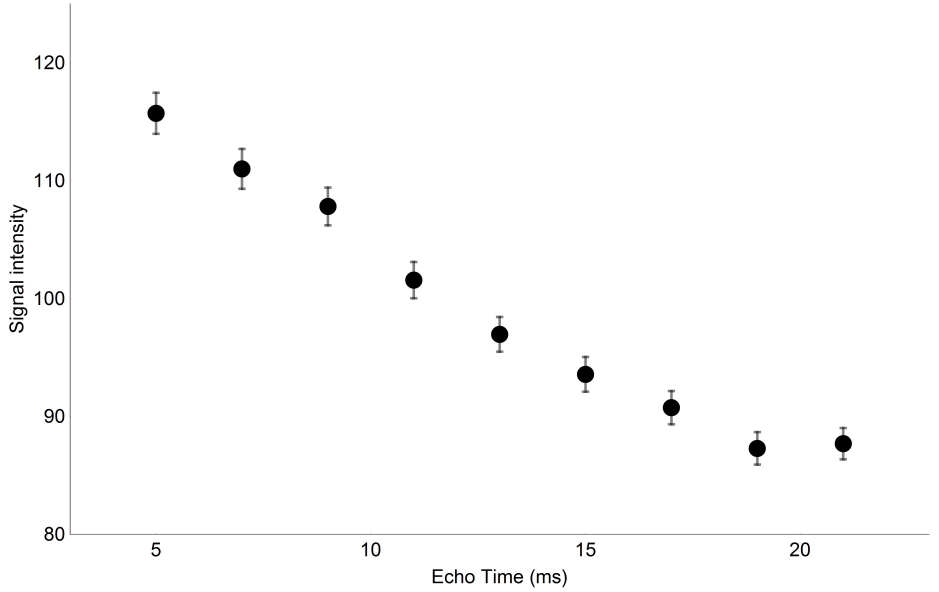

FIGURE 6.9: Average baseline signal intensity across 5 participants with TE variations ranging from 5 to 21ms.

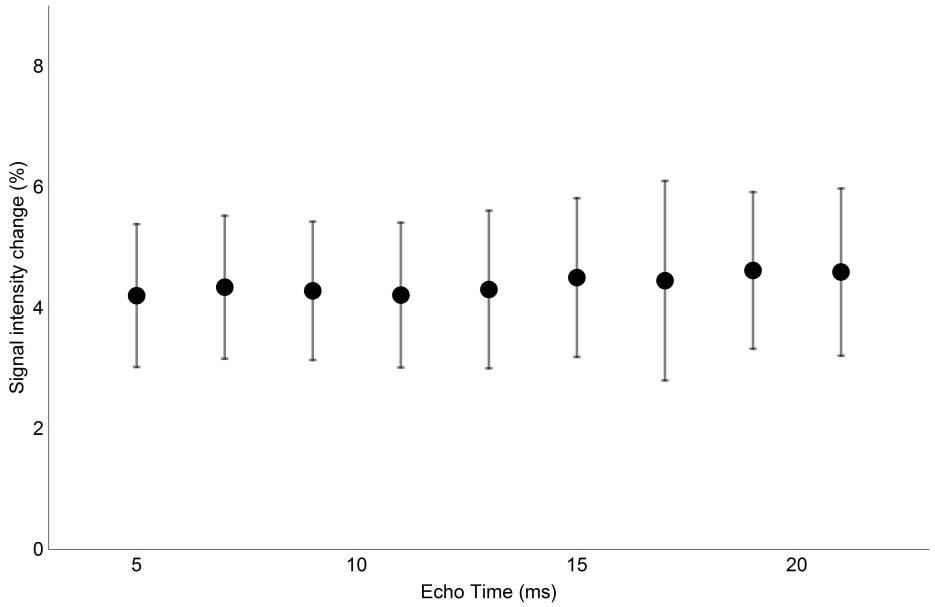

FIGURE 6.10: % of the average peak signal change of signal intensity across 5 participants with TE variations ranging from 5 to 21ms.

and a p-value equal to 0.0544898. Again, no apparent dependency with TE exists, because the peak change is balanced with the baseline change.

Linear regression on the baseline estimated a T_2* equal to 42.2472 ± 1.9772ms while the T_2* of the peaks was equal to 55.0637 ± 6.545 ms.

6.1.2 Movement Artefacts vs the UEPIS Signal

ICA was used to separate the sources of UEPIS signals. Figures 6.11 and 6.12 illustrate two of the ICA components for one of the subjects. ICA showed that the movement component can be differentiated (Figure 6.12) from the component with cardiac behaviour (Figure 6.11). The movement component is identified as an abrupt change in the time course, suggesting an abrupt head movement. Additionally, the UEPIS component offers a substantial cardiac peak in frequency domain, while the movement component, however, only forges a noisy spectra with no clear frequencies.

The analysis of 9 slices across the brain at different positions showed regions with significantly lower cardiac induced oscillations (Figure 6.13). The area highlighted

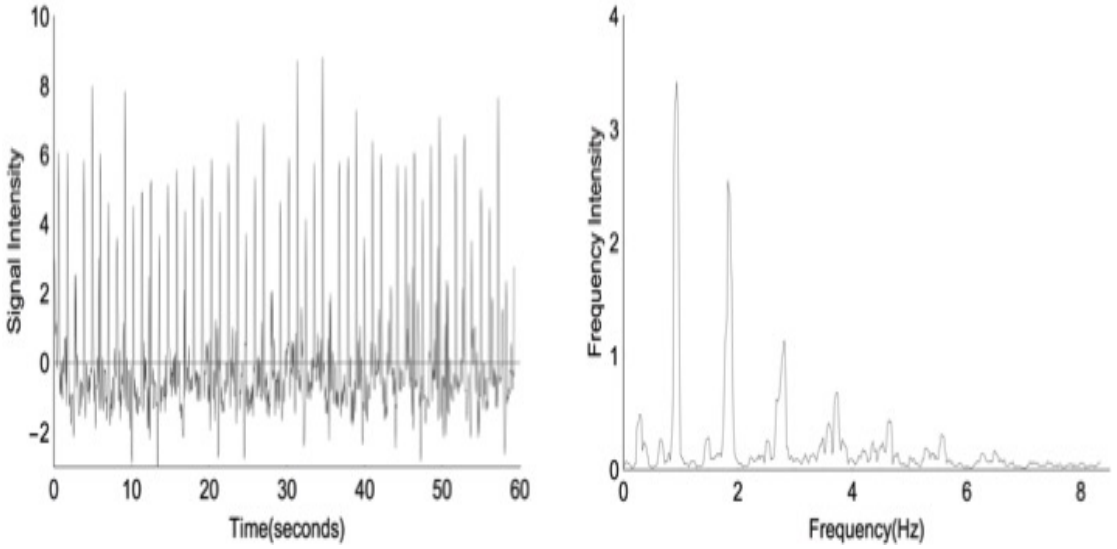

FIGURE 6.11: Example of the ICA peaks component and its frequency spectrum from one of the participants.

in red in those images represents the region with lower cardiac intensity. Figure 6.14 illustrates one example. A pixel extracted from that region had its cardiac frequency substantially lowered in comparison to a pixel located outside that area. The red areas correlated anatomically with the deep grey matter.

Finally, during hyperventilation, the participant's fast breathing induced higher head movement which affected the signal (Figure 6.15). The cardiac induced oscillations vanished during this period of strong movement while they became visible again at the end of the hyperventilation time. Identical behaviour was

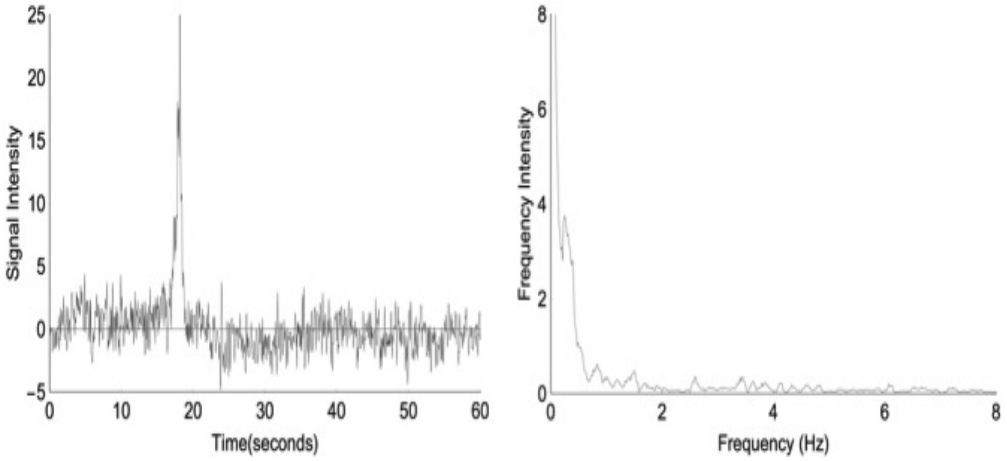

FIGURE 6.12: Example of ICA abrupt movement component from a subject in time and frequency domain from one of the participants.

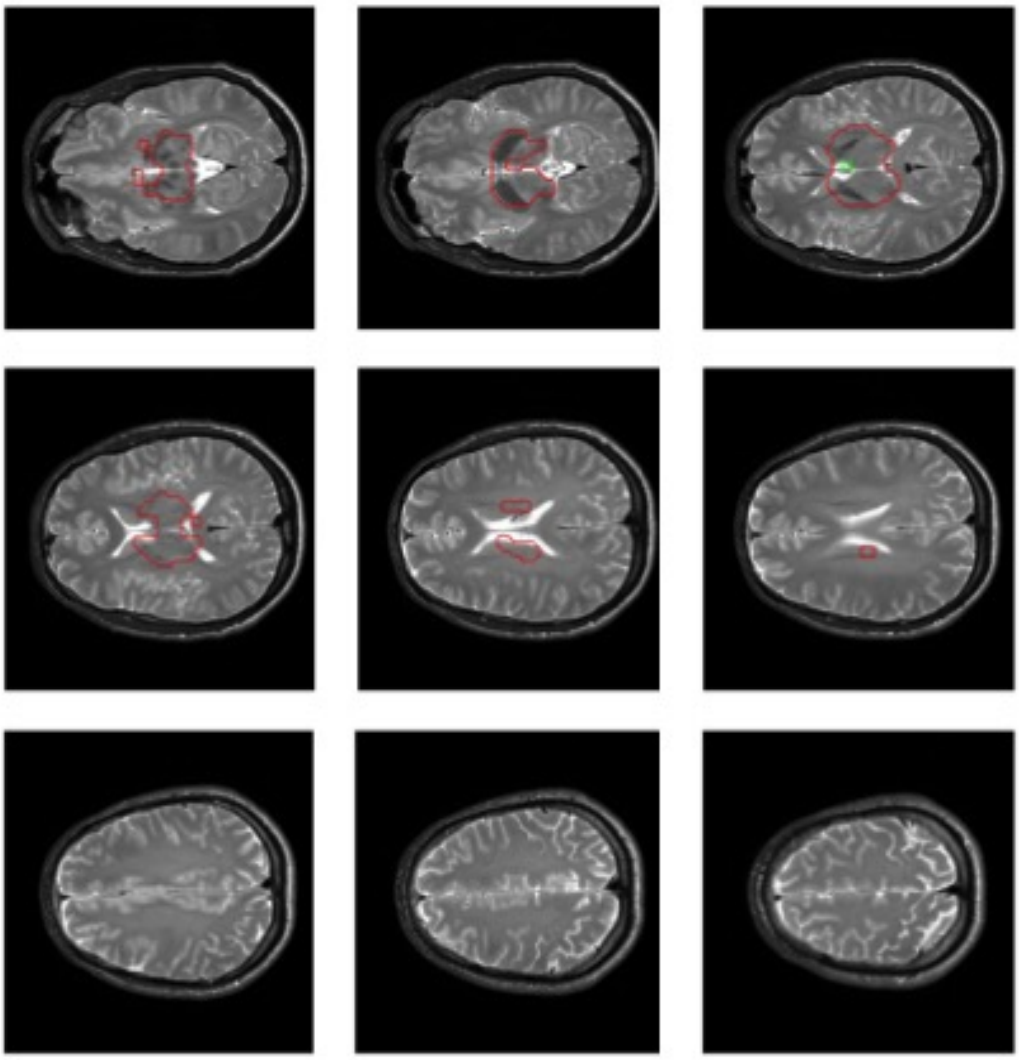

FIGURE 6.13: The analysis of 9 slices across the brain at different positions showed regions with significantly lower cardiac induced oscillations. This area with lower cardiac intensity is highlighted in red.

observed in the hypoventilation experiment (Figure 6.16). One of the participants took a deep breath prior to hold his breath, which induced a movement that can be seen in the time series at the beginning of the hypoventilation time. Besides, at the end of it, the participant breathed out and moved again, proving that head movement distorts the signal.

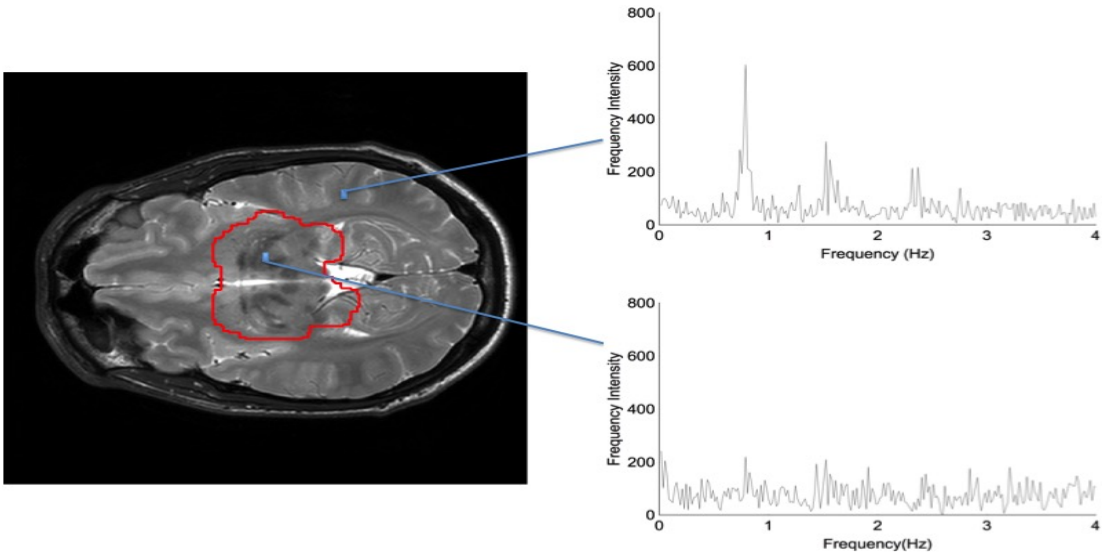

FIGURE 6.14: Example of the region marked, in red, which has a diminished cardiac response. Two spectra examples are shown for a pixel inside the region (down plot) and outside of it (upper plot).

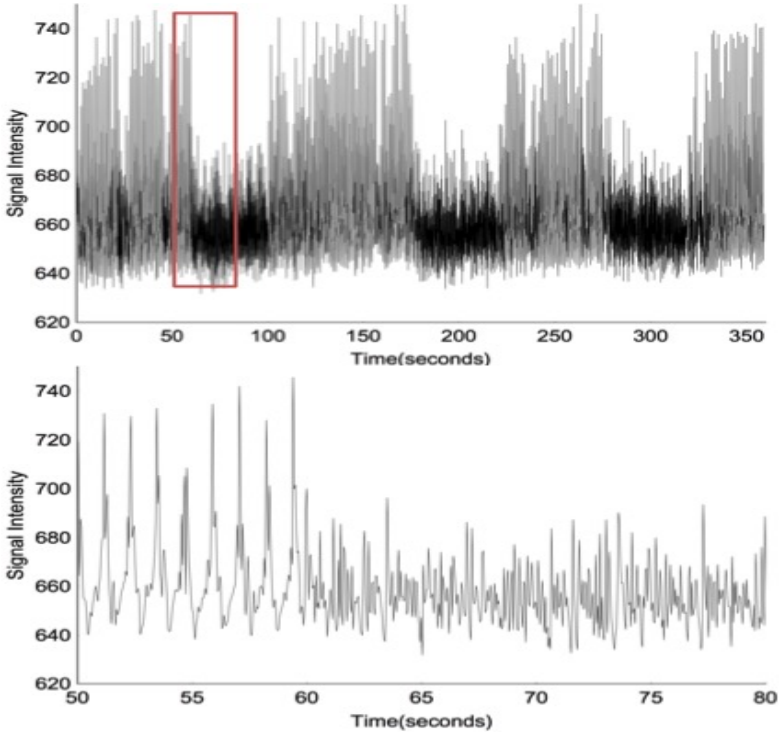

FIGURE 6.15: Average time series signal during hyperventilation. The whole time series as well as a zoomed section is described.

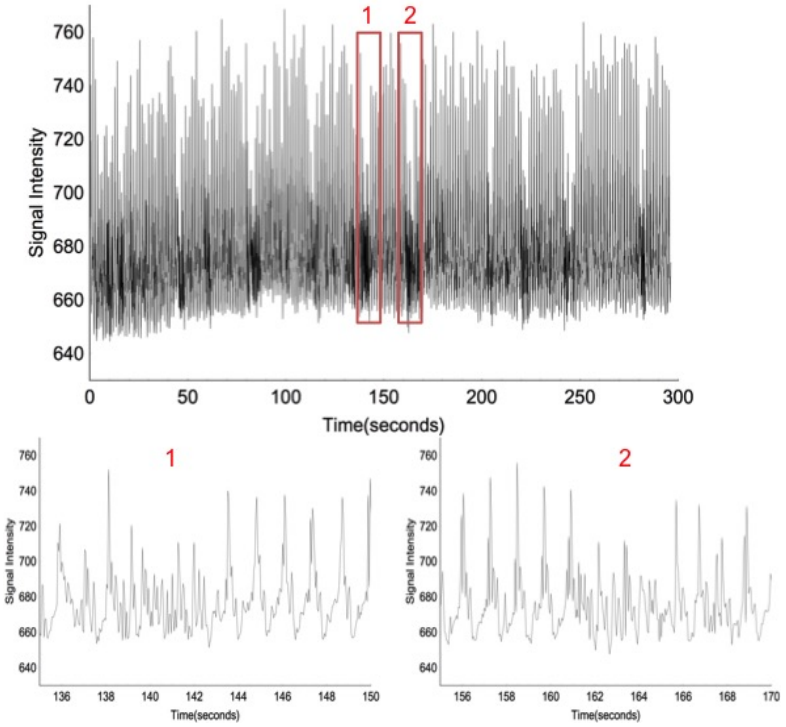

FIGURE 6.16: Average time series signal during hypoventilation. The whole time series as well as a zoomed section is described.

6.2 Discussion

The parameters of the UEPIS sequence were varied to study the possible variations affecting the signal and identify the origin of the signal mechanism. First, the TR was considered and dependency ($p < 0.05$) was found in the signal where the intensity of the wavelet packet decreased at longer TRs. The linear regressions of the TR decays with and without REST slabs showed a stronger decrease when the REST slabs were present. Secondly, increasing the slice thickness lead to a linear intensity increase of the baseline with larger slice thickness. The % of the average peak signal change of signal intensity remained constant proving that the same linear effect affects at the wavelet peak, thus, suggesting that there is no dependancy with the slice thickness ($p > 0.05$). Thirdly, analysis of offset frequency showed little dependency of the wavelet peak in relation to the offset frequency ($p < 0.05$). The % change was moderately stronger at short frequencies showing practically no change at the other frequencies. Next, the evolution of the baseline signal with the TE manifested an exponential decay. In the same way

as the slice thickness, the % change was practically constant finding once more no dependancy ($p > 0.05$). Finally, strong FA dependency ($p < 0.05$) was found, where the intensity of the wavelet packet varied with the FA. The baseline signal and the wavelet peak % change had their maximum intensity at different FA (i.e. 25-30 and 50-55 ms respectively) for both TRs. Using the Ernst angle formula the T_1 value can be estimated [43] for each TR. T_1 values equal to 457.3171 and 417.2464 ms were obtained for the baseline signal at TR = 45 and 60 respectively. However, T_1 values of the oscillation maxima were 107.9340 and 101.8350 ms.

6.2.1 Is it a Single-Quantum Contrast?

6.2.1.1 Amplitude M_0 Change

There are a few mechanisms that might generate an enhancement of the MRI signal (e.g. movement, flow effects or BOLD).

Movement Firstly, ICA was used to isolate head movements in comparison to the cardiac related peaks. The movement components are characterised by abrupt signal changes due to abrupt head movements [148]. In addition, head movements are part of the low frequency noise components which are characterised by high frequency intensity at low frequencies [149]. ICA components are a sensitive reflection of the data, thus, they also tend to be sensitive to all types of movement including abrupt changes and slow, linear drifts [148]. Therefore, it was possible to separate between a signal characterised by periodic peak whose frequency correlates with the cardiac pulsation, and a signal characterised in frequency domain by high low frequency values. It was shown that this movement component correlated to those times in the time series in where the cardiac peaks had disappeared or diminished. This finding suggested that head movement it is not the origin of the cardiac induced peak, but it distorts it. To test this hypothesis the UEPIS signal was studied under hypo and hyperventilation conditions. Normally, during hyperventilation the participant involuntary moves the head when trying

to breath faster. Figure 6.15 illustrated how this effect may be observed within the time series in relation to the disappearance of the cardiac induced oscillation peaks during this period. In addition, during hypoventilation studies one, of the participants reported to have taken a deep breath before holding if for 20 seconds. The deep breath provoked a movement prior and after the duration of the breath-holding periods as it was illustrated in the time series (Figure 6.16). Again, these results are in good agreement with the fact that wavelet packet disappears under movement conditions and it is not the movement itself that produces the UEPIS signal. What is more, independent slices were taken at different positions of the brain anatomy. The study of the cardiac peak intensity in frequency domain uncovered an area with significant low cardiac intensity. The overlapping with the anatomical images suggested that this area correlated with the deep grey matter. Studies in the deep grey matter have reported that it is an area of high movement [150, 151]. This correlates with the reduced cardiac intensity found in that area.

The TR also contradicts that the signal originates due to movement. If there is more time between RF pulses, more time is allowed for the movement to occur. Therefore, higher number of unsaturated spins would be part of the imaging slice and higher intensity should be observed. However, the signal decreases with at longer TRs. Finally, if the signal is due to movement effects the increase in the slice thickness should reduced the wavelet peak. The reason for that is that a thin slice needs a smaller movement for the spins to be replaced by unsaturated spins. The same amount of movement would affect the thicker slice to a lesser extend since there some unsaturated spins still remain. However, the % peak change remained constant at each value. Thus it might be assumed that the origin of the contrast mechanism signal cannot be considered as subject movement.

Inflow Inflow effects are also able to produce an enhancement of the signal. Nevertheless, the UEPIS signal applied REST slabs which should suppress unwanted flow artifacts from vessels entering the imaged slice [33]. Spins flowing through REST saturation bands are flipped into the transverse plane and then have their transverse magnetisation dephased by spoiler gradients [64]. When these spins

flow into the imaging slice they are already saturated and give zero signal [64]. Thus, the intensity of the peak should be at least equal or even larger when the data was acquired without REST slabs. However, figure 5.3 contradicts this idea because the intensity of the peak was considerable smaller without the employment of the REST slabs. In addition, increasing the flip angle decreases the signal from static tissue due to greater saturation and increases the relative signal from blood at the entry slice [37]. However, the wavelet peak had a maximum at FA equal to 50 degrees and decreased afterwards, contradicting that the UEPIS signal arises from inflow effects. Additionally, maximum inflow enhancement occurs when all the blood in the slice replaces that present in the slice [38]. Therefore, the signal change with thinner slices should be higher. Nevertheless, the % of signal change stayed unchanged for all values proving that the UEPIS signal is not due to inflow effects. Finally, inflow effects happen if the blood affected by the first RF has left the slice and has been replaced by new flowing spins when the next RF pulses is applied. If there is more time between RF pulses, a stronger increase of the signal will be observed because there is more to for the unsaturated spins to flow in. However, the signal decreases with longer TRs. Thus, inflow can be also discarded as the origin of the contrast mechanism.

6.2.1.2 Relaxation Times

T_1 relaxation Theoretically, the longer TR the higher T_1 relaxation occurs, which leads to an enhancement of the MRI signal [33]. However, although the baseline signal increases, the cardiac induced oscillation peak did not follow the same trend and the signal from the baseline hinders the response of the oscillation at longer TRs. One explanation could be that the T_1 value of the peak is considerably shorter than the T_1 value of the water spins in tissue. Thus, it is necessary to saturate the signal from the tissue water spins in order to be able to observe the signal from the wavelet packet. Hence, that the REST slabs are important. As it was introduced in Chapter 5, the RF excitation of the REST slabs causes off-resonance MT effects in the imaging slice. Therefore, the baseline signal decreases attributable to the exchange between the free spins and the bound

spins at that frequency [57]. This decreases might be considered as an additional saturation of the signal. The combination of the saturation effects at short TRs with the off-resonance MT due to the excitation of the REST slabs is key to obtain a strong wavelet peak.

In addition, using the Ernst angle relation [43], it has been proved that both signals (i.e., the baseline and the % of change) have different T_1 values. Thus, they also have different relaxation curves, one being faster (i.e. cardiac induced oscillation) than the other (i.e. baseline signal). Applying strong saturation to the signal, the fast component will still have time to recover while the lower will not have relaxed as much. In this way, the signal from the cardiac wavelet will occur. Otherwise, if enough time passes so the baseline signal relaxes back, the effect of the cardiac wavelet will be hindered. The measure T_1 of the oscillation peak was equal to 107.9430 ms. In the literature, only hydration water (water spins that are cross-coupled with the macromolecules) has a similar short T_1 between 10 and 100 ms [37]. However, this water has a T_2 approximately between 5 and 10 ms and the estimated value for the peak was 55.0637 ms.

Although the relation $T_1 \geqslant T_2$ is true for all tissues in the brain [37, 152], it could be possible in extremely rare cases to construct molecular systems (often at low temperatures coupled to quantum baths) where T_2 is slightly greater than T_1. This occurs when spin relaxation is produced by fluctuating microscopic fields, that are mostly transverse rather than longitudinal, often involving the antisymmetric components of the chemical shift tensor [153]. But this requires complex molecular systems that cannot exist under normal circumstances in brain tissue.

T_2 relaxation and T_2^* relaxation: BOLD A signal enhancement can be caused by dephasing due to T_2 or T_2^* relaxations. The T_2^* of both, the peaks and the baseline, were close and no significant differences were found between them. This proves that the T_2* can not be the origin of the enhancement

Moreover, another effect, related to the T_2^* dephasing and may cause an increase in the signal, is the BOLD effect. This concept is used in brain activation studies that

are based on the assumption that stimulated tissue undergoes an increase in blood flow with an increased delivery of oxygenated hemoglobin [33]. The amount of deoxygenated hemoglobin decreases within the tissue, reducing the concentration of paramagnetic molecules. This condition reduces the amount of susceptibility dephasing induced and thereby increases the T_2^* for the stimulated tissue relative to the unstimulated tissue [38]. As a result, there is an increase in the signal intensity. Despite that, fMRI studies have argued that the BOLD effect takes approximately 3 seconds [154] and here the effect is immediately related to each cardiac cycle. Furthermore, the deoxygenated blood has an optimum TE value just about 30 ms and the UEPIS experiments employed in most cases TE equal to 5 ms which reduces the BOLD effect [155].

6.2.1.3 Magnetisation Transfer

The excitation of the REST slabs requires two off-resonance pulses. This pulses induce MT effects into the imaging slice. The importance of these MT effects resides in the enhancement that introduced in the UEPIS signal. It could be argued that the input pressure wave stops for a very short moment the energy exchange between the bound and free water protons, originating the strong peak. However, it was shown that there is no dependancy between the intensity of the cardiac induced oscillation and the offset frequency. This rules out MT effects, as the origin of the contrast of the oscillation.

6.2.2 Other Contrast Mechanisms

The UEPIS signals have been proven not to arise from flow, movement, BOLD effects or phase shifts. In addition, we have seen that the TR and FA effects on the UEPIS signal behave differently from the effects observed in conventional MRI theory. There are still two possible explanations for this behaviour: double quantum effects between water protons and free radicals. The mechanism in both cases is essentially the same (i.e. the Overhauser Effect) [73, 74].

6.2.2.1 The Nuclear Overhauser Effect

NOE population changes occur due to contributions of the three dipolar relaxation processes and the balance between them depends on molecular tumbling [73]. It has been proved that the UEPIS measures the response of the tissue to pressure changes. This cardiac pressure wave can affect the normal tumbling of the molecules which may influence the rotational frequencies of the spin-spin interactions [74]. If that is the case, it was shown in equations 2.21-24 that the relaxation time will also be affected because of its dependancy from this rotational frequencies. In mobile solvents, molecular motion is much faster than the Larmor frequency [74]. Under these conditions, the DQ relaxation is more effective than SQ or ZQ, because there is a better match between the Larmor frequency and the DQ relaxation process than between the Larmor frequency and SQ relaxation process[74] . In ZQ, a mutual spin flip occurs between populations which derives into a decrease of the signal (i.e. Negative NOE). On the other hand, in DQ the spins relax in the same direction which results in an increase of the signal (i.e. Positive NOE). Therefore, it could be hypothesised that the contrast mechanism of the UEPIS signal is due to DQ effects. However, further research is needed to confirm this hypothesis.

Part IV

Applications of the Non-Single Quantum MRI Sequence

Chapter 7

Non-Single Quantum MRI in Ageing

7.1 Introduction

Extensive research has been devoted during the last decades to unravel the mechanisms behind ageing. As we age, several processes profoundly impact the brain and the heart at multiple levels, ranging from sub-cellular to macro-structural. For instance, in the brain, ageing causes deterioration of neuronal and mitochondrial membranes, which leads to the loss of cellular integrity and impaired neuronal function [156], reduction of brain volume [157] or cortical thickness [158]. At the same time, the cardiac dynamics are altered, which influences the brain metabolism [159]. Generally, normal ageing is linked to diminished cerebral blood flow or hypoperfusion to the brain. As a consequence, blood vessels thicken and become less elastic with advancing age, which increases the resistance to the flow leading to an increase in blood pressure [160]. Blood vessels damaged by hypertension lose their ability to nourish cells, which may influence the brain function. In fact, decreased cerebral blood flow with age, is related to higher risk for neuronal injury and death, blood brain barrier disruption [161], cerebrovascular pathologies [162], and cognitive deficit [163, 164].

A wide range of methods has been used to quantify the effects of ageing. For instance, MRI voxel-based morphometry is used to find structural changes [165], diffusion tensor imaging (DTI) to study regional changes in tissue properties such as tissue microstructures [166] or Arterial Spin Labeling (ASL) to measure perfusion changes [167]. However, the relation between heart and brain has not been analysed using a fast cardiac related MRI technique. Therefore, here, UEPIS will be used to study the interplay between heart and brain. It is possible that UEPIS allows the measurement of water dynamics in the brain tissue which depends on cell integrity and on cardiac pulsation to shed more information about brain ageing.

7.2 Material and Methods

7.2.1 Data Acquisition

UEPIS was applied to study the effects of ageing in the signal. 60 subjects (29 between 18 and 29 years old, and 31 over 65 years old) were scanned with the protocols approved by the St. James Hospital and the Adelaide and Meath Hospital, incorporating the NationalChildrens Hospital Research Ethics Committee. Two REST slabs of 5 mm in thickness were placed parallel to the imaged slice. The first one was located above the imaged slice at a distance equal to 15 mm. The second one was placed below separated by 20 mm. These slabs are applied to suppress unwanted flow artifacts from vessels entering the imaged slice. Additionally, the excitation of the REST slabs is going to induce an RF off-resonance pulse leading, thus to introduce the MT effects. MT effects were introduced in both cases by a negative (-13411 $\pm$ 2290 Hz) and a positive off-frequency (17882 $\pm$ 2290 Hz) RF pulse. Imaging parameters were voxel size of 3.5 x 3.5 x 3 mm, TR = 60 ms, TE = 18 ms, FA = 35°, SENSE = 2 and 3000 repetitions. The location of the imaging slice was slightly angulated and always above the ventricle to avoid pulsation effects. Additional scans without MT effects were carried out for each case using the same imaging parameters.

Anatomical MRI images in all studies included a high-resolution sagittal, T1-weighted MP-RAGE (TR = 2.1 s, TE = 3.93 ms, flip angle = 7°).

7.2.2 Data Analysis

All calculations were developed in a Dell Optiplex 790 with 12 Gb RAM using Matlab 2014a (http://www.mathworks.co.uk/). All the calculations were carried out with an in-house built Toolbox (see Appendix C).

7.2.2.1 Preprocessing

Prior to any calculation motion correction could not be applied due to the single slice nature of the experiment. First, each average time series was visually inspected in search for movement. Since movement produces abrupt changes in the time series (i.e. much higher than the cardiac related peaks), these movement related peaks were manually removed from the analysis leaving the rest of the time series unaltered. In addition, the data was not smoothed to avoid removing low frequencies which may lead to the loss of information [140].

Manual segmentation was used to create a mask to remove cerebral spinal fluid (CSF) contributions. The first 100 scans were removed to avoid signal saturation effects. The manual segmentation of the masks was eroded to avoid partial volume effects at the edges.

7.2.2.2 Fractal Analysis

Multifractal Detrended Fluctuation Analysis (MFDFA) was used to quantify the fractal properties of the time series in young and old participants [130]. To estimate the fractal spectra D, 16 window lengths; from 5 to 20, were chosen. The q-order statistical moments were chosen between -11 and 11 and divided in 21 steps.

From each spectra three parameters are calculated, i.e., width of the spectra W, asymmetry A, and the position of the of the spectra maxima H. The parameter

W is calculated by subtracting the lower part of the spectra, $D(h_{min})$, to the upper part of the spectra, $D(h_{max})$ [130, 134]:

$$W = D(h_{max}) - D(h_{min}), \tag{7.1}$$

The smaller width indicates that the time series has fewer singularities and tends to be more monofractal. The second parameter, A, is calculated by subtracting the width of the $h(q > 0)$ values to the width of the $h(q < 0)$ part calculated at full width half maximum (FHWM) [134, 138]:

$$A = \Delta h(q < 0) - \Delta h(q > 0), \tag{7.2}$$

Again the lower value of A indicates that the time series has weaker singularities and tends to be more monofractal. Finally the H represents the value of h in which the singularity spectra has its maximum D_{max} [137]:

$$H = h(D_{max}) \tag{7.3}$$

The position of h_{max} moves to higher values when the stronger singularities are present.

7.2.2.3 Spectral Clustering

Spectral clustering was used in an attempt to classify the spectra of young and old participants. First the average signal across the slice was computed among all participants. Subsequently, the individual spectrum of each time series was calculated using the Matlab open function *mtcspectrum* from the spectral analysis toolkit Chronux package [168, 169]. This function uses a multitaper method which reduces estimation bias by obtaining multiple independent estimates from the same sample. Each data taper is multiplied element-wise by the signal to

provide a windowed trial from which one estimates the power at each component frequency. As each taper is pairwise orthogonal to all other tapers, the windowed signals provide statistically independent estimates of the underlying spectrum. The final spectrum is obtained by averaging over all the tapered spectra [170]. The time-bandwidth product was set to 3 while the number of tapers was 5. The sampling frequency was $\frac{1}{2TR}$. All the volumes were classified using a spectral clustering method [121]. Similarity graphs were calculated using a normal k-Nearest neighbours with 5 neighbours and sigma value equal to 1. Four clusters were computed using a normalised Shi and Malik method [123].

7.3 Results

A comparison between the time series for both age groups is shown in figure 7.1a-h. In both cases, the time series of all voxels across the slice were averaged to showcase the difference between populations. Strong cardiac constant peaks are resolved only for the young subjects (Figure F.1a-b) while for older subjects the strong cardiac peaks are diminished (Figure 7.1c-d).

The Fourier Transform of the time series was calculated in each case (Figure 7.1e-h). The frequency spectra for the young group present the strongest cardiac frequencies. However, the spectra for the older group show stronger harmonics, envelope waves or both, in addition to the weaker cardiac frequencies. These envelope waves have a beat frequency of the (cardiac frequency)/n, where n takes values of (2,3,4,6,9 ...). These results are consistent over most subjects.

An spectral clustering algorithm was used to classify the individual spectra into separate groups. Figure 7.2 shows the result of this spectral clustering. In a first step, 85% of the spectra were correctly classified into the 4 groups. It was shown within the first iteration the possibility of determining accurately if the dataset belongs to a young or old adult without previous knowledge about the frequency spectrum. Clusters 2 and 3 were entirely formed by one type of population (young). However, number 1 and 4 had participants from both populations. Cluster 1 had

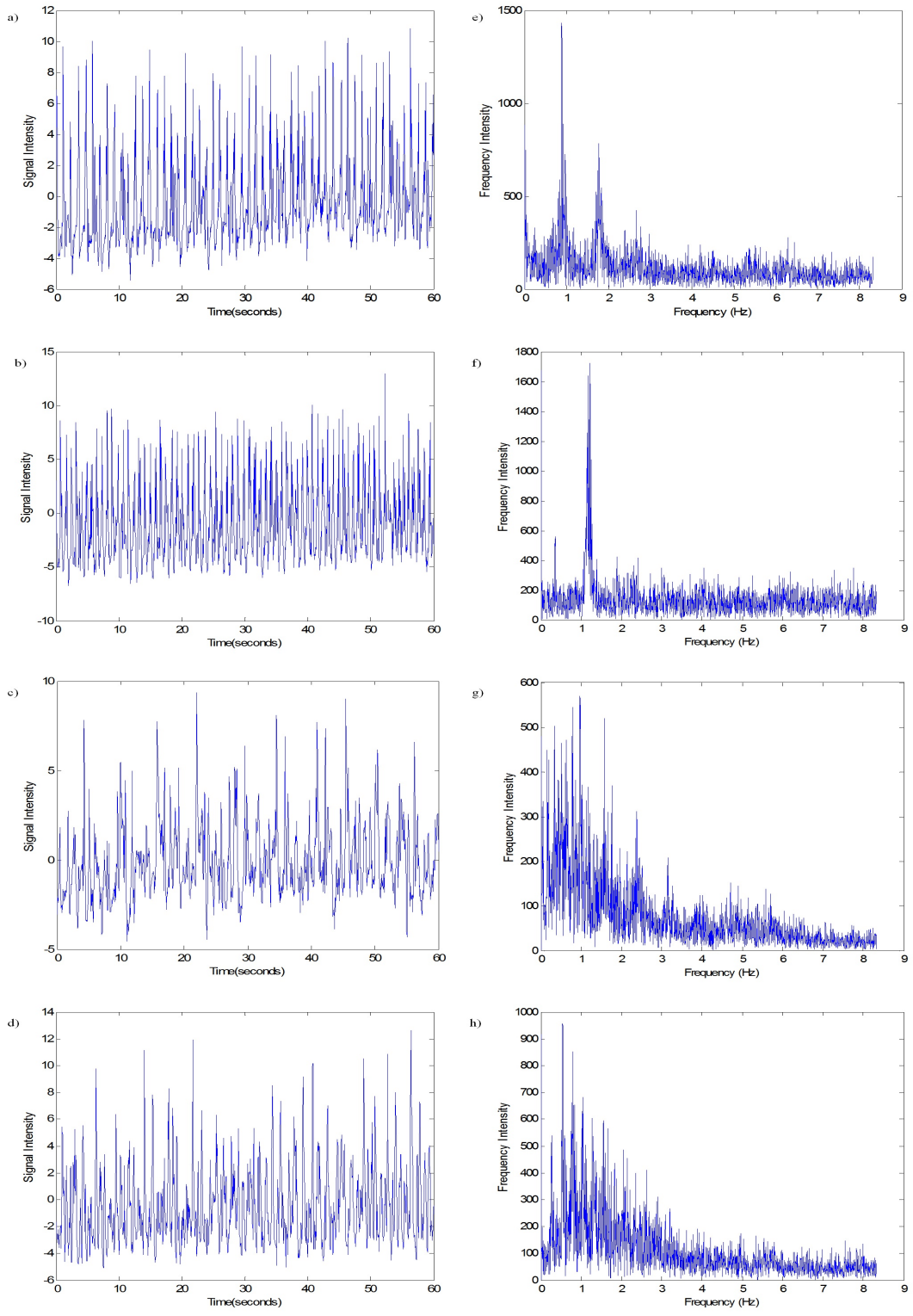

FIGURE 7.1: Example of the time series as well as its frequency spectra for two young (a-b and e-f) and two old healthy adults (c-d and g-h). These examples are representing the typical results in these groups.

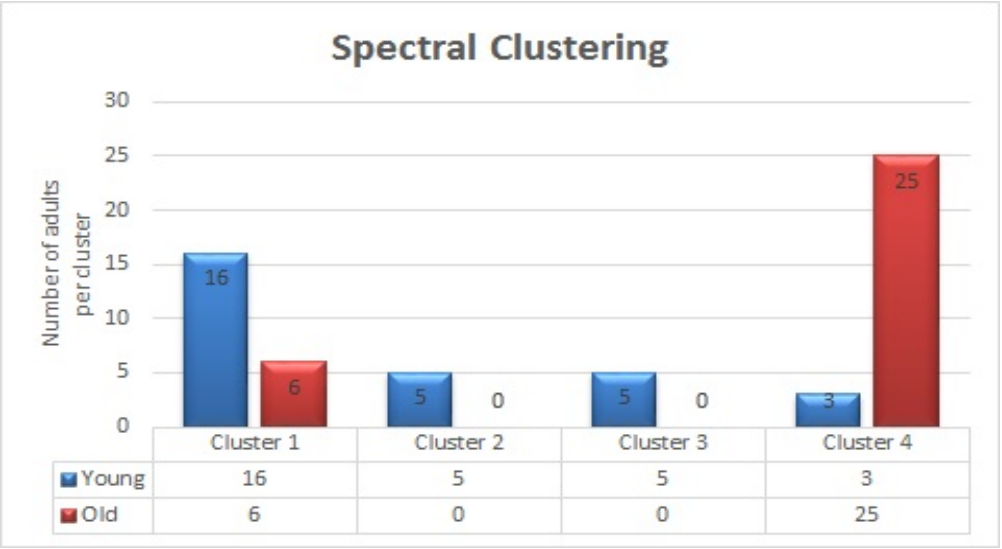

FIGURE 7.2: Result of the first iteration of the spectral clustering applied to 60 data sets.

16 young and 6 old participants, while Cluster 4 had 3 young and 25 old. Examples of the different clusters' spectra can be seen in Figures 7.3-6. Figure 7.3 shows some examples from the first cluster, which contains a mixture of young (7.3a-c) and old participants (7.3d). These spectra are mainly cardiac. Figures 7.4 and

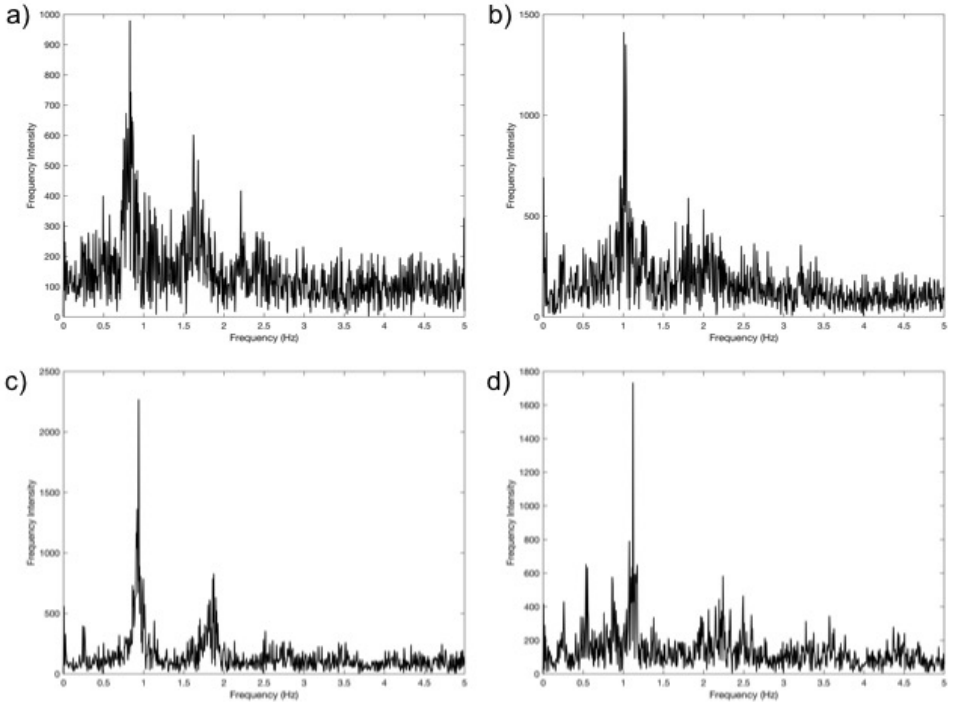

FIGURE 7.3: Examples of the spectra included in Cluster 1. Three young (7.3a-c) and one old (7.3d) participants are represented.

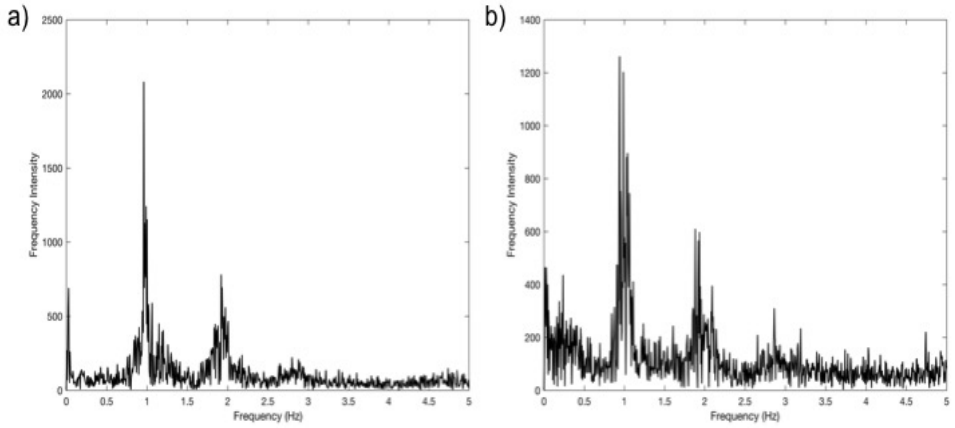

FIGURE 7.4: Examples of the spectra included in Cluster 2.

7.5 show examples of those participants classified in Clusters 2 and 3 respectively. Cluster 2 contains purely cardiac spectra without additional frequencies, while Cluster 3 includes also cardiac spectra but substantially noisier, probably due to changes in the cardiac rate during the experiment. Finally, in Figure 7.6 some examples of cluster 4 are presented. This group is mostly compounded by old participants (7.6a-c) and just a handful of young ones (7.6d). In this case, the spectra are characterised by an increase in the number of frequency components.

Finally, the result from the fractal analysis (i.e., fractal spectra) is shown in Figure 7.7. The young group has a narrower curve with a 0.9077 ± 0.1728 while the old group has an average value of 0.985 ± 0.1583. The higher width values correlates with a higher number of singularities within the time series. This fits with

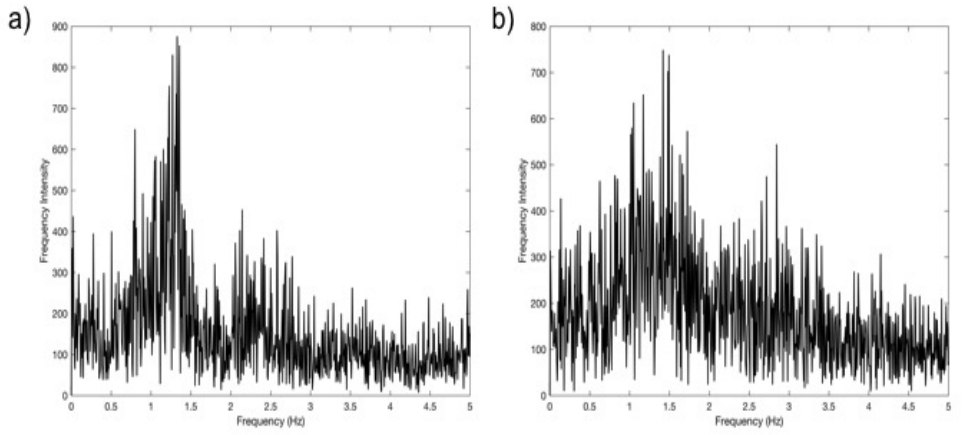

FIGURE 7.5: Examples of the spectra included in Cluster 3.

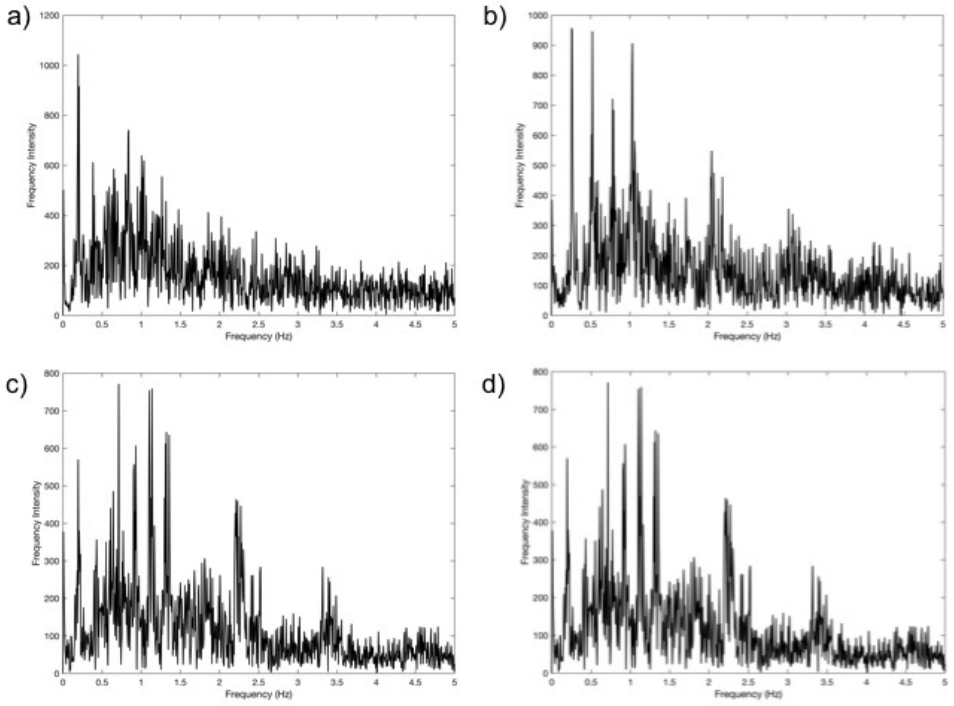

FIGURE 7.6: Examples of the spectra included in Cluster 1. Three old (7.6a-c) and one young (7.6d) participants are represented.

the position of the spectrum maxima which is at higher values for the old cohort (0.7383 ± 0.096) compared to the young one (0.6683 ± 0.0814). Again, higher values indicate a higher number of singularities present in the data. Additionally, the asymmetry represents if the time series is located in the strong or weak

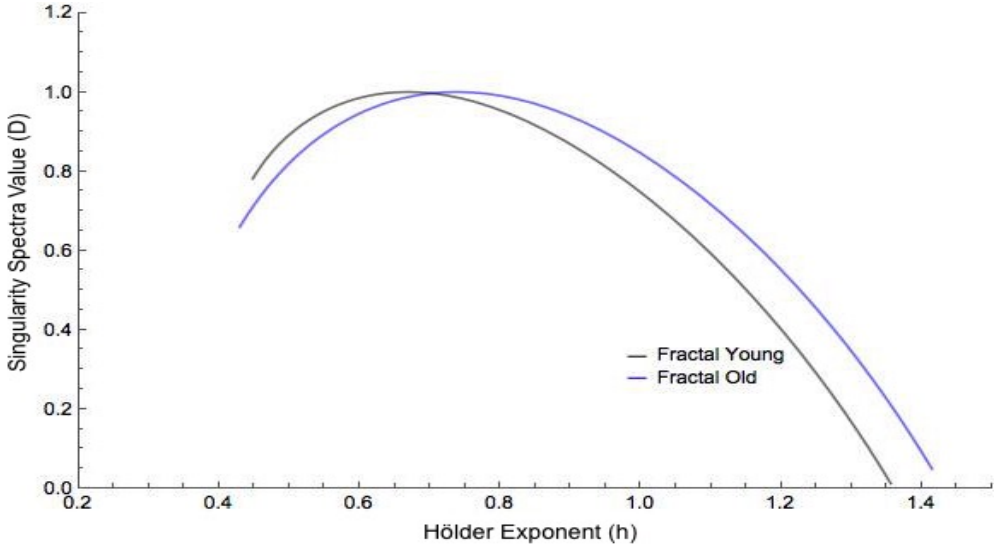

FIGURE 7.7: Result of the fractal analysis. The average spectra is shown for the young group (blue) and the old group (black).

magnitude singularities part of the spectra. The higher values found in the young group (0.4671 ± 0.1528) suggests that the time series have higher number of strong magnitude singularities than in the old one, whose value is lower (0.3669 ± 0.1072).

7.4 Discussion

UEPIS was applied to an ageing study with promising results. Strong cardiac constant peaks are resolved only for the younger subjects while for the older subjects the strong cardiac peaks are diminished. This decrease lead to stronger harmonics or envelope waves, or both, in addition to weaker cardiac frequencies. Furthermore, spectral clustering was able to classify the spectra into four clusters with an accuracy of 85%. Finally, fractal analysis showed an increase in the number of singularities in the older group.

As we age, several processes profoundly impact the brain and the heart at multiple levels. The cardiac dynamics of the brain are altered influencing the brain metabolism. For example, normal ageing is linked to diminished cerebral blood flow [160], hypo-perfusion to the brain [159] or reduction of brain volume [158]. The UEPIS signal proved to be sensitive to changes related to ageing. These changes were manifold, varying in shape, amplitude and frequency. In particular, older participants possessed a higher number of frequencies as well as a decrease in the size and number of the cardiac peaks. On the other hand, the younger group was characterised with roughly constant peaks and clear cardiac frequencies and its harmonics. Since the UEPIS signal arises from the response of the brain tissue to the input pressure wave (see Chapter 5) any change in the brain morphology or cardiac dynamics might affect this response. For example, blood vessels thicken and become less elastic with advancing age which increases the resistance to the flow leading to an increase in blood pressure [160]. This thickening of the vessels and the loss of cortical matter may affect the way the tissue responses to the pressure wave, being the peaks thus diminished. Additionally, one feature observed in the aged patients is that there are additional frequencies in the ageing data.

Taking a closer look to the time series it is noticeable that sometimes there are peaks at n (2, 3, 4...) times of the cardiac frequency (see Figure 7.6). It could be hypothesised that those peaks are correlated with the respiration. In fact, some studies have reported the so called *respiratory pump*, which is the increase in the cardiac output during inspiration [171, 172]. This can be cased by mechanisms related to respiratory cycle changes in the main magnetic field [173] and changes in arterial CO_2 pressure [174]. This could explain why a peak is significantly stronger at frequencies which might correlate with the respiration frequency. However, this could not confirmed because a respiration belt was not used in the study.

Spectral clustering was used to successfully classify the spectra of both groups in separate clusters although still some participants felt into the wrong groups. Although both groups could be separated with high accuracy, it is important to point out that not everybody ages in the same fashion and that could be the reason of those cases classified in the wrong groups. For example, there are old adults with a healthy lifestyle, that may have their cognitive functions intact. In these cases, the tissue response to the pressure wave would be stronger (see Figure 7.3d). The same thinking can be applied to the young cohort. There are young participants that may have an unhealthy lifestyle that can affect the brain dynamics (see Figure 7.6d). Further studies should take into account these possible changes and acquired more information about the cognitive status of the participants (e.g., personal questionnaires, Abbreviated Mental Test Score [AMTS], Mini-Mental State Examination [MMSE]) or even separate into different groups attending to, for instance, gender or sports activities.

Additionally, the fractal analysis of the ageing data showed differences between both groups. The fractal width and the position of the spectra maxima in the older cohort were larger than in the young one. These two parameters are related to an increase in the number of singularities in the frequency spectra[130, 138]. In fact, this increase could be expected because of the multiplication in the number of frequencies existing in the older one. What is more, the asymmetry of the fractal spectra goes to higher values when the spectrum is located in an area of strong magnitude singularities [138]. The higher value in the asymmetry of the young

group demonstrates that the singularities have higher magnitude, which is in good agreement with the stronger peaks observed within this group.

This proves that UEPIS can reveal new insights in the dynamics of the ageing brain. Moreover, its combination with existing methods (e.g. fractal analysis) might help to unravel new features in the ageing brain.

Chapter 8

Non-Single Quantum MRI in Major Depressive Disorder. A Pilot Study

8.1 Introduction

The advances in neuroscience such functional neuroimaging has been used to investigate pathophysiological mechanisms and the physiological basis of depression. Currently, more advance techniques such PET images co-registration with MRI data have been used to characterise variations in the activity of different regions[175]. It has been found through these methods, for instance, an increase number of structural abnormalities[176], differences of cerebral metabolism or blood flow in the caudale nucleus and the admygdala[177–179] or hypofrontality in the pre-frontal cortex[180]. Of particular interest are the changes in the caudate nucleus which is part of the basal ganglia. Suggestions that basal ganglia disturbances may play a part in depression also come from clinical observations where depression is associated with several neuropsychological deficits including some suggestion of prefrontal dysfunction[181]. It has been shown that depressed patients performing a complex planning task fail to demonstrate the normal control

finding of increased caudate activation with increasing task difficulty[182]. Additionally, in postmortem brain examinations of patients with mood disorders compared with controls, the patients had smaller left nucleus accumbens, smaller left and right external pallidum, and smaller right putamen[183]. Therefore, UEPIS was applied to a pilot study in which a slice across the basal ganglia was selected.

8.2 Material and Methods

8.2.1 Data Acquisition

UEPIS was also applied to study the effects of MDD in the signal. 6 depressed patients (25 and 42 years old) and 5 control subjects (26 over 34 years old) were scanned with the protocols approved by the Ethics Board of Taillight' and St. James' Hospitals. Two REST slabs of 5 mm in thickness were placed parallel to the imaged slice. The first one was located above the imaged slice at a distance equal to 15 mm. The second one was placed below separated by 20 mm. These slabs are applied to suppress unwanted flow artifacts from vessels entering the imaged slice. Additionally, the excitation of the REST slabs is going to induce an RF off-resonance pulse leading, thus to introduce the MT effects. MT effects were introduced in both cases by a negative (-13411 $\pm$ 2290 Hz) and a positive off frequency (17882 $\pm$ 2290 Hz) RF pulse. Imaging parameters were voxel size of 3.5 x 3.5 x 3 mm, TR = 60 ms, TE = 11 ms, FA = 35° and 1000 repetitions. The imaging slice was place approximately across the balsa ganglia of each participant. Additional scans without MT effects were carried out for each case using the same imaging parameters.

Anatomical MRI images in all studies included a high-resolution sagittal, T1-weighted MP-RAGE (TR = 2.1 s, TE = 3.93 ms, flip angle = 7°).

8.2.2 Data Analysis

All calculations were performed on a Dell Optiplex 790 with 12 Gb RAM using Matlab 2014a (http://www.mathworks.co.uk/). All the calculations were carried out with an in-house built Toolbox (see Appendix C).

8.2.2.1 Preprocessing

Prior to any calculation motion correction could not be applied due to the single slice nature of the experiment. First, each average time series was visually inspected in search for movement. Since movement produces abrupt changes in the time series (i.e. much higher than the cardiac related peaks), these movement related peaks were manually removed from the analysis leaving the rest of the time series unaltered. In addition, the data was not smoothed to avoid removing low frequencies which may lead to the loss of information [140].

Manual segmentation was used to create a mask to remove cerebral spinal fluid (CSF) contributions. The first 100 scans were removed to avoid signal saturation effects. The manual segmentation of the masks was eroded to avoid partial volume effects at the edges.

8.2.2.2 Fractal Analysis

MFDFA was used to quantify the fractal properties of the time series in MDD patients and healthy control participants [130]. To estimate the fractal spectra D, 16 window lengths; from 5 to 20, were chosen. The q-order statistical moments were chosen between -11 and 11 and divided in 21 steps.

From each spectra three parameters are calculated, i.e., width of the spectra W, asymmetry A, and the position of the of the spectra maxima H. The parameter W is calculated by subtracting the lower part of the spectra, $D(h_{min})$, to the upper part of the spectra, $D(h_{max})$ [130, 134]:

$$W = D(h_{max}) - D(h_{min}), \tag{8.1}$$

The smaller width indicates that the time series has fewer singularities and tends to be more monofractal. The second parameter, A, is calculated by subtracting the width of the $h(q > 0)$ values to the width of the $h(q < 0)$ part calculated at full width half maximum (FHWM) [134, 138]:

$$A = \Delta h(q < 0) - \Delta h(q > 0), \tag{8.2}$$

Again the lower value of A indicates that the time series has weaker singularities and tends to be more monofractal. Finally the H parameters represents the value of h in which the singularity spectra has its maximum D_{max} [137]:

$$H = h(D_{max}) \tag{8.3}$$

The position of h_{max} moves to higher values when the stronger singularities are present.

8.2.2.3 Spectral Clustering

Spectral clustering was used in an attempt to separate the spectra of MDD patients and healthy control participants. First the average signal across the slice was computed among all participants. Subsequently, the individual spectrum of each time series was calculated using the Matlab open function *mtcspectrum* from the spectral analysis toolkit Chronux package [168, 169]. This function uses a multitaper method which reduces estimation bias by obtaining multiple independent estimates from the same sample. Each data taper is multiplied element-wise by the signal to provide a windowed trial from which one estimates the power at each component frequency. As each taper is pairwise orthogonal to all other tapers, the windowed signals provide statistically independent estimates of the

underlying spectrum. The final spectrum is obtained by averaging over all the tapered spectra [170]. The time-bandwidth product was set to 3 while the number of tapers was 5. The sampling frequency was $\frac{1}{2TR}$. All the volumes were classified using a spectral clustering method [121]. Similarity graphs were calculated using a normal k-Nearest neighbours with 5 neighbours and sigma value equal to 1. Two clusters were computed using a normalised Shi and Malik method [123].

8.3 Results

A comparison between the frequency spectra of both groups is shown in Figure 8.1a-b. For each subject, ROI's from the basal ganglia and from the visual cortex were averaged to showcase the difference between brain regions and populations.

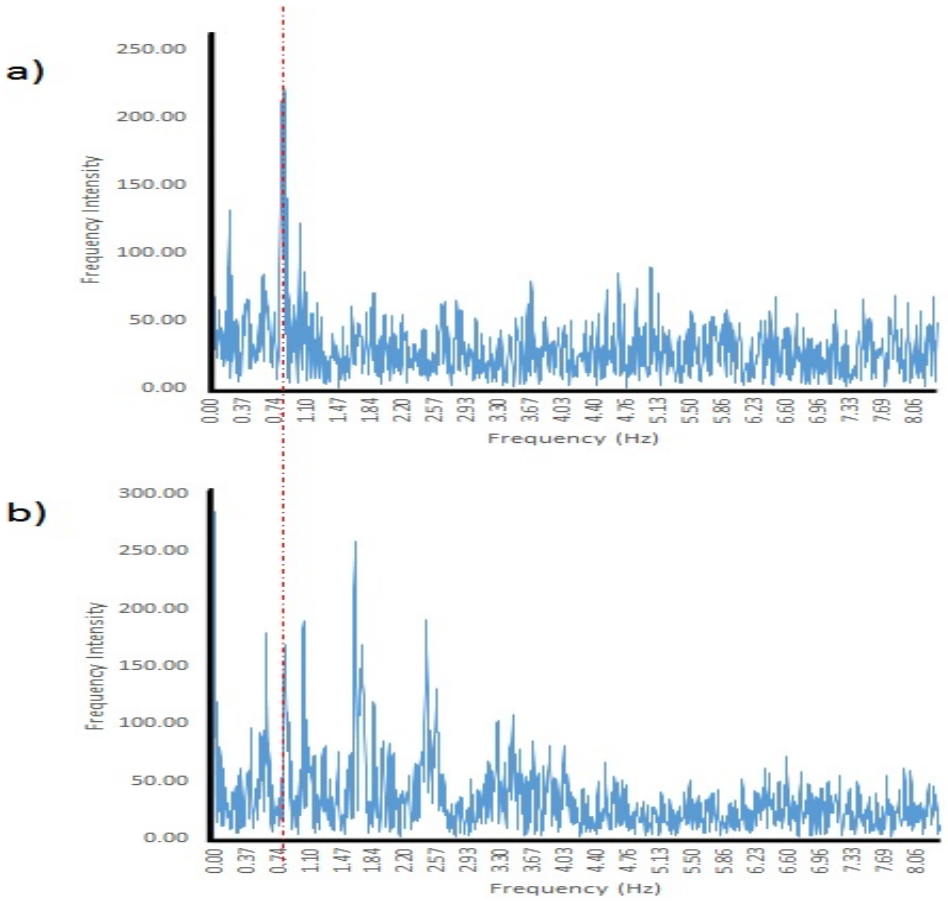

FIGURE 8.1: Frequency spectra examples from the control (a) and the depression group (b).

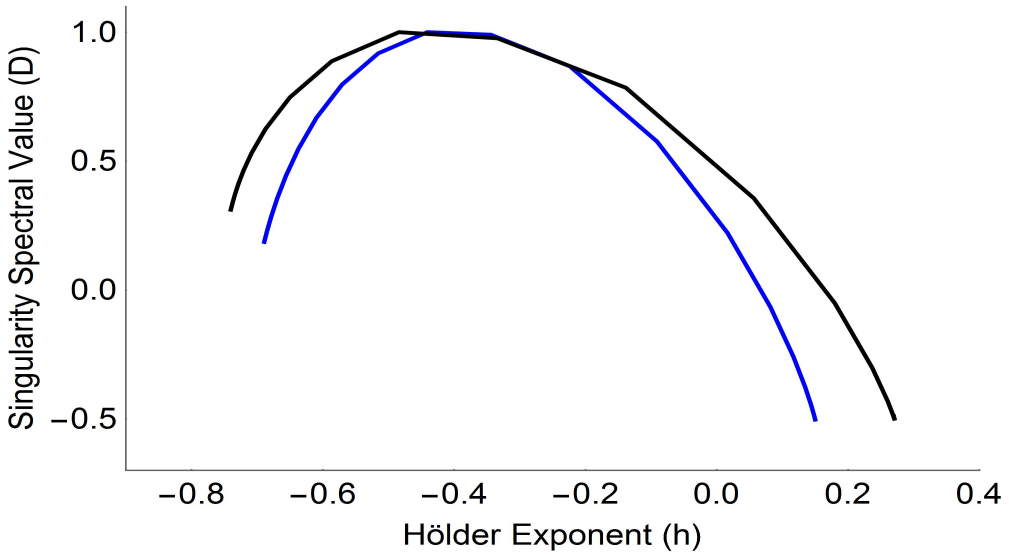

FIGURE 8.2: Fractal spectrum from the control (Blue) and the depression group (Black).

For the control group, only strong cardiac frequencies are resolved in the basal ganglia as well as the cortex (Figure 8.1a). However, the spectra for the depressed patients show lower cardiac response in general but different behaviour in the basal ganglia where we found a direct cardiac response from the tissue as well as a second response at around half of the cardiac circle (Figure 8.1b). This results in an apparent shortening by the detected frequency by a factor 2.

The average fractal spectra of both groups are shown in Figure 8.2. The black line represents the MDD patients which showed a wider width in comparison to the control participants represented with a blue line. Besides, there was also an increase in the asymmetry of the spectrum for the MDD patients. Moreover, those participants who performed worst in the Hamilton Depression Scale correlated with higher fractal values.

An spectral clustering algorithm was used to classify both groups into two separate clusters. However, the differences among both groups were not strong enough for the algorithm to separate between groups (Figure 8.3). The first cluster was formed by 5 depressed patients and 3 healthy controls, while the second cluster had 1 depressed patient and two healthy controls. Interestingly, 3 out of the 4 depressed patients with higher values in the Hamilton scale were classified in the same group (Cluster 1).

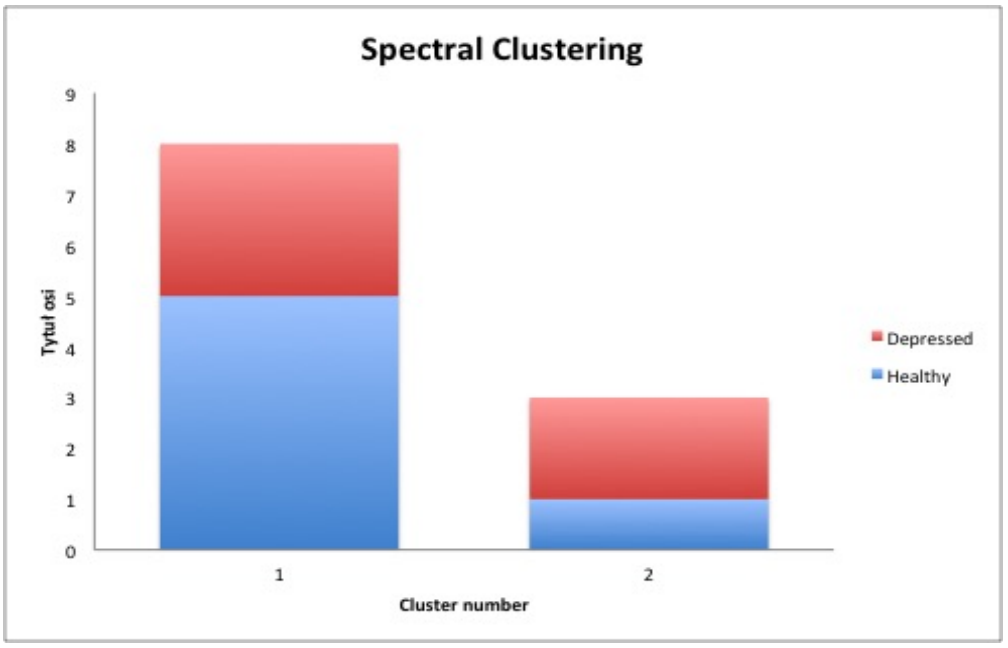

FIGURE 8.3: Results of the spectral clustering in the depression study. Two clusters were computed.

8.4 Discussion

A pilot study was conducted in a small group of MDD patients. Preliminary results suggest that there are alterations in the basal ganglia of the MDD patients. These variations are manifold, varying in shape amplitude and frequency. Additionally, fractal analysis showed increased numbers of singularities in MDD patients. However, the spectral clustering algorithm was not able to differentiate between MDD patients and control subjects.

MDD patients showed more dynamic components in the basal ganglia which may be related to tissue compartments that have a delayed response to cardiac dynamics. Previous studies have already shown that patients suffering from MDD have a variation in the blood flow dynamics [175]. For instance, changes have been observed in areas such hippocampus, pre-frontal cortex or the head of the caudate nucleus [179, 180]. This correlates with the differences found between groups since the caudate nucleus is interesting because it forms part of the basal ganglia which was analysed in this study. However, the use of one slice complicates the study of one particular area. This could induce variability in the results across all the

participants. Different slices should be acquired in future studies to cover a large region and improve the comparison between groups.

The fractal analysis of the time series inside the slice showed an increase number of singularities in the MDD patients compared to the control subjects. This could be expected, as happened in the ageing study, since the spectra showed more frequency components, and thus, more singularities in the time series might be expected. This variation of the brain dynamics may be because of the decreased perfusion in this area, as found in other studies [175]. Additionally, this area is highly connected with the pre-frontal cortex which is also strongly affected in MDD [184]. It was particularly interesting that the cases with higher fractal parameters correlated well with the Hamilton depression scale. 3 out of the 4 cases with the highest values in the Hamilton scale (i.e., scores around 30 or over) showed the highest values in the fractal analysis. Additionally, the asymmetry parameter, however, was higher in the control patients showing that the singularities present in this group are stronger in magnitude. This fits with the observation that the time series have stronger cardiac induced oscillations in the control group.

However, the spectral clustering results were not as good as in the ageing study and clustering separation was not possible. Probably the proximity in age between the subjects produces the cardiac dynamics, although altered in MDD, do not differ strongly. In addition, the position of the slice was across the basal ganglia which is part of the deep grey matter. It was shown in Chapter 6 that the UEPIS signal was perturbed in that region due to high movement. Therefore, the quality of the signal was not as good as one presented in the other areas of the brain (i.e. motor cortex, visual cortex...). and results are probably contaminated with movement effects. Future studies should focus on areas such the prefrontal cortex also affected in depression and which suffers from less movement.

Although this was a pilot study, it suggests that UEPIS might reveal new insights in the brain dynamics of the depressed brain. However, only a small group was studied and larger groups are needed to confirm this hypothesis. In combination

with existing methods (e.g. fractal analysis) might help to shed more light about the brain dynamics in the depressed brain.

Chapter 9

Non-Single Quantum MRI in fMRI

9.1 Introduction

Since its creation in 1990 [65] then and during the last two decades BOLD fMRI has emerged as the foremost method for visualising not only brain activity. It has been possible not only to quantify the relation between Cerebral Blood Flow (CBF) and cerebral blood volume (CBV) with the BOLD signal [185], but also the analysis of the time course of the BOLD signal has widened our understanding about brain activation [154, 186, 187].

In spite of its extended use there is, however, certain reluctancy present against the BOLD signal and its accuracy to represent the real activation. It is well known that the BOLD signal relies on the paramagnetic properties of the deoxy-hemoglobin (dHb). During activation the increase in the consumption of oxygen is accompanied by an increase in the fully oxygenated blood. Therefore it would be expected an increase in dHb and consequently a decrease in the MRI signal. However, there is a decrease in the concentration of dHb downstream from the site of activation leading to an increase in the $T2^*$ value and therefore an increase in the MRI signal [38]. This increase is due to the overcompensation by CBF [71].

Since the BOLD signal is detected in the downstream from the site of activation and therefore in venules or veins, a debate opens about the spatial correspondence between the actual site of neural activity and the extent of the metabolic and hemodynamic response.

A recent paper by Renwall et al. [155], has pointed out that all that glitters is not BOLD by analysing the variations of the BOLD signal under different acquisition parameters. They concluded that the contributions to fMRI signals can be disambiguated by applying multiple acquisition parameters during the same experiment. Additional studies have used multi-echo sequences in order to denoise the BOLD signal from the non-BOLD derived from physiological contributions and motion artefacts [188, 189]. All these studies might point out that the real activation slightly differs from what we see in BOLD studies and more needs to focus on the accuracy in the spatial location of the BOLD response. Therefore, UEPIS is applied to determine the changes during activation.

9.2 Material and Methods

9.2.1 Data Acquisition

Two fMRI protocols were carried out in 4 subjects to check whether there are changes in the UEPIS signal during activation. First, a finger-taping protocol was carried out to measure activation in the motor cortex. Thus, each subject was told to move two fingers after a light appear on the screen and stop when the light switched off. The finger-taping lasted 12 seconds followed by 24 seconds of rest in each case (Fig. 9.1). Second, and flicker paradigm was used to activate the visual cortex. After each resting block lasting 18 seconds a 18 seconds flicker block followed (Fig. 9.2). The flicker had a 5 Hz frequency. Five rest blocks and 4 activations were acquired for each run. MT effect was introduced by a negative (-13411 $\pm$ 2290 Hz) and a positive off frequency (17882 $\pm$ 2290 Hz) RF pulse.

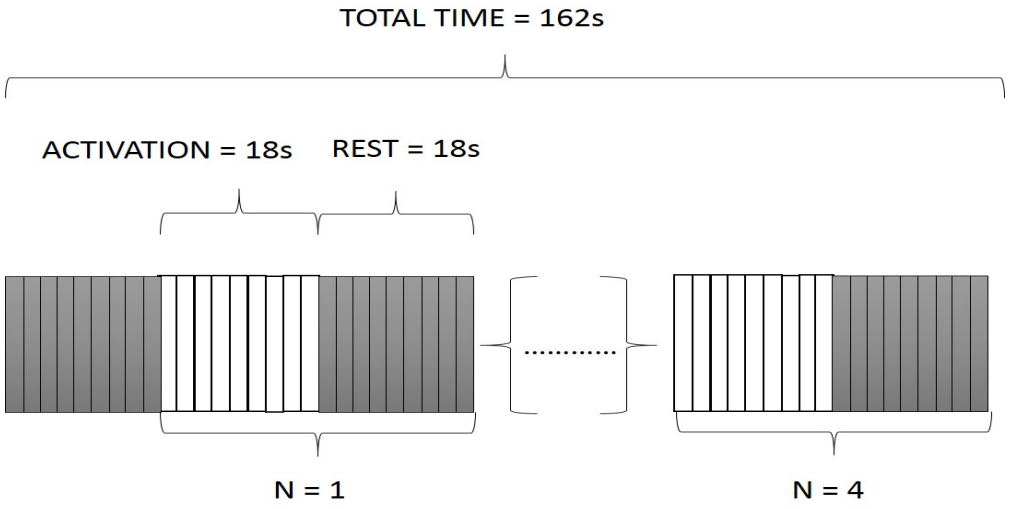

FIGURE 9.1: Visual Cortex Paradigm. A flicker stimulus lasting 18 seconds was followed by 18 seconds of rest. The experiment was repeated four times.

Imaging parameters were voxel size of 3.5 x 3.5 x 3 mm, TR = 60 ms, TE = 11 ms, FA = 35° and 2800 repetitions.

A real time BOLD fMRI scan was ran prior to the UEPIS studies to determine the location of the imaging slice. The slice with stronger BOLD signal was selected as imaging slice for the UEPIS sequence. The real time BOLD fMRI sequence was a normal EPI with TR = 2 s, TE = 30 ms, FA = 90°, voxel size of 3.5 x 3.5 x 3.5 mm and 60 repetitions.

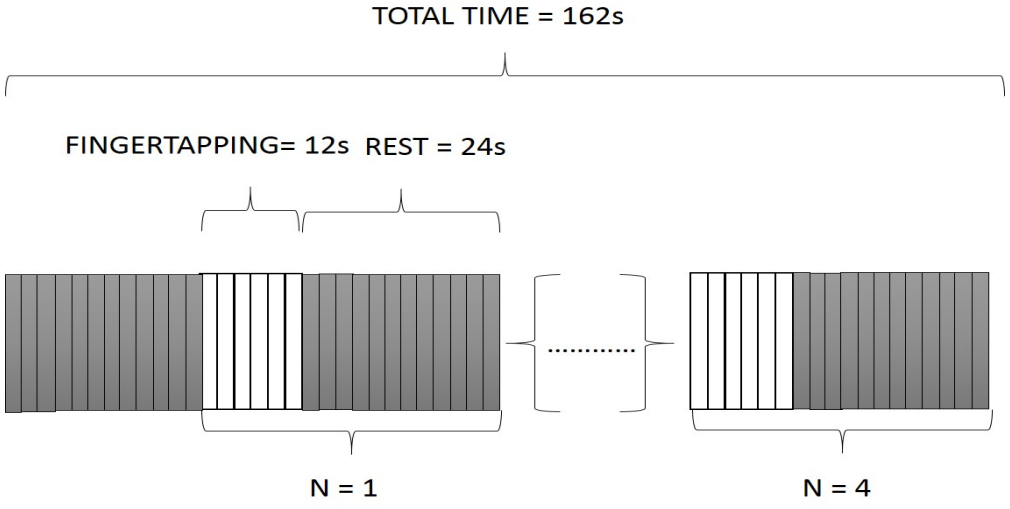

FIGURE 9.2: Motor Cortex Paradigm. A finger-tapping activation of 12 seconds was followed by 24 seconds of rest. The experiment was repeated four times.

Anatomical MRI images in all studies included a high-resolution sagittal, T1-weighted MP-RAGE (TR = 2.1 s, TE = 3.93 ms, flip angle = 7°).

9.2.2 Data Analysis

All calculations were developed in a Dell Optiplex 790 with 12 Gb RAM using Matlab 2014a (http://www.mathworks.co.uk/). All the calculations were carried out with an in-house built Toolbox (see Appendix C).

9.2.2.1 Preprocessing

Prior to any calculation motion correction could not be applied due to the single slice nature of the experiment. First, each average time series was visually inspected in search for movement. Since movement produces abrupt changes in the time series (i.e. much higher than the cardiac related peaks), these movement related peaks were manually removed from the analysis leaving the rest of the time series unaltered. In addition, the data was not smoothed to avoid removing low frequencies which may lead to the loss of information [140].

Manual segmentation was used to create a mask to remove cerebral spinal fluid (CSF) contributions. The first 100 scans were removed to avoid signal saturation effects. The manual segmentation of the masks was eroded to avoid partial volume effects at the edges.

9.2.2.2 Mean Maximum Peak Detection

The intensity of the mean maximum peak was calculated by subtracting the mean baseline to the mean peak values. The detection of the peak maxima is based on the method proposed in Gomes and Pereira 2013 [141]. The method uses the open function *peakdet* implemented in Matlab, to detect all the local maxima of the temporal signals. The mean baseline signal will be the mean value of the

remaining time points (i.e. the peak maxima were excluded to compute the mean baseline).

During activation the haemodynamics changes such cerebral blood flow (CBF), cerebral blood volume (CBV) and changes in the CO_2 consumption are linked spatially and temporally to the duration and the location of the activation. As a result, in fMRI there is a signal increase due to the change of deoxyhemoglobin. This signal change needs to be taken into account when calculating the peak-to-baseline value. Thus, a linear fitting is applied to the baseline during the activation and deactivation periods to quantify the intensity of the baseline at the time of the wavelet peak maxima. The baseline signal will be the mean value of the remaining time points (i.e. the peak maxima were excluded to compute the mean baseline) extracted from the fitting . The peak-to-baseline value for each time series will be calculated by computing the % signal change in comparison to the baseline at each peak position.

9.3 Results

The activated area in the motor cortex can be seen highlighted in red. Those pixels which are hyper-tense corresponds to activation. The area in the non-UEPIS case showed a larger area of activation. In general, the slice with UEPIS was less contaminated due to venous residual responses (Fig. 9.3).

The comparison between the signal changes during activation and rest for the visual and motor cortex can be seen in Figure 9.4 respectively. For each participant the two strongest BOLD voxels were selected and the % change was calculated at activation and rest. In some cases activation was slightly stronger than rest while in others the rest state was higher. A strong linear correlation (1.5845 ± 0.73197) was found within the data ($p < 0.0001$).

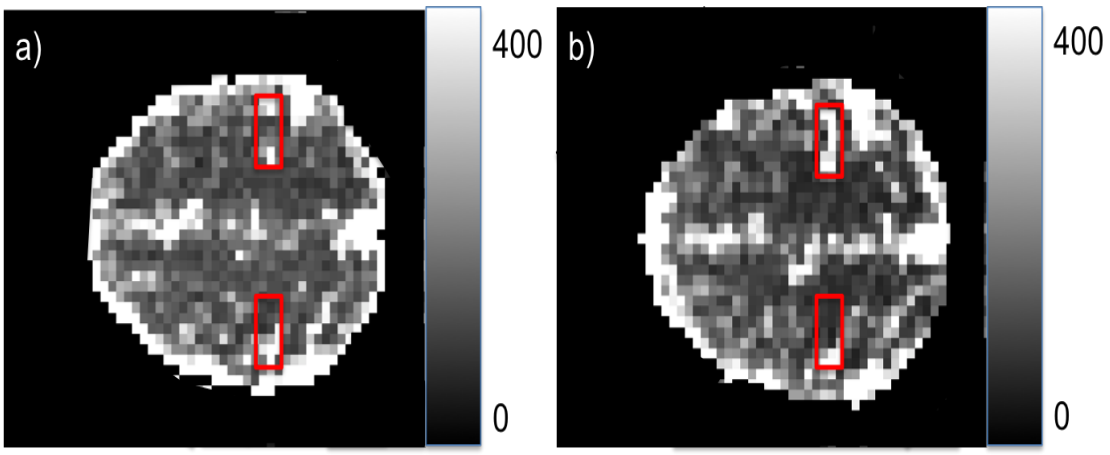

FIGURE 9.3: Example of the activation areas in the motor cortex for the UEPIS (a) and the non-UEPIS sequence (b). Slightly larger area is found in the non-UEPIS.

9.4 Discussion

In this chapter the UEPIS sequence was applied to two pilot fMRI studies. Differences were not found in the intensity of the oscillations during activation and rest. In fact, linear correlation was found between the signal during activation and the signal at rest. Therefore, the increase of one values means the increase of the other value. The most likely explanation for this lack of differences is that in

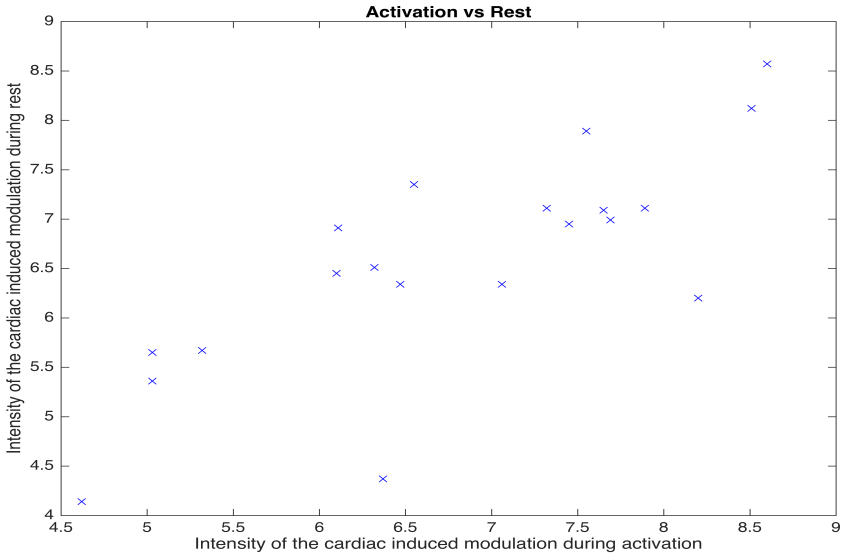

FIGURE 9.4: Relation between the intensity of the peak during activation and the intensity of the peak during rest.

the fMRI studies, the peak is a response to the whole brain dynamics due to the input cardiac pressure wave and it is not sensitive to local changes in the blood flow. In chapter 6, it was shown that peak of the oscillation is not flow related. Otherwise, the intensity of the oscillation should have increased during activation because of the increase of CBF in the activated region [71]. The fact that there are not significant changes between both states correlates with the idea that the oscillation is not flow related.

During activation the amount of deoxygenated hemoglobin decreases within the tissue, reducing the concentration of paramagnetic molecules. This condition reduces the amount of susceptibility dephasing induced and thereby increases the T_2^* for the stimulated tissue relative to the unstimulated tissue [38]. However, in Chapter 6 showed that there are no dependencies between the T_2^* and the intensity of the oscillation.

One of the constraints in this study was once again the single slice acquisition protocol. A real time fMRI protocol was used to obtained the area with the strongest BOLD signal change in order to place the UEPIS imaging slice through it. However, these changes could be related to a higher venous response and not necessarily be related to activation in the tissue. It has already been mentioned that the imaging slice is able to cover only a small part. Therefore, it is also possible that the activated region was missed. In light of these results, future research should focus on acquiring larger areas by, for example, increasing the number of slices, the slice thickness or by moving the imaging slice into different positions. Additionally, the decrease in the size of the activated area can be due to the short TE used. Previous studies have shown that the BOLD response diminishes at TEs shorter than the optimum TE for BOLD [155]. Under the same threshold the area of UEPIS signal activation was smaller than a non-UEPIS. So the change in the baseline due to activation gets already reduced with the UEPIS case. Although it seems that UEPIS is not able to detect the changes in the intensity of the oscillation, it could be useful to remove venous residual responses from the BOLD activation maps.

Chapter 10

Sleeping in the Scanner. A Case Study.

Although a sleeping study was not carried out, one of the participants reported to have fallen asleep during the scan session and woken up at the end of it. An anomalous signal change pattern was obtained and therefore, this data was analysed separately as a case of study.

The participant (27 years old) was scanned with the protocols approved by the Trinity College School of Medicine Research Ethics Committee. He was imaged in a 3.0 T Philips whole-body MRI scanner (Philips, The Netherlands) using a standard single-shot GE EPI sequence. For this participant a variation of the offset frequency was conducted. Therefore, the distance of the REST slabs were varied between 0.8 mm and 50 mm to alter the off-resonance frequency while the voxel size was 3.5 x 3.5 x 3 mm, the TE = 5 ms, TR = 45ms and the FA = 35°. Two REST slabs of 5 mm in thickness were placed parallel to the imaged slice. The first one was located above the imaged slice at a distance equal to 15mm. The second one was placed below separated by 20 mm. MT effects were introduced in both cases by a negative (-13411 ± 2290Hz) and a positive off frequency (17882 ± 2290 Hz) RF pulse. The imaging slice was placed away from the ventricle to

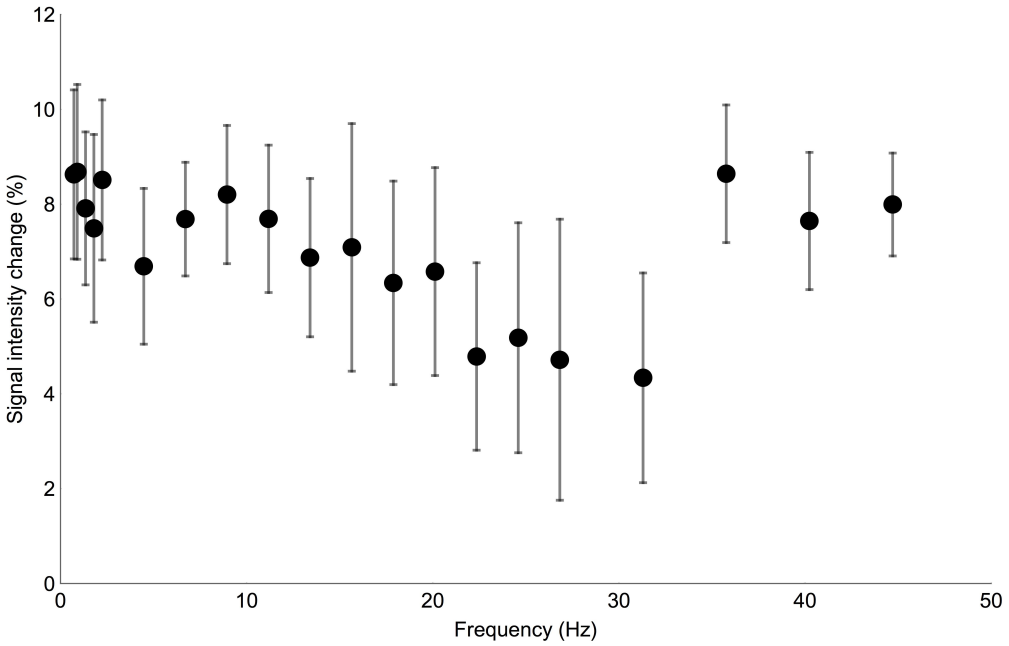

FIGURE 10.1: Signal intensity change when different frequency offset variations where applied. The participant reported to have fallen asleep during the scan session.

avoid pulsation effects (see Figure 4.1b). The offset frequency was calculated using Equation 4.1.

The intensity of the mean maximum peak was calculated by computing the signal change in % between the peak and the baseline. The detection of the maximum peak is based on the method proposed in Gomes and Pereira [141]. The method uses the open function *peakdet* implemented in Matlab, to detect all the local maxima of the temporal signals. The mean baseline signal will be the mean value of the remaining time points (i.e. the peak maxima were excluded to compute the mean baseline).

Figure 10.1 presents the % signal change at each offset frequency. The signal change started to drop after the 8^{th} run and kept decreasing until it went back to normal again in the 17^{th} run. Figure 10.2 illustrates some examples of the time series at different offset frequencies. The first two images represent scan number 3 and scan number 5 with offset frequencies equal to 1.3075 and 4.3625 kHz respectively (Figures 10.2a-b). Clear cardiac behaviour is present in both cases with no signs of decline in the peaks strength. Figures 10.2c-e reveal scans number

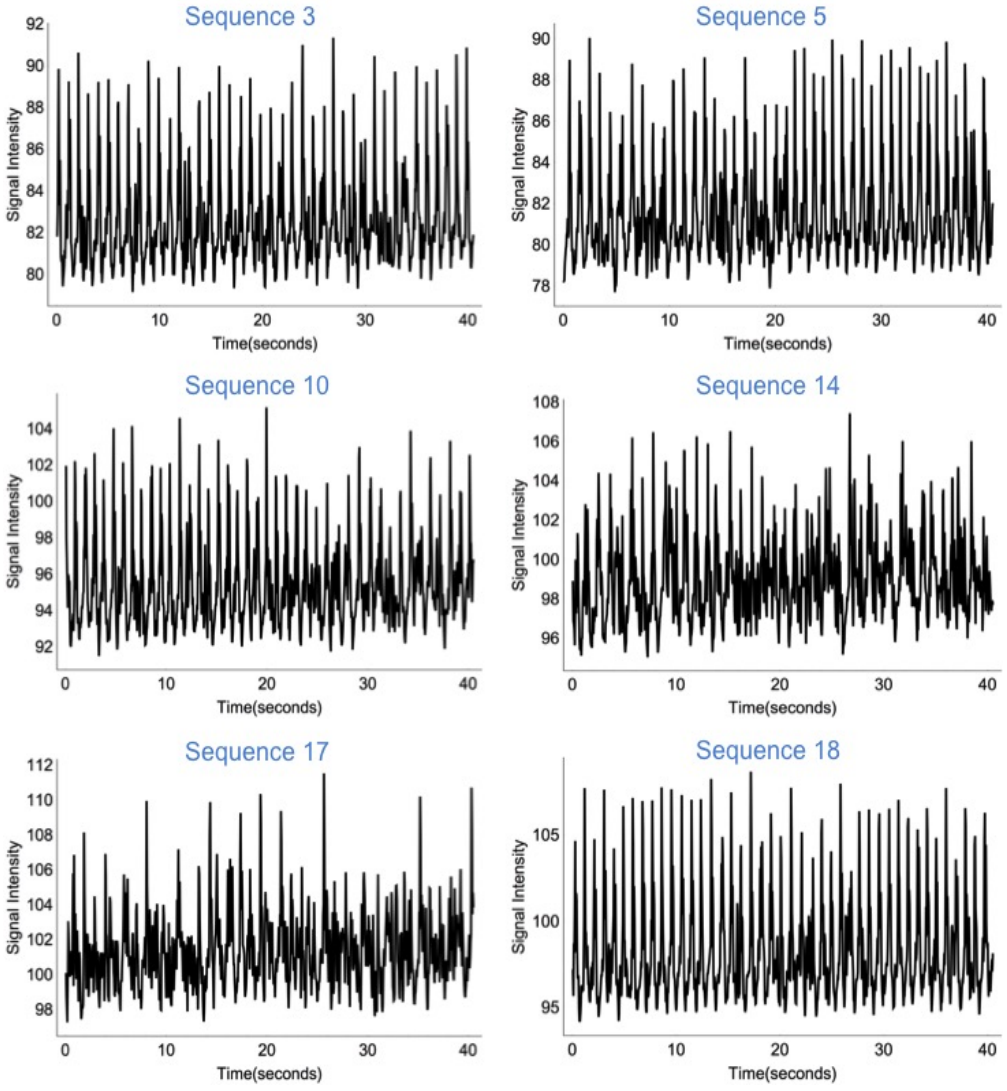

FIGURE 10.2: Example of six time series for the participant that reported falling asleep. Sequences 3, 5 and 10 suggest that the patient is still awake, while the noisy sequences 14 and 17 that the patient is falling asleep or that is already sleeping. Finally, sequence 18 might represent the time when the patient is again awake.

10, 14 and 17 with offset frequencies amounting 13.0825, 21.8150 and 30.5450 kHz. Scan number 10 exhibited a general cardiac behaviour but at the end of the scan the peaks are losing intensity and the baseline is getting noisier. The strongest differences appeared in scans 14 and 17. The peaks are no longer constant and in some cases even disappear, apart from having a much noisier baseline. Finally, the last image shows scan 18 with a frequency offset set to 34.9075 kHz. The cardiac behaviour comes back to normal suggesting that the participant woke up at the end of the scan session. This could represent a variation in the brain wave pattern

(i.e. decrease in the frequency) in combination with a decrease in the cardiac signal due to sleepiness.

Figure 10.1 illustrated the variation of the cardiac induced oscillations in a subject that reported to have fallen asleep during the data acquisition. During the experiment there was an evident decline not only in the intensity of the oscillation maxima but also the cardiac induced oscillations pattern worsened. In those cases, the oscillation maxima are found apparently random and not periodically as it was in previous cases. This results might be threefold. First, during sleep there is a decrease in the arterial pressure [190, 191]. Since the signal arises from the tissue response to the input pressure wave, a decrease in the latter might introduce a decrease in the former. This might explain why the peak profile disappears. Second, it was shown in Chapter 5 that there is little correlation between the cardiac and the wavelet frequency. During sleep, brain waves slow down and the Delta Waves become predominant [144, 145]. Additionally, the heart rate slows down during sleep which might disperse the distance among wavelet packets [192]. Therefore, the response of the tissue might also vary influencing the UEPIS signal. Finally, it should also be taken into account that during sleep there is an increase in the number of involuntary movements [192]. Thus, it could be expected that the signal worsens because of the movement sensitivity aforementioned in Chapter 6. However, only one case reported to have fallen asleep and further research is needed to confirm these results.

Part V

Conclusions

Chapter 11

Conclusion and Future Research

Throughout this thesis a new MRI sequence that relies on cardiac induced oscillation changes has been extensively explored. For example, it has been hypothesised that the cardiac pressure wave acts as a travelling wave that modulates the rhythms present in the brain. This modulation produces a signal in the tissue which is difficult to measure with other methods in the brain in vivo and essential for the understanding of the cerebral blood circulation and auto-regulation. Although the studies were carried out with and without angulation, it points in the direction that the brain rhythms are not the same for all regions in the brain. In this case, the cardiac induced modulations should not be in phase. These results are not conclusive. Therefore, more work has to be devoted to answering this question.

Additionally, the interesting mechanism behind the UEPIS contrast has been evaluated with various different parameters inside the sequence. It has been shown that cardiac induced oscillations are not TE, SL or frequency dependent and that only the FA and TR strongly influenced the signal. It has also been revealed that the characteristic signal in the UEPIS sequence is not related to brain movement, inflow effects, phase shifts or BOLD, rather, it has been identified that the tissue itself as the origin of those signals. Thus, it was suggested the NOE as one of the possible explanations for the contrast mechanism. However, more work is needed

to confirm the veracity of it because the mechanism behind the cardiac induced modulation still remains unclear.

One of the major limitations of this protocol is that the signal acquisition gets limited to a single slice due the short TR. This is a constraint for those studies that require, for instance, the study of larger brain regions. In those cases, manual shifts of the slice up and down would be required to cover the entire region of interest. Thus, an expansion of the current protocol into a multi-slice UEPIS sequence would allow for the examination of larger regions of interest. Although this is not easy to accomplish, current development of new scanners in MRI are moving towards faster acquisition times, giving the possibility, for instance, of acquiring multiple slices in just one excitation. Although this could be valuable to cover larger regions, additional MT effects should be taken into account. When the image gradients switch to excite a new imaging slice it induces a RF pulse. These RF pulses induce MT effects into the adjacent slices (Multi-slice EPI MT effects). Previous studies have tried to account for these MT effects to correct the MRI signal [54], however, the UEPIS signal relies on strong saturation effects combined with MT effects. Therefore, additional MT effect could benefit the intensity of the cardiac induced oscillation. The only consideration to be taken is that the central slice would suffer from higher MT that outer slices and the strength of the peaks may differ between.

Another problems of UEPIS is its sensitivity to movement. Motion correction was not possible with conventional methods due to single slice acquisition. This could be solved by acquiring higher number of slices and using some of the available motion correction tools such Statistical Parametric Maping (SPM) [193]. Also more advanced techniques such head tracking for real-time motion correction in the MRI environment using a single camera could be applied[194].

Additionally, the UEPIS sequence was applied in different pilot studies. First an ageing study was carried out. Alterations of the cardiac related MT changes were observed across participants. These changes were manifold, varying in shape, amplitude and frequency. In particular, older participants possessed a higher number

of frequencies as well as a decrease in the size and number of the cardiac induced oscillations. Spectral clustering was used to successfully classify the spectra of both groups in separate clusters, however some participants still felt into the wrong groups. In spite of that and on the basis of these promising results, work should concentrate on the study of the ageing brain using this sequence. For example, as UEPIS only needs a few minutes, a large database could be achieved. Each time a new dataset is acquired, and with the help of a spectral clustering algorithm, this dataset could be sorted into one of the possible clusters. This would provide information about the brain dynamics of the participant in a few minutes. Continuing study might also involve comparing the results from the spectral clustering with the information from MR elastography about the stiffness of the brain tissue of each participant. Since the stiffness describes the mechanical properties of the tissue, it would help understand the relationship between the UEPIS signal and the brain dynamics, and changes in the ageing brain.

A pilot study was conducted with depressed patients. Alterations in the basal ganglia of MDD patients were observed. These changes, as it happened in the ageing study, were manifold, varying in shape, amplitude and frequency. MDD patients showed more dynamic components in the basal ganglia which potentially related to tissue compartments that have a delayed response to cardiac dynamics. The Fractal analysis displayed an increase in the number of singularities confirming this observation. UEPIS might help to shed light on the dynamic changes in the depressed brain. However, it was shown that the basal ganglia was an region corrupted by movement. Thus, further studies should focus on less movement sensitive areas such as the prefrontal cortex. Additionally, the population in the study was small and further research should focus on acquiring a larger cohort of MDD and control participants with a different number of slices to cover larger regions.

Two fMRI pilot studies were also conducted. No changes were observed in the intensity of cardiac induced oscillations in the motor and visual cortex during rest and activation. A real time fMRI protocol was used to obtained the area with the strongest BOLD signal change in order to place the UEPIS imaging slice through

it. However, these changes could be related to a higher venous response and not necessarily be related to activation in the tissue. It has already been mentioned that the imaging slice is able to cover only a small part. Therefore, it is also possible that the activated region was missed. In light of these results, future research should focus on acquiring larger areas by, for example, increasing the number of slices, the slice thickness or by moving the imaging slice into different positions.

Of particular interest was the participant that reported to have fallen asleep during the data acquisition. The participant suffered a decline in the intensity of the cardiac induced oscillations. During sleep brain waves slow down and the Delta Waves become predominant, [145] and the heart rate slows down during sleep which might disperse the distance among wavelet packets [192]. However, only one case reported to have fallen asleep and further research is needed to confirm these results. The next stage of the research should focus on confirming these results by acquiring new data during sleep. Clearly, the achievement of this experiment might not be trivial. Some participants feel anxious inside the scanner which combined with the loud noise of the scanner might impede falling asleep. However, spite of these difficulties the findings suggest that UEPIS could add more information about brain dynamics during sleep.

Since UEPIS is a completely new sequence, a whole spectrum of new applications opens. For instance, patients that have suffered a stroke or have a tumour, have their brain dynamics altered. UEPIS might help to highlight the affected region in just a few minutes by quantifying those regions without cardiac induced oscillations.

Finally, it could also help differentiate between genders among the young cohort. Although it was not studied, stronger peaks were normally detected in male subjects in comparison to females. Clearly, further research is needed to validate what the origin of these differences is. On one hand, it would be compelling to study the differences between participants exercising regularly and those that do not exercise. On the other hand, it would be interesting to search in the female group

for brain dynamic' changes in relation to contraceptives intake or different stages during the menstrual cycle.

To conclude, the effectiveness of UEPIS as a powerful and useful new sequence has been established. Numerous studies have been employed to highlight the advantages and potential uses for the sequence. This research has also identified and outlined potential limitations that require future investigation.

Part VI

Appendix

Appendix A

AppendixA

In this Appendix, complementary examples to Chapter 5 are presented.

A.1 Examples of Timing Without Angulation of the Imaging Slice

Figure A.1 shows the comparison between the time series a pixel located at the front, one at the middle of the non-angulated imaging slice. Four more participants are shown.

A.2 Examples of Timing With Angulation of the Imaging Slice

Figure A.2 illustrates the comparison between the time series a pixel located at the front, one at the middle of the angulates imaging slice. Four more participants are shown.

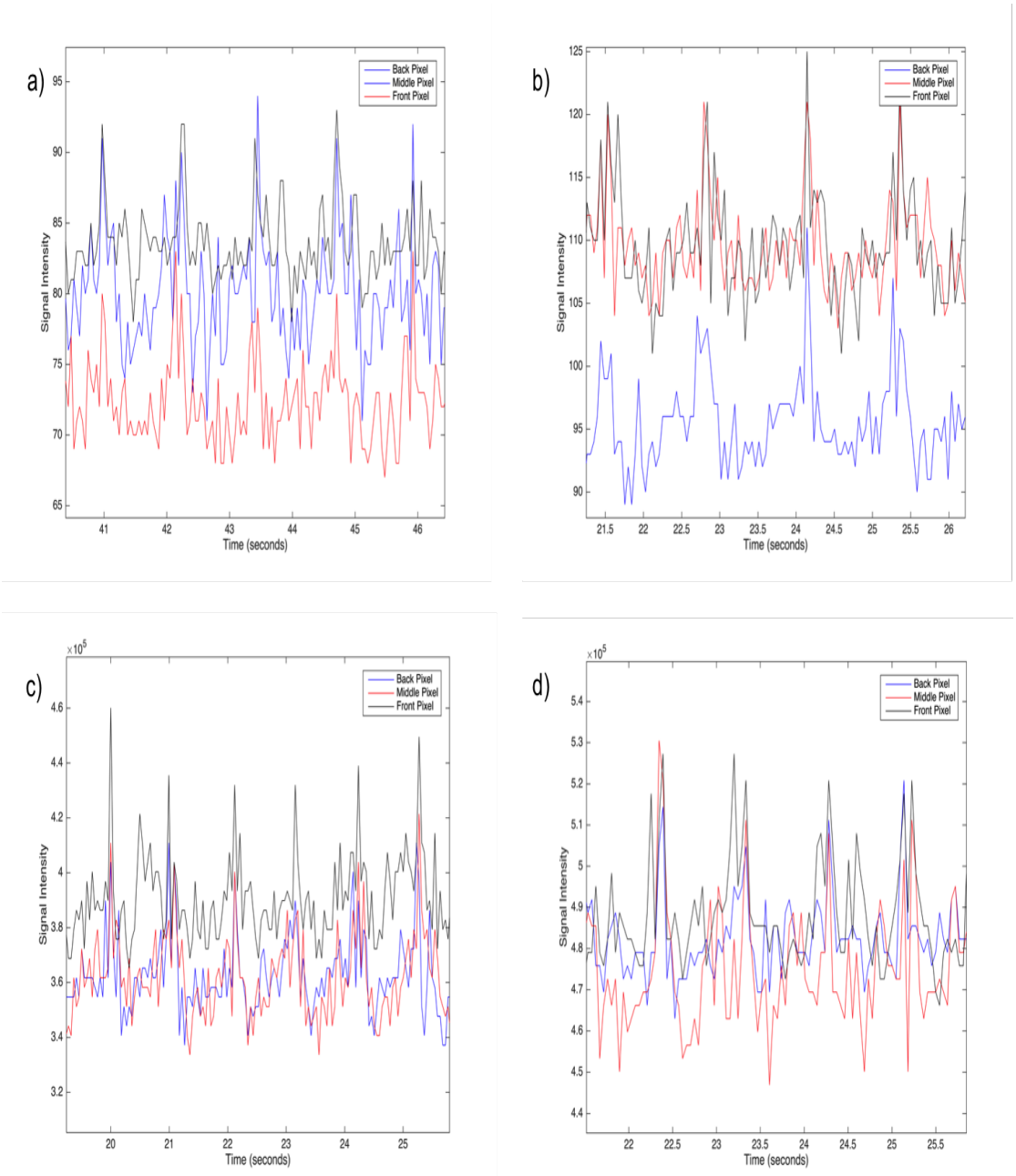

FIGURE A.1: Comparison of the signal of three pixels located at different areas in an horizontal imaging slice. One pixel was located at the front, the second at the middle and the last one at the back of the slice. Four different participants are shown.

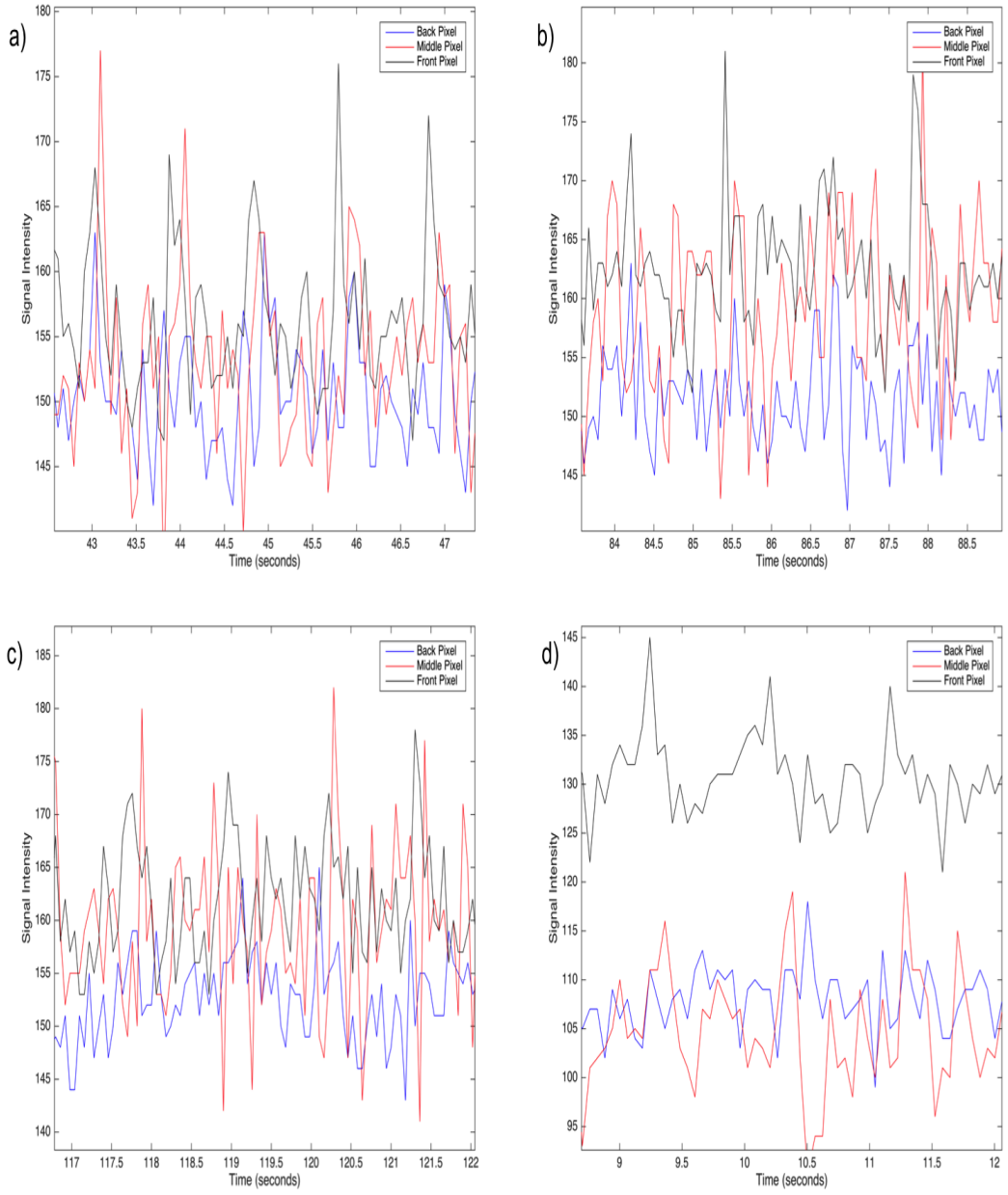

FIGURE A.2: Comparison of the signal of three pixels located at different areas in an angulated imaging slice. One pixel was located at the front, the second at the middle and the last one at the back of the slice. Four different participants are shown.

Appendix B

Individual Signal Parameters Values

In the following sections, the individual values for each subject will be presented for each signal parameter.

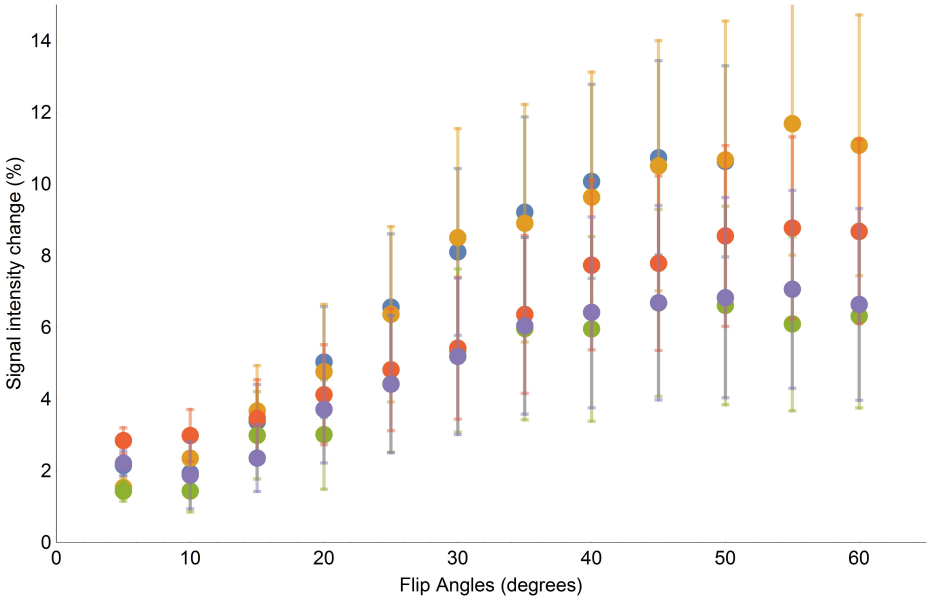

FIGURE B.1: Individual signal changes values in % when the TR = 45ms and the FA was varied between 5 and 60 degrees.

B.1 Flip Angle

5 subjects were scanned to assess the effect of the FA with TR = 45 ms (Fig. B.1) and TR = 60 ms (Fig. B.2). Both graphs are practically similar indicating that all subjects, with higher or lower signal change, followed the same behavior in comparison to the average values. Stronger values were observed at shorter TR due to the increase in MT effects which intensified the signal change.

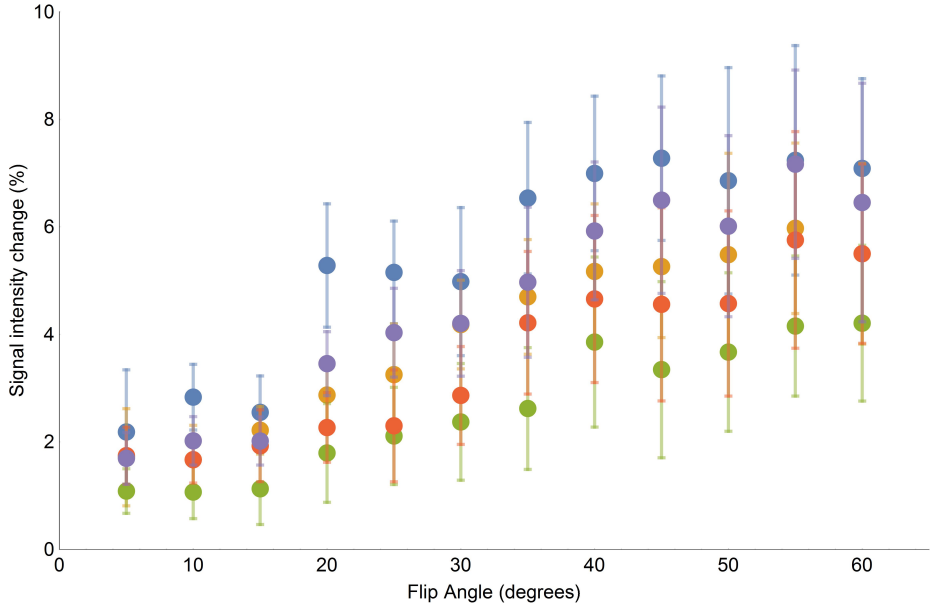

FIGURE B.2: Individual signal changes values in % when the TR = 60 ms and the FA was varied between 5 and 60 degrees.

B.2 Repetition Time

5 subjects were scanned to determine the effect of TR variations with (Fig. B.3) and without the slabs (Fig. B.4). In both cases strong decreases were observed across all subjects. Again, strong variability was present among the different subjects but the tendency was to decline with longer TR.

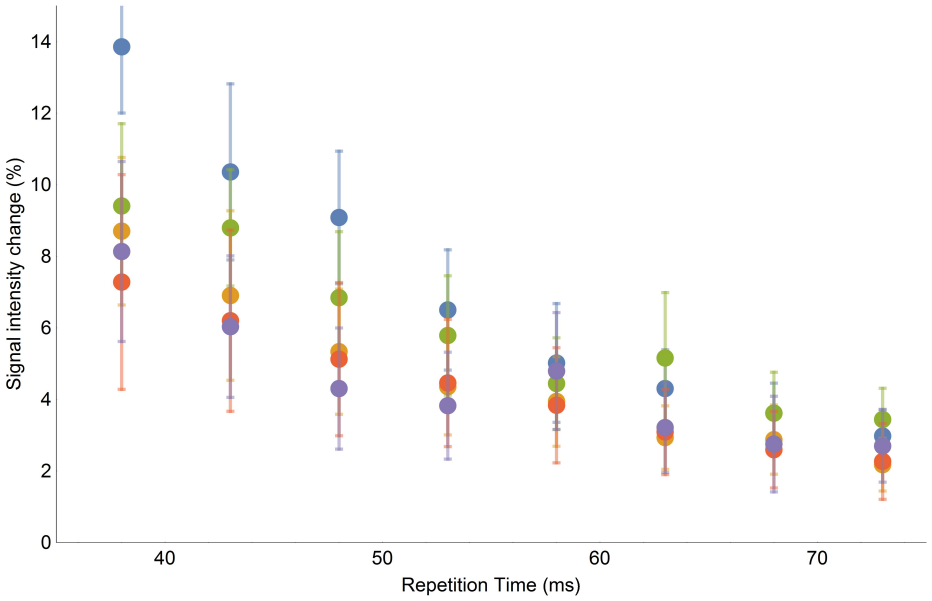

FIGURE B.3: Individual signal changes values in % with TR variations between 38 and 73 ms in the UEPIS.

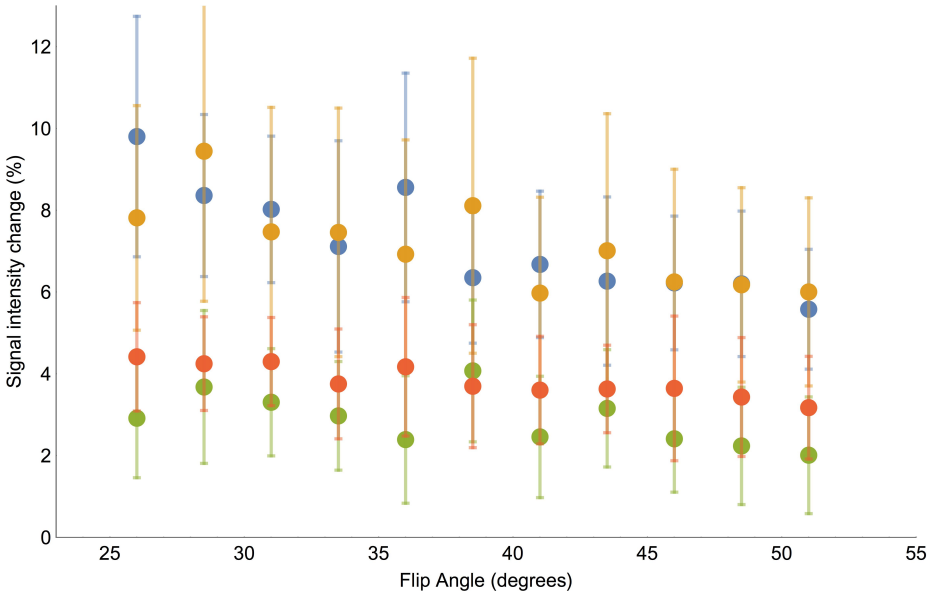

FIGURE B.4: Individual signal changes values in % with TR variations between 26 and 51 ms in the non-UEPIS.

B.3 Slice Thickness

5 subjects were scanned to determine the effect of SL variations (Fig. B.5). All subjects had a constant intensity change across all the slice thickness suggesting no slice thickness dependency.

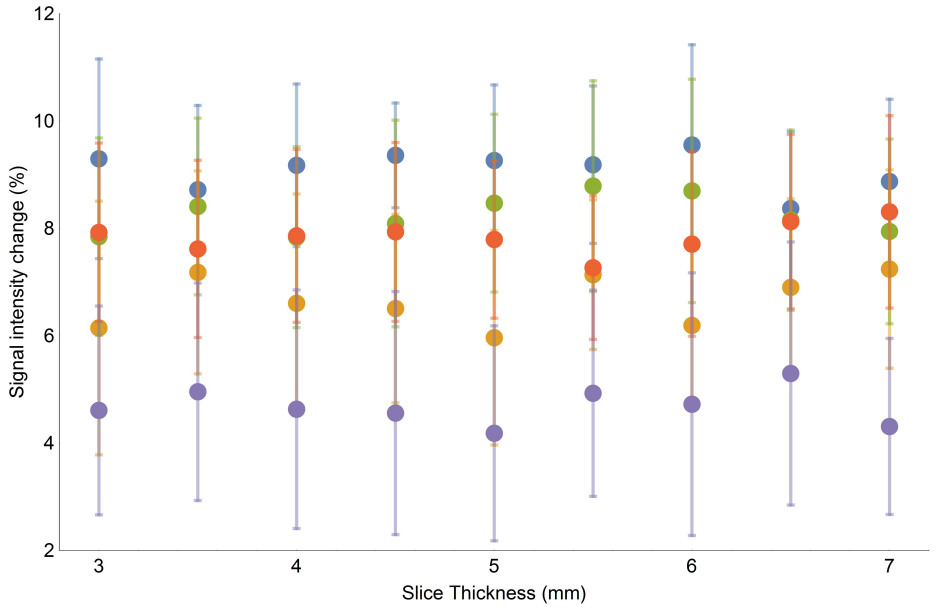

FIGURE B.5: Individual signal changes values in % when the slice thickness was varied between 3 and 7 mm.

B.4 Echo Time

5 subjects were scanned to determine the effect of TE (Fig. B.6). All subjects had a constant intensity change across all the echo times suggesting no echo time dependency.

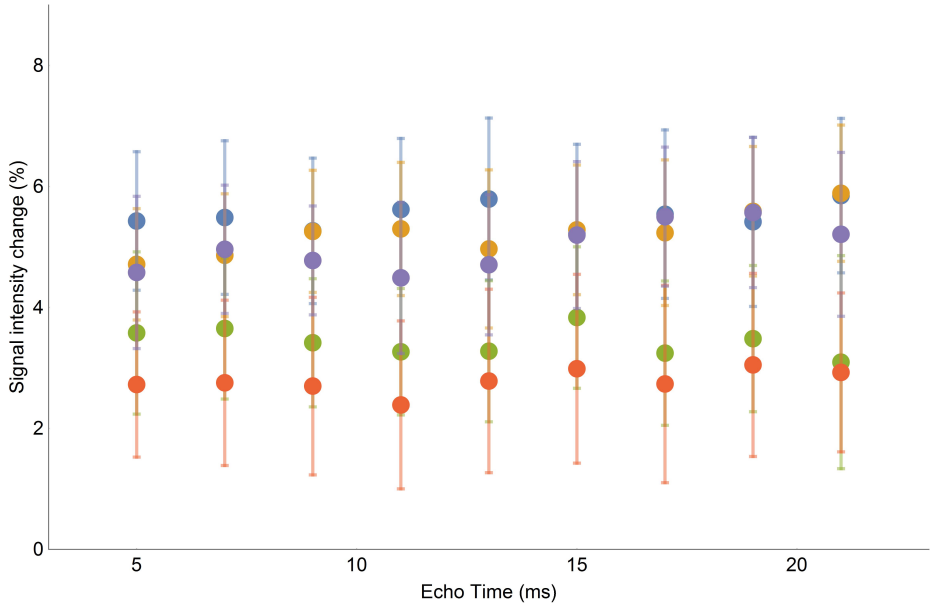

FIGURE B.6: Individual signal changes values in % when the echo time was varied between 5 and 21 ms.

B.5 Frequency Variation

5 subjects were scanned to determine the effect of frequency offset (Fig. B.7). All subjects had a constant intensity change across all the frequencies suggesting no frequency dependency.

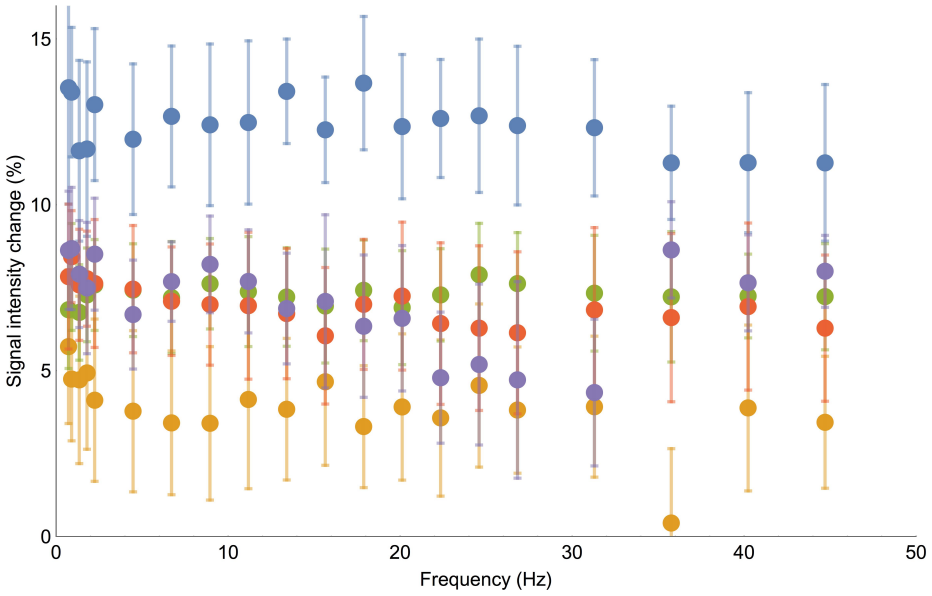

FIGURE B.7: Individual signal changes values in % when the frequency offset was varied between 0.6975 and 43.6350 kHz.

Appendix C

UEPIS Toolbox

Throughout the process of this thesis, a Matlab toolbox has been programmed to analyse the UEPIS signal. The main interface is shown in the next picture.

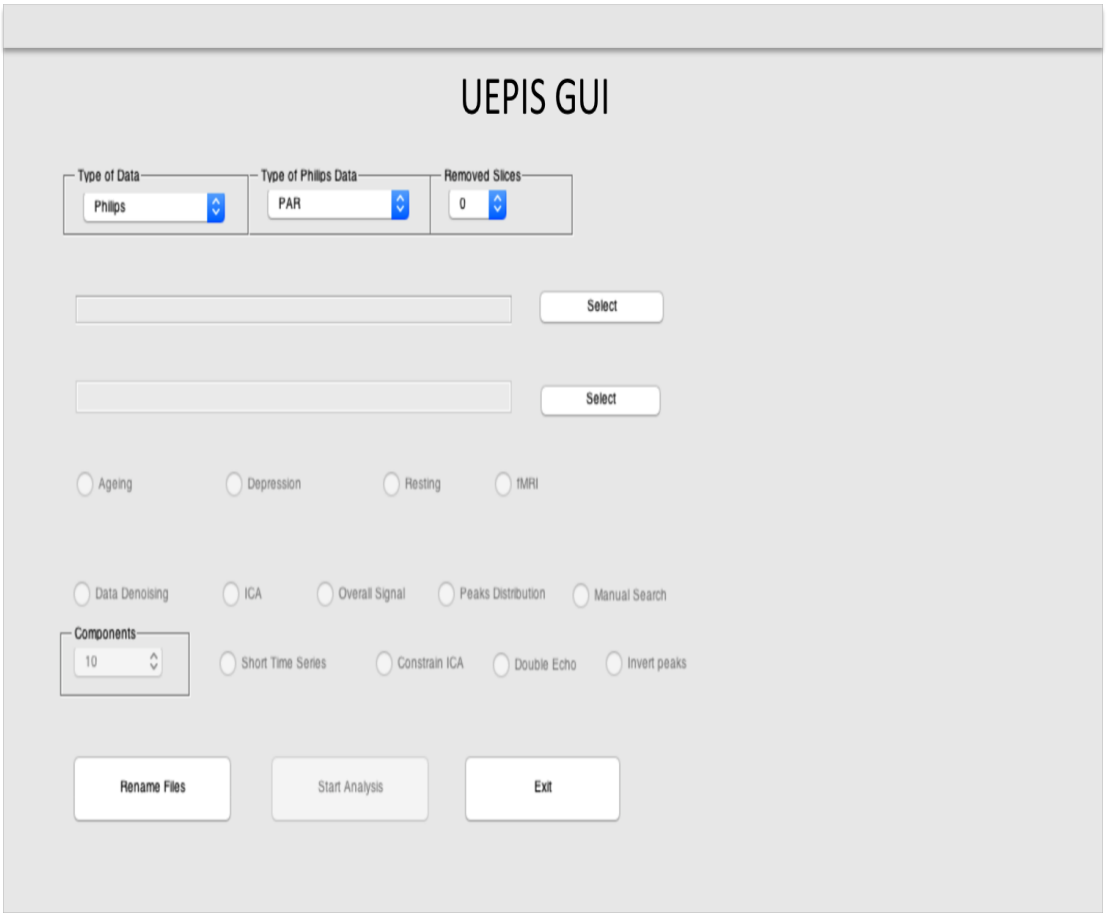

FIGURE C.1: UEPIS User interface.

The top of the window includes the parameters needed to define the data to be analysed:

1. *Type of Data*: It defines if the scanner used to acquired the data is Bruker or Philips.

2. *Type of Philips Data*: If the scanner is Philips, then the format of the data is needed to load the data. There are four possibilities: Nifti format, *PAR* which represents PAR/REC format, *Dicom* which reflects the dicom format in individual files and *New Dicom* which stands for dicom format in just one file.

3. *Removed Slices*: It allows to remove up to 100 repetitions to avoid saturation effects in the data.

Once these values have been set, the filename has to be selected. If the filename textfield is empty, the toolbox will show and error. The software allows to select multiple files for the analysis as long as they have the same format and longitude.

The second text field refers to a mask file. If the user selects a mask, all the voxels of that mask will be processed, otherwise a magnitude mask of the whole slice will be estimated. This is done to reduce the number of voxels to processed and save some computational time.

The next step is to select if we are dealing with Resting State (*Resting*) or *fMRI* data. The *Ageing* and *Depression* are there for future development of the software. At least one of these options has to be selected, otherwise the application will return an error.

Once the previous fields have been set, the following analysis can be carried out:

1. *ICA*: This is needed to carry out the ICA analysis. Two options are available for this option.

   (a) *Number of Components*: This establishes which is the maximum number of possible sources. The values are 10, 20, 30, 40 or the same as

pixels inside the slice. The last value requires a huge computational load.

(b) *Constraint ICA*: The number of components is set to 5 for all cases independently of the optimum values calculated.

2. *Overall Signal*: The signal is average across all the voxels inside the slice.

3. *Peak Distribution*: Each voxel is analysed individually and the peak statistics are calculated.

4. *Manual Search*: It allows a new window to be opened where manual search can be done at each voxel, to move across all the voxels in the slice.

This options are independent and combining both options will return an error. There are a few extra options available that can be also used:

1. *Data Denoising*: The data is denoised using a wavelet transform prior to any analysis.

2. *Short Time Series*: this checkbox sets the maximum number of repetitions to 1000.

3. *Double Echo*: For double echo data, the signal is separated into alternative datasets and analyse individually.

4. *Invert peaks*: The signal is inverted to analyse the appearance of down peaks in the signal.

5. *Rename Files*: This button has been added to rename files, in case it is needed to enable multiple files selection which might have the same name.

A future version will optimise the code and combine the spectral clustering as well as the fractal analysis into the main interface.

C.1 ICA Results Window

When the ICA analysis is computed successfully, a new window appears with the results. An example can be seen in Figure C.2.

On the top two images are shown. The first one corresponds to the time series of the first component and the second one to its spectrum. Below the images, there are two text fields. The first one contains information about the displayed component such the eigenvalue of the mixing matrix for that component and the maximum frequency value of the spectrum. The second one would show the parameters of the time series to which the component belongs to when the *Show Parameters* button is clicked.

It is possible to go through all the components of a time series by clicking the *Next Component* and *Previous Component* buttons. By clicking *Next Component*, the

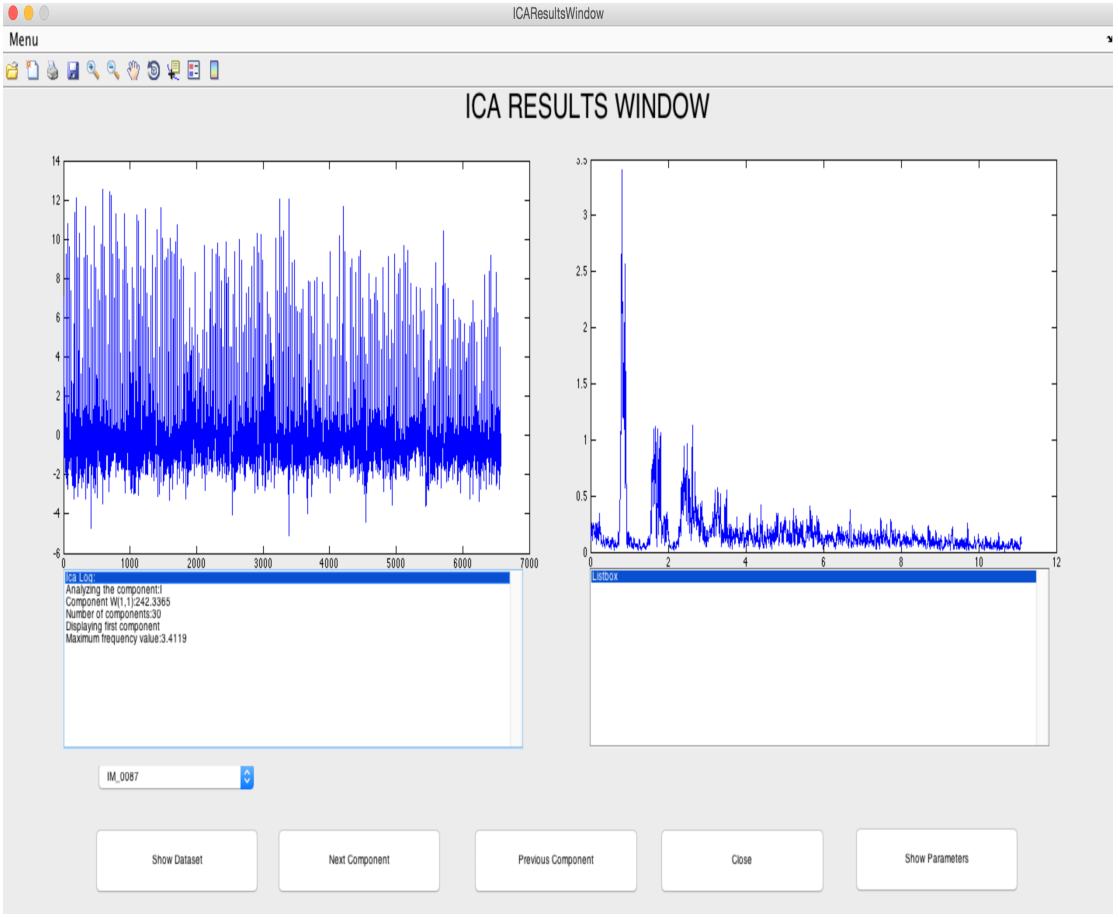

FIGURE C.2: Example of the ICA results window.

time series and spectrum of the next component will be shown, as well as the text field will be updated with the information of the component. By clicking *Previous Component* it is possible to go back to previous components. Once the first or last component has been reached, a message will be shown in the text field.

It is possible to have the components from other datasets when multiple file or double echo analysis have been selected. In order to do this, it is necessary to select from the pop-up menu the dataset and afterwards press the button *Show Dataset*. The new ICA results will be loaded and the same treatment as above can be done.

C.2 Overall Results Window

When the overall signal analysis is computed successfully, a new window appears with the results. An example can be seen in Figure C.3.

On top two images are shown. The first one corresponds to the time series of the first component and the second one to its spectrum. The first one contains information about the overall signal such as the maximum frequency in the spectrum, mean and standard deviation of the baseline of the time series. The second one would show the peaks statistics, (mean and standard deviation) of the overall signal if the *Peak Statistics* button is clicked.

For multiple file or double echo analysis the *Next Parameters* and *Previous Parameters* buttons will show the next or previous overall signal if the last or the first signal has not been reached. This will update the time series course as well as the spectra and the information about the overall signal.

The evolution of the peak across all the datasets can be shown when pressing the *Show Evolution* button. This will show a new figure with the evolution of the mean and standard deviation of the baselines and the evolution of the mean and standard deviation of the peak strength.

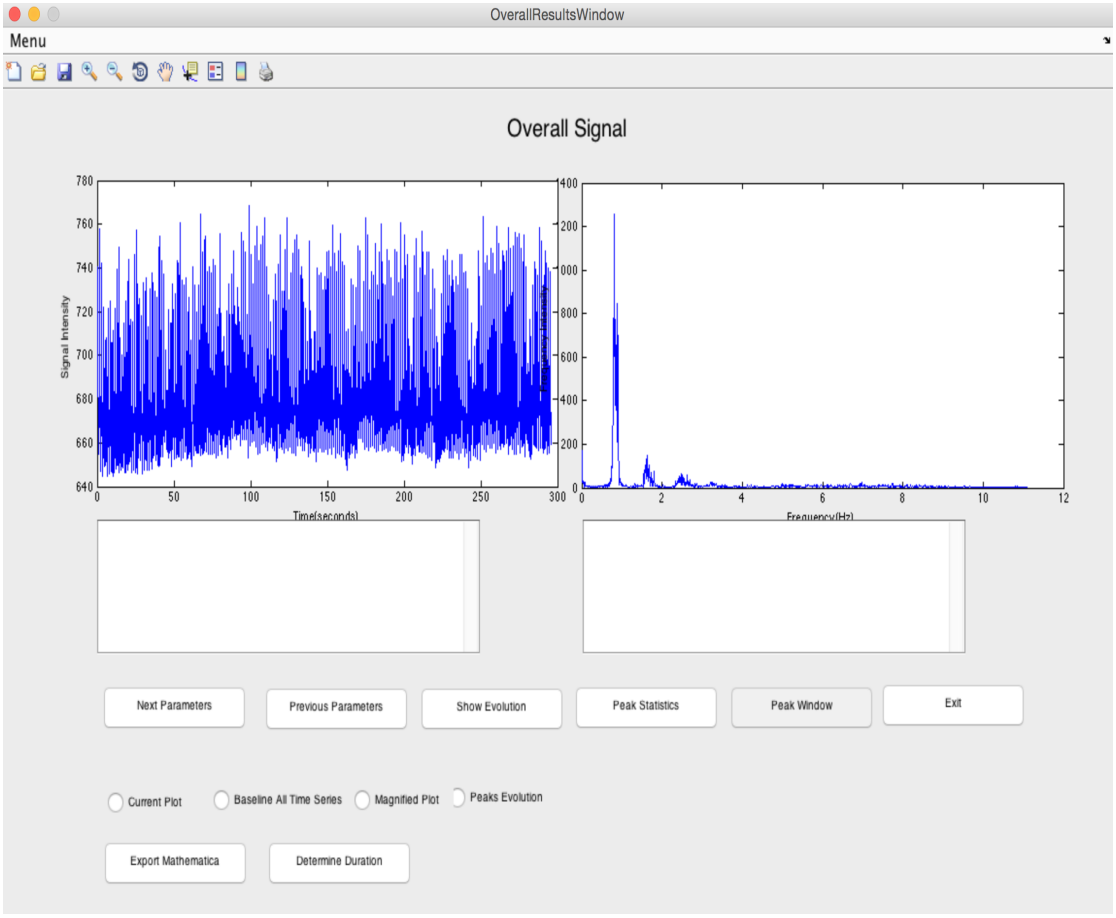

FIGURE C.3: Example of the overall signal analysis window.

It is possible to estimate the duration of the peak by pressing the *Determine Duration* button. It will fit each peak to a Gaussian function and will average the values to obtain the mean peak duration as well as its standard deviation.

The data from the time series can be exported to Mathematica by pressing the *Export Mathematica* button. Four options are available:

1. *Current Plot*: It creates a Mathematica file which the data obtained from the current time series plot.

2. *Baseline All Time Series*: It creates a Mathematica file which the data obtained from the all the time series.

3. *Magnified Plot*: It creates a Mathematica file which the data obtained from the current magnified time series plot.

4. *Peaks Evolution*: It created a Mathematica file the baseline and peak strength evolutions.

Finally, the button *Peak Window* connects the Overall Signal Window with the Peaks Results Window which will be described next.

C.3 Peak Distribution Window

The peak analysis window will show a map with the mean peak as each pixel and the same for the frequency intensity of the cardiac signal. An example can be seen in Figure C.4.

Below both images there will be two text fields. The first one, would include the mean and standard deviation of the peaks intensity. The second one would show the mean and standard deviation of the cardiac frequency.

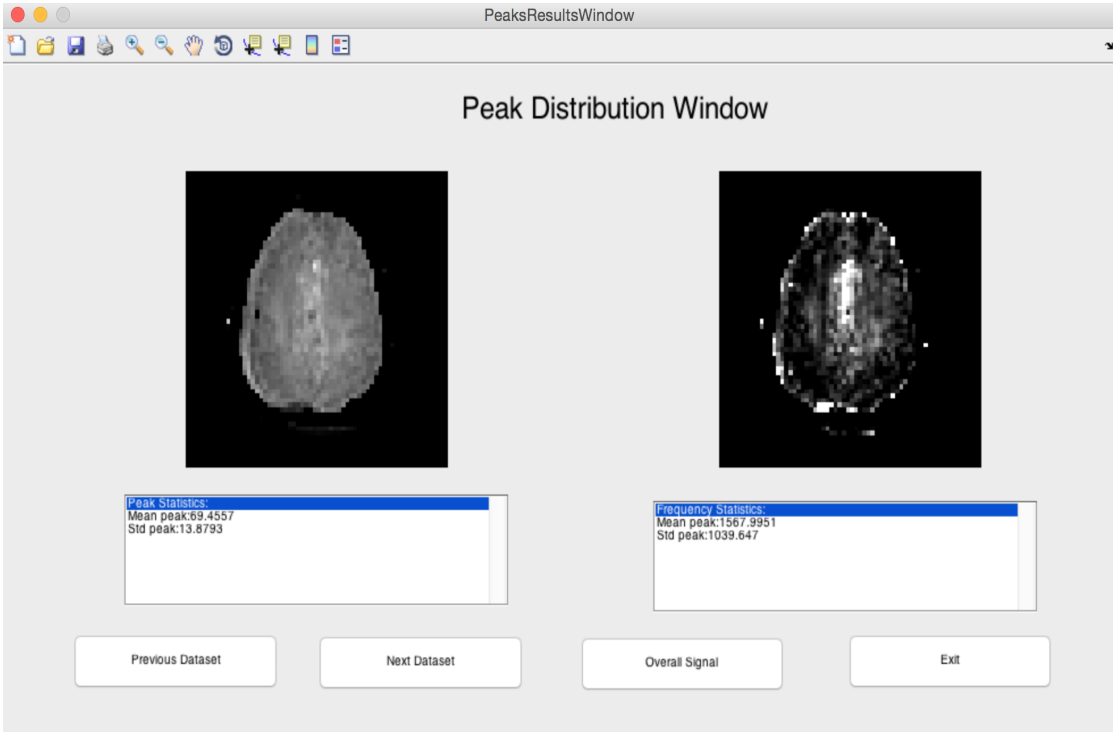

FIGURE C.4: Example of a Peak Distribution Window.

In the same fashion as the previous windows, if there is more than one dataset it will possible to change between datasets by pressing the buttons *Previous Dataset* and *Next Dataset*.

Finally, the window is linked to Overall results window by the *Overall Signal* button. It will compute the overall signal for each dataset and show the aforementioned Overall Results Window.

C.4 Manual Search Window

The manual search window allows to plot the individual time series of a pixel by clicking over an image. The image is computed by averaging over all the repetitions of the dataset. Once a pixel is clicked, the time series linked to it is presented in the plot next to the image. An example can be seen in Figure C.5.

If some pixels are of the interest of the user, it is possible to add those pixels together by clicking the *Add Pixel* button. After that, there are three possibilities:

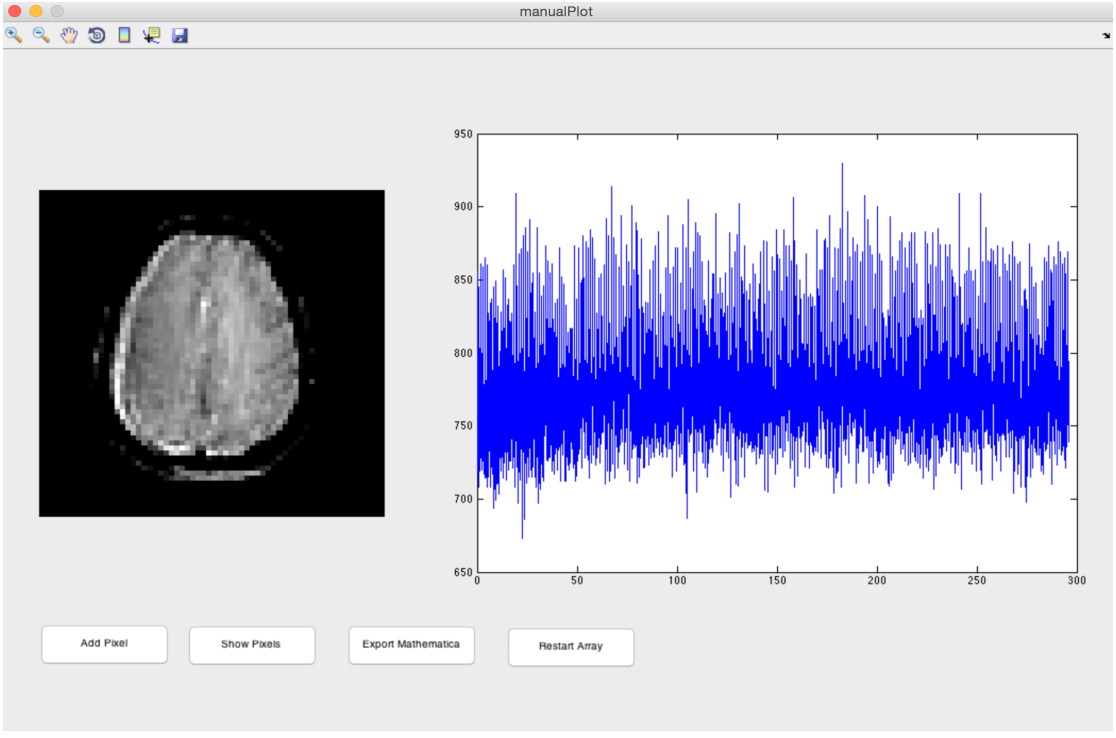

FIGURE C.5: Example of a manual search window.

1. *Show Pixels*: It will show the selected pixels over the image to see the location.

2. *Export Mathematica*: The times series of each pixel as well as the average value of all of them will be saved into a mathematica file.

3. *Restart Array*: All the saved pixels values are deleted from the memory.

Bibliography

[1] Denk, W., Strickler, J. H. and Webb, W. W. Two-photon laser scanning fluorescence microscopy. *Science*, 248:73–76, 1990.

[2] Helmchen, F. and Kleinfeld, D. *In Vivo Measurements of Blood Flow and Glial Cell Function with Two-Photon Laser-Scanning Microscopy. In David Cheresh: Methods in Enzymology, Angiogenesis: In Vivo Systems, Part A.* New York: ACADEMIC PRESS, 2008.

[3] Jöbsis, F. F. Noninvasive, infrared monitoring of cerebral and myocardial oxygen sufficiency and circulatory parameters. *Science*, 198:1264–1267, 1977.

[4] Ferrari, M. and Quaresima, V. A brief review on the history of human functional near-infrared spectroscopy (fNIRS) developed and fields of application. *NeuroImage*, 63(2):921–935, 2012.

[5] Brazy, J.E., Lewis, D. V., Mitnick, M. H, and Jöbsis, F F. Noninvasive monitoring of cerebral oxygenation in preterm infants: preliminary observations. *Pediatrics*, 75:217–225, 1985.

[6] Haacke, E. M., Mittal, S., Wu, Z., Neelavalli, J. and Cheng, Y. C. N. Susceptibility-weighted imaging: technical aspects and clinical applications, part 1. *J. Neuroradiol.*, 30(1):19–30, 209.

[7] Detre, J. A., Leigh, J. S., Williams, D. S. and Koretsky, A. P. Perfusion imaging. *Magn. Reson. Med.*, 23:37–45, 1992.

[8] Aaslid, R., Markwalder, T. M. and Frayne, R. Noninvasive transcranial Doppler ultrasound recording of flow velocity in basal cerebral arteries. *NMR in Biomedicine.*, 57(6).

[9] MacDonald, M. E. and Nornes, H. Cerebrovascular MRI: a review of state-of-the-art approaches. *J. Neurosurg.*, 28:767–791, 2015.

[10] Lassen, N. A. Cerebral blood flow and oxygen consumption in man. *Phsiol. Rev.*, 39:183–238, 1959.

[11] Aaslid, R., Lindegaard, K. F., Sorteberg, W. and Nornes, H. Cerebral autoregulation dynamics in humans. *Stroke*, 20:45–52, 1989.

[12] Tiecks, F. P., Lam, A. M., Aaslid, R. and Newell, D. W. Comparison of static and dynamic cerebral autoregulation measurements. *Stroke*, 26:1014–1019, 1995.

[13] Ainslie, P. N. and Brassard, P. Why is the neural control of cerebral autoregulation so controversial? *F1000Prime Rep*, 6(14), 2014.

[14] Lang, E. W., Mudaliar, Y., Lagopuolos, J., Dorsch, N., Yam, A., Griffith, J. and Mulvey, J. A review of cerebral autoregulation: Assessment and Measurements. *Australiasian Anaesthesia*, pages 161–173, 2005.

[15] Koehler, R. C., Gebremedhin, D. and Harder, D. R. Tole of astrocytes in cerebrovascular regulation. *J. Appl. Physiol.*, 100(1):307–317, 2006.

[16] Peterson, E. C., Wang, Z. and Britz, G. Regulation of cerebral blood flow. *Internation Journal of Vascular Medicine*, 2011(Article ID 823525):8 pages, 2011.

[17] Atwell, D., Buchan, A. M., Charpak, S., Lauritzen, M., MacVicar, B. A. and Newman, E. A. Glial and neuronal control of cerebral blood flow. *Nature*, 468(7321):232–243, 2010.

[18] Tzeng, Y. C. and Ainslie, P. N. Blood pressure regulation IX: cerebral autoregulation under blood pressure challenges. *Eur. J. Appl. Physiol.*, 114:545–559, 2014.

[19] Thompson, R. and McVeigh, E. R. Fast Measurement of Intracardiac Pressure Differences With 2D Breath-Hold Phase-Contrast MRI. *Magn. Reson. Med.*, 49(6):1056–1066, 2003.

[20] Yang, G. Z., Burger, P., Kilner, P.J., Karwatowski, S. P. and Firmin D. N. Dynamic range extension of cine velocity measurements using motion registered spatiotemporal phase unwrapping. *J. Magn. Reson. Imaging*, 6:495–502, 1996.

[21] Wagshul, M. E., Eide, P. K. and Madsen, J. R. The pulsating brain: A review of experimental and clinical studies of intracranial pulsatility. Fluids and Barriers of the CNS. *C3S2E '13 Proceedings of the International C* Conference on Computer Science and Software Engineering*, 8:5, 2011.

[22] Raboel, P. H., Bartek Jr, J., Andresen, M., Bellander, B. M. and Rommer, B. Intracranial Pressure Monitoring: Invasive versus Non-Invasive MethodsA Review. *Critical Care Research and Practice*, 36:520–526, 1996.

[23] Smith, M. Monitoring intracranial pressure in traumatic brain injury. *Anesthesia and Analgesia*, 106(1):240–248, 2008.

[24] Poca, M. A., Sahuquillo, J., Topczewski, T., Pearrubia, M. J. and Muns, A. Is intracranial pressure monitoring in the epidural space reliable? Fact and fiction. *Journal of Neurosurgery*, 106(4):548–556, 2007.

[25] Gelabert-Gonzlez, M., Ginesta-Galan, V., Sernamito-Garcia, R., Allut, A. G., Bandin-Dieguez, J. and Rumbo, R. M. The Camino intracranial pressure device in clinical practice. Assessment in a 1000 cases. *Acta Neurochirurgica*, 148(4):435–441, 2006.

[26] Voulgaris, S. G., Partheni, M., Kaliora, H., Haftouras, N., Pessach, I. S. and Polyzoidis, K. S. Early cerebral monitoring using the transcranial Doppler pulsatility index in patients with severe brain trauma. *Medical Science Monitor*, 11(2):49–52, 2005.

[27] Bellner, J., Romner, B., Reinstrup, P., Kristiansson, K. A., Ryding, E. and Brandt, L. Transcranial Doppler sonography pulsatility index (PI) reflects intracranial pressure (ICP). *Surgical Neurology*, 62(1):45–51, 2004.

[28] Geeraerts, T., Launey, Y., Martin, L. et al. Ultrasonography of the optic nerve sheath may be useful for detecting raised intracranial pressure after severe brain injury. *Intensive Care Medicine*, 33(10):1704–1711, 2007.

[29] Soldatos, T., Karakitsos, D., Chatzimichail, M., Papathanasiou, M., Gouliamos, A. and Karabinis, A. Optic nerve sonography in the diagnostic evaluation of adult brain injury. 12(3):article R67, 2008.

[30] Miller, M. T., Pasquale, M., Kurek, S. et al. Initial head computed tomographic scan characteristics have a linear relationship with initial intracranial pressure after trauma. *The Journal of Trauma*, 56(5):967–973, 2007.

[31] Alperin, N. J., Lee, S. H., Loth, F., Raksin, P. B. and Lichtor, T. MR-intracranial pressure (ICP): a method to measure intracranial elastance and pressure noninvasively by means of MR imaging: baboon and human study. *Radiology*, 217(3):877–885, 2000.

[32] Weishaupt, D., Kchli, V. D. and Marincek, B. *How does MRI work?.* Springer, Berlin, 2006.

[33] Brown, M. A. and Semelka, R. C. *MRI basics principles and applications.* Wiley-Liss, 2003.

[34] Slichter, C. P. *Principles of Magnetic Resonance.* 3nd edn, Springer, Berlin, 1992.

[35] Bloch, F. Nuclear induction. *Phys. Rev.*, 70:460–474, 1946.

[36] Berry, E. and Bulpitt, A. *Fundamentals of MRI: An Iteractive Learning Approach.* CRC Press, 2000.

[37] Elster, A. D. Questions and Answers in MRI. http://mri-q.com/index.html, 2014. Accessed: 2015-07-28.

[38] McRobbie, D. W., Moore, E. A., Graves, M. J. and Prince, M. R. *MRI From Picture to Proton.* Cambridge University Press, 2nd edition, 2007.

[39] Kerskens, C. M., Piech, R. M. and Meaney, J. F. M. *Imaging Blood Circulation Using Nuclear Magnetic Resonance, in Microcirculation Imaging (ed M. J. Leahy).* Wiley-VCH Verlag GmbH & Co. KGaA, Weinheim, Germany., 2012.

[40] Zimmerman, J. R. and Brittin, W. E. Nuclear magnetic resonance studies in multiple phase systems: lifetime of a water molecule in an adsorbing phase on silica gel. *J. Phys. Chem.*, 61:1328–1333, 1957.

[41] Chavhan, G. B., Babyn, P. S, Thomas, B., Shroff, M. M. and Haacke, E. M. Principles, Techniques, and Applications of T_2^*-based MR Imaging and Its Special Applications. *NeuroImage*, 29(5):1433–1449, 2009.

[42] Currie, S., Hoggard, N., Craven, I. J., Hadjivassiliou, M. and Wilkinson, I. D. Understanding MRI: Basic MR Physics for Physicians. *Postgrad. Med. J.*, 89(1050):209–223, 2013.

[43] Ernst, R. R. and Anderson, W. A. Application of Fourier Transform Spectroscopy to Magnetic Resonance. *Review of Scientific Instruments*, 37(1):93–102, 1966.

[44] Wolff, S. D. and Balaban, R. S. Magnetization Transfer Contrast (MTC) and tissue Water Relaxation In Vivo. *Magn. Reson. Med.*, 17:304–314, 1989.

[45] Edelmann, R. R., Ahn, S. S. and Chien, D. Improved time-of-flight MR angiography of brain with magnetization transfer contrast. *Radiology*, 184:395–399, 1992.

[46] Dousset, F., Franconi, J. M. and Degreze, P. Use of Magnetization Transfer Contrast to improve Cerebral 3D MR Angiography. *Neuroradiol.*, 36:188, 1994.

[47] Pierce, W. B., Harms, S. E., Flamig, D. P., Griffey, R. H., Evans, W. P. and Hagans, J. E. Three-dimensional gadolinium-enhanced MR imaging of the breast: pulse sequence with fat suppression and magnetization transfer contrast. Work in progress. *Neuroradiol.*, 181:757–763, 1991.

[48] Dean, K. I., Komu, M., Dean, P. B. and Kormano, M. Magnetization transfer contrast in gadopentetate-dimeglumine-enhanced breast magnetic resonance imaging at 0.1 Tesla. *Invest. Radiol.*, 29(2):302–303, 1992.

[49] Dousset, V., Grossman, R. I., Ramer, K. N., Schnall, M. D., Young, L. H., Gonzalez-Scarano, F., Lavi, E. and Cohen, J. A. Experimental allergic encephalomyelitis and multiple sclerosis: lesion characterisation with magnetization transfer imaging. *Radiology*, 182:483–491, 1992.

[50] Grossman, R., Gomori, J. M., Ramer, K. N., Lexa, F. J. and Schanll, M. D. Magnetization transfer: theory and clinical applications in neurology. *RadioGraphics*, 14:279–290, 1994.

[51] Santos, A. C., Narayanan, S., de Stefano, N., Tartaglia, M. C., Francis, S. J., Arnaoutelis, R., Caramanos, Z., Antel, J. P., Pike, G. B. and Arnold, D. L. Magnetization transfer can predict clinical evolution in patients with multiple sclerosis. *J. Neurol.*, 249(6):662–668, 2002.

[52] Dixon, T. W., Engels, H., Castillo, M. and Shardhasti, M. Incidental Magnetization Transfer in Standard Multislice Imaging. *Magn. Reson. Imaging*, 8:417–422, 1990.

[53] Melki, P. S. and Mulkern, R. V. Magnetization Transfer Effects in Multislice RARE sequences. *Magn. Reson. Med.*, 24:189–195, 1992.

[54] Shin, W., Go, H. and Yang, Y. Incidental Magnetization Transfer Contrast by Fat Saturation Preparation Pulses in Multislice Look-Locker Echo Planar Imaging. *Magn. Reson. Med.*, 62:520–526, 2009.

[55] Helms, G. and Piringer, A. Dynamic evaluation of magnetization transfer (MT) in human brain: the approach to steady state after pulsed saturation. *6th Scientic Meeting of the International Society for Magnetic Resonance in Medicine*, page 2192, 1998.

[56] Gloor, M. *Magnetization Transfer Imaging Using Steady-State Free Precession MR Sequences*. PhD thesis, Philosophisch-Naturwissenschaftlichen Fakultt der Universitt Basel, 2010.

[57] Henkelman, R. M., Stanisz, G. J. and Graham, S. J. Magnetization transfer in MRI: a review. *NMR Biomed.*, 14:57–64, 2001.

[58] de Boer, R. W. Magnetization transfer contrast. Part 1: MR Physics. *Philips Medical Systems MedicaMundi*, 40:60–73, 1995.

[59] Stoeck, C. T., Hu, P., Peters, D. C., Kissinger, K. V., Goddu, B., Goepfert, L., Ngo, L., Manning, W. J., Kozerke, S. and Nezafat, R. Optimization of On-Resonant Magnetization Transfer Contrast in Coronary Vein MRI. *Magn. Reson. Med.*, 64(6):1849–1854, 2010.

[60] Forster, J., Schick, F., Pfeffer, M. and Lutz, O. Magnetization transfer by simple sequences of rectangular pulses. *MAGMA*, 3(2):83–93, 1995.

[61] Pike, G. B., Glover, G. H., Hu, B. S. and Enzmann, D. R. Pulsed magnetization transfer spin echo MR imaging. *J. Magn. Reson. Imaging*, 3(3):531–539, 1993.

[62] Schick, F., Forster, J., Pfeffer, M. and Lutz, O. Pulsed magnetization transfer for imaging and spectroscopic applications on whole-body imagers. *MAGMA*, 2(2):10, 1994.

[63] Stark, D. D. *Magnetic resonance imaging, Volume one.* 2nd ed. Mosby, St Louis, Missouri, 1992.

[64] Felmlee, J. P. andEhman, R. L. Spatial presaturation: a method for suppressing flow artifacts and improving depiction of vascular anatomy in MR imaging. *Radiology*, 164:559–564, 1987.

[65] Ogawa, S., Lee, T. M., Kay, A. R. and Tank, D. W. Brain magnetic resonance imaging with contrast dependent on blood oxygenation. *Proc. Natl. Acad. Sci. USA*, 87(24):9868–9872, 1990.

[66] Bandettini, P. A., Wong, E. C., Hinks, R. S., Tikofsky, R. S. and Hyde, J. S. Time course EPI of human brain function during task activation. *Magn. Reson. Med.*, 25:390–397, 1992.

[67] Ogawa, S., Tank, D., Menon, R., Ellermann, J.M., Kim, S.-G., Merkle, K. and Ugurbil, K. Intrinsic signal changes ac- companying sensory stimulation: functional brain mapping using MRI. *Proc. Natl. Acad. Sci. USA*, 89:5951–5955, 1992.

[68] Kim, S. G., Ashe, J., Georgopoulos, A. P., Merkle, K., Ellermann, J. M., Menon, R. S., Ogawa, S. and Ugurbil, K. Functional imaging of human motor cortex at high magnetic field. *J. Neurophysiol.*, 69:297–302, 1993.

[69] Schneider, W., Noll, D. G. and Cohen, J. G. Functional topographic mapping of the cortical ribbon in human vision with conventional MRI scanners. *Nature*, 365:150–153, 1993.

[70] McCarthy, G., Blamire, A.M., Rothman, D.L., Gruetter, R. and Shulman, R.G. Echo-planar MRI studies of frontal cortex activation during word generation in humans. *Proc. Natl. Acad. Sci. USA*, 90:4952–4956, 1993.

[71] Raichle, M. E. Circulatory and metabolic correlates of brain function in normal humans. In: Handbook of physiology-the nervous system. *Bethesda: American Physiological Society*, 5:643–674, 1987.

[72] Norris, D. G. Principles of magnetic resonance assessment of brain function. *J. Magn. Reson. Imaging*, 23(6):794–807, 2006.

[73] Pivarc, J. *Application of the Multiple Quantum NMR Spectroscopy for Investigation of the Dipole-Dipole Couplings in Amorphous Polymers.* PhD thesis, Mathematisch-Naturwissenschaftlich-Technischen Fakulta t der Martin-Luther-Universit at Halle-Wittenberg, 2000.

[74] Reich, H. J. 8.2 The Nuclear Overhauser Effect,.

[75] Noggle, J. H. and Schirmer, R. E. *The Nuclear Overhauser Effect. Chemical Applications.* InTech, 2012.

[76] Kwan, E. The nuclear overhauser effect, March 2011. University Lecture.

[77] Solomon, I. Relaxation Processes in a System of Two Spins. *Phys. Rev.*, 99(2):559–565, 1955.

[78] Palmer, A. G. *Relaxation and Dynamic Processes. In Cavanagh, J., W. J. Fairbrother, A. G. Palmer and N. J. Skelton: Protein NMR Spectroscopy: Principles and Practice.* Academic Press, 2007.

[79] Ohanian, H. C. What is spin? . *Am. J. Phys.*, 54:500–505, 1986.

[80] Weil, J. A. and Bolton, J. R. *Electron Paramagnetic Resonance.* Second Edition, John Wiley & Sons, Inc, 2007.

[81] Lurie, D. J. Free radical imaging. *The British Journal of Radiology*, 74:782–784, 2001.

[82] Vikram, D. S., Rivera, B. K. and Kuppusamy, P. *In Vivo Imaging of Free Radicals and Oxygen. In Uppu, R. M., Murthy, S. N., Pryor, W. A. and Parinandi, N. L. :Free Radicals and Antioxidant Protocols*, volume 610. Humana Press, 2009.

[83] Goez, M. *Photo-CIDNP Spectroscopy. In David Cheresh: Annual Reports on NMR SPectroscopy, Volume 66.* Elsevier, 2009.

[84] Ward, H. R. and Lawler, R. G. Nuclear Magnetic Resonance emission and enhanced absorption in rapid organometallic reactions. *J. Am. Chem. Soc.*, 89:5518–5519, 1967.

[85] Kaptein, R., Dijkstra, K. and Nicolay, K. Laser photo-CIDNP as a surface probe for proteins in solution. *Nature*, 274:293–294, 1978.

[86] Kaptein, R. and Oosterhoff, J. L. Chemically Induced Dynamic Nuclear polarization II (relation with anomalous ESR spectra). *Chem. Phys. Lett.*, 4:195, 1968.

[87] Krishna, M. C., English, S., Yamada, K., Yoo, J., Murugesan, R., Devasahayam, N., Cook, J. A., Golman, Kerkjaer-Larsem, J. H., Subramanian, S. and Mithell, J. B. Overhauser enhanced magnetic resonance imaging for tumor oxymetry: Coregistration of tumor anatomy and tissue oxygen concentration. *Chem. Phys. Lett.*, 99(4):2216–2221, 2001.

[88] Sarracanie, M., Armstrong, B. D., Stockmann, J. and Rosen, J. M. High Speed 3D Overhauser-Enhanced MRI using Combined b-SSFP and Compressed Sensing. *Mag. Res. in Med.*, 71(2):735–745, 2014.

[89] Friston, K. J., Frith, C. D., Liddle, P. F., Lammerstma A. A. and Frackowiak, R. S. J. The relationship between global and local changes in PET scans. *J. Cereb. Blood Flow Metab.*, 10:458–466, 1990.

[90] Cox, R. W. AFNI: Software for analysis and visualization of functional magnetic resonance neuroimages. *Computers and Biomedical Research*, 29:162–173, 1996.

[91] Lopes da Silva, F. H., Storm van Leeuwen, W. and Rmond, A. *Handbook of Electroencephalography and Clinical Neurophysiology. Volume 2: Clinical Applications of Computer Analysis of EEG and other Neurophysiological Signals.* Elsevier, Amsterdam, 1986.

[92] Keller, K. and Sinn, M. Ordinal analysis of time series. *Physica A*, 356:114–120, 2005.

[93] Acharya, U. R., Faust, O. and Kannathal, N. Non-linear analysis of EEG signals at various sleep stages. *Comput. Methods Programs Biomed.*, 80(1):37–45, 2005.

[94] Parlitz, U., Berg, S., Luther, S., Schirdewan, A., Kurths, J. and Wessel., N. Classifying cardiac biosignals using ordinal pattern statistics and symbolic dynamics. *Computers in Biology and Medicine*, 42:319–327, 2012.

[95] Hostalkova, E. and Prochazka, A. Wavelet Signal and Image Denoising. *Institute of Chemical Technology, Prague Department of Computing and Control Engineering Technichques*, 2009.

[96] Mallat, S. A wavelet tour of signal processing. *Academic Press, New York.*, 1998.

[97] Lang, M., Guo, H., Odegard, J. E., Burrus, C. S. and Wells, R. O. Jr. Noise Reduction Using an Undecimated Discrete Wavelet Transform. *IEEE Signal Processing Letters*, 3:10–12, 1996.

[98] Simoncelli, E. P. and Adelson, E. H. Noise removal via Bayesian wavelet coring, IEEE. *Signal Processing Letters, IEEE*, 1996.

[99] Jansen, M. *Noise reduction by wavelet thresholding.* Springer, USA, 2001.

[100] Ergen, B., Tatar, Y. and Gulcur, H. O. Time-frequency analysis of phonocardiogram signals using wavelet transform: a comparative study. *Signal Processing Letters, IEEE*, 15(4):371–381, 2011.

[101] Moulin, P. and Liu, J. Analysis of multiresolution image denoising schemes using generalized Gaussian and complexity prior. *Information Theory, IEEE Transaction*, 45(3):909–919, 1999.

[102] Alfaouri, M. and Daqrouq, K. ECG signal denoising by wavelet transform thresholding. *American Journal of Applied Sciences*, 5(3):276–281, 2008.

[103] Ergen, B. *Signal and image denoising using wavelet transform, advances in wavelet theory and their applications in engineering, physics and technology.* Dr. Dumitru Baleanu (Ed.) ISBN: 978-953-51-0494-0. In Tech.

[104] Donoho, D. L. and Johnstone, I. M. Ideal Spatial Adaptation by Wavelet Shrinkage. *Biometrika*, 81:425–455, 1994.

[105] Hyvärinen, A. and Oja, E. Independent Component Analysis: Algorithms and Applications. *Neural Networks*, 13(4):411–430, 2000.

[106] Jutten, C. and Hrault, J. Blind separation of sources, part I: An adaptive algorithm based on neuromimetic architecture. *Signal Processing*, 24:1–10, 1991.

[107] Bell, A. J. and Sejnowski, T. J. An information maximisation approach to blind separation and blind deconvolution. *Neural Computation*, 7(6):1129–1159, 1995.

[108] Hyvrinen, A. Fast and robust fixed-point algorithms for independent component analysis. *IEEE Transactions on Neural Networks*, 10(3):626–634, 1999.

[109] Back, A. D. and Weigend, A. S. A first application of independent component analysis to extracting structure from stock returns. *Int. J. on Neural Systems*, 8(4):473–484, 1997.

[110] Bell, A. J. and Sejnowski, T. J. The independent components of natural scenes are edge filters. *Vision Research*, 37:3327–3338, 1997.

[111] Johnson, M., Yuan, X. and Ren, Y. Speech Signal Enhancement through Adaptive Wavelet Thresholding. *Biometrika*, 49(2):123–133, 2007.

[112] de Pasquale, F., Penna, S. D., Snyder, A. Z., Lewis, C., Mantini, D., Marzetti, L., Belardinelli, P., Ciancetta, L., Pizzella, V., Romani, G. L. and Corbetta, M. Temporal dynamics of spontaneous MEG activity in brain networks. *Proc. Natl. Acad. Sci. U.S.A.*, 107:6040–6045, 2010.

[113] Kiviniemi, V., Kantola, J. H., Jauhiainen, J., Hyvarinen A. and Tervonen, O. Independent component analysis of nondeterministic fMRI signal sources. *Neuroimage*, 19:253–260, 2003.

[114] van de Ven, V. G., Formisano, E., Prvulovic, D., Roeder, C. H. and Linden, D. E. Functional connectivity as revealed by spatial independent component analysis of fMRI measurements during rest. *Hum. Brain Mapp.*, 22:165–178, 2004.

[115] Bartels, A. and Zeki, S. The chronoarchitecture of the human brainnatural viewing conditions reveal a time-based anatomy of the brain. *NeuroImage*, 22:419–433, 2004.

[116] Hasson, U., Nir, Y., Levy, I., Furhmann, G. and Malach, R. Intersubject synchronization of cortical activity during natural vision. *Science*, 303:1634–1640, 2004.

[117] Naik, G. R. and Kumar, D. K. An Overview of Independent Component Analysis and Its Applications. *Informatica*, 35:63–81, 2009.

[118] Hansen, L. K., Larsen, J. and Kolenda, T. Blind Detection of Independent Dynamic Components. *In proc. IEEE ICASSP'2001*, 5:3197–3200, 2001.

[119] Pham, D. T., Garrat, P. and Jutten, C. Separation of a mixture ofindependent sources through a maximum likelihood approach. *Proc. EUSIPCO*, pages 771–774, 1992.

[120] Papoulis, A. *Probability, Random Variables, and Stochastic Processes.* McGraw-Hill, 3rd edition, 1991.

[121] Von Luxburg U. A Tutorial on Spectral Clustering. *Statistics and Computing*, 17(4):1–32, 2007.

[122] Chung, F. Spectral graph theory (Vol. 92 of the CBMS Regional Conference Series in Mathematics). *Conference Board of the Mathematical Sciences, Washington.*, 1997.

[123] Shi, J. and Malik, J. Normalized cuts and image segmentation. *IEEE Transactions on Pattern Analysis and Machine Intelligence*, 22(8):888–905, 2000.

[124] Hastie, T., Tibshirani, R. and Friedman, J. *The elements of statistical learning.* Springer, 2001.

[125] Ng, A., Jordan, M. and Weiss, Y. On spectral clustering: analysis and an algorithm. In T. Dietterich, S. Becker, and Z. Ghahramani (Eds.), Advances in Neural Information Processing Systems 14 (pp. 849 –856). MIT Press. 2002.

[126] Mandelbrot, B. *Fractals. Form, Chance and Dimension.* Freeman (Eds), 1977.

[127] Rybaczuk, M., Kedzia, A. and Blaszyk, E. Fractal description of the cerebellum surface during fetal period. *Folia Morphologica*, 55(4):434–436, 1996.

[128] Iftekharuddin, K., Jia, W. and Marsh, R. A fractal analysis approach to identification of tumor in brain MRI images. *Conference of the IEEE Engineering in Medicine and Biology Society.*, 4:3064–3066, 2000.

[129] Zhang, L., Dean, D., Liu, J., Sahgal, V, Wang, X. and Yue, G. Quantifying degeneration of white matter in normal aging using fractal dimension. *Neurobiology of Aging.*, 28(10):1543–1555, 2006.

[130] Ihlen, E. A. F. Introduction to multifractal detrended fluctuation analysis in Matlab. *Front . Physiol.*, 3(141):1–18, 2012.

[131] Goldberger, A. L., Amaral, L. A., Hausdorff, J. M., Ivanov, P. C., Peng, C. K. and Stanley, H. E. Fractal dynamics in physiology: alterations with disease and aging. *Proc. Natl. Acad. Sci.*, 99:2466–2472, 2002.

[132] Suckling, J., Wink, A. M., Bernard, F. A., Barnes, A. and Bullmore, E. Endogenous multifractal brain dynamics are modulated by age, cholinergic blockade and cognitive performance. *J. Neuros. Methods*, 174:2466–2472, 2008.

[133] Ciuciu, P., Varoquaux, G., Abry, P., Sadaghiani, S. and Kleinschmidt A. Scale-free and multifractal time dynamics of fMRI signals during rest and task. *Front. Physiol.*, 3:186, 2012.

[134] Qianli, M. A., Xibao, N., Jun, W. and Chunhua, B. A new measure to characterize multifractality of sleep electroencephalogram. *Chinese Science Bulletin*, 51(24):3059–3064, 2006.

[135] Zheng, Y., Gao, J. B., Sanchez, J. C., Principe, J. C. and Okun, M. Multiplicative multifractal modeling and discrimination of human neuronal activity. *Phys. Lett. A*, 344:253–264, 2005.

[136] Soares, F., Sousa, I., Janela, F., Seabra, J., Pereira, M. and Freire, M. M. Multifractal analysis of arterial spin labeling functional magnetic resonance imaging of the brain. *Proc. IEEE International Workshop on Medical Measurements and Application Proceedings , NY , United States*, 1:161–164., 2010.

[137] Makowiec, D., Rynkiewicz, A., Wdowczyk-Slulc, J. and Zarczynska-Buchowiecka, M. On reading multifractal spectra. Multifracta age for healthy aging humans by analysis of cardiac interbeat time intervals. *Acta Phys. Pol. B*, 5:159–170., 2011.

[138] Dick, O. E. and Svyatogor, I. A. Potentialities of the wavelet and multifractal techniques to evaluate changes in the functional state of the human brain. *Neurocomputing*, 82:207–215, 2012.

[139] Kantelhardt, J. W., Zschiegner, S. A., Koscielny-Bunde, E., Havlin, S., Bunde, A. and Stanley, H. E. Multifractal detrended fluctuation analysis of nonstationary time series. *Physica A.*, 316:87–114, 2002.

[140] Pignat, J. M, Koval, O., Van De Ville, D., Voloshynovskiy, S., Michel, C., Pun, T. The impact of denoising on independent component analysis of functional magnetic resonance imaging data. *Journal of Neuroscience Methods,*, 213:105–122, 2013.

[141] Gomes, E. F. and Pereira, E. Classifying heart sounds using peak location for segmentation and feature construction. *Manuscript*, 2013.

[142] Lindsten, F. A remark on zero-padding for increased frequency resolution. 2010.

[143] de Broglie, L. La mcanique ondulatoire et la structure atomique de la matire et du rayonnement. *Journal de Physique et le Radium*, 8(5):225–241, 1927.

[144] Larsen, E. A. *Classification of EEG Signals in a Brain-Computer Interface System.* PhD thesis, Norwegian University of Science and Technology, Department of Computer and Information Science, 2011.

[145] Niedermeyer, E. and Lopes da Silva, F. *Electroencephalography: Basic Principles, Clinical Applications, and Related Fields.* 5th ed. Baltimore: Williams & Wilkins, 1993.

[146] Monro, A. Observations on structure and functions of the nervous system. . *Edinburgh: Creech and Johnson*, 1783.

[147] Mokri, B. The Monro-Kellie hypothesis: applications in CSF volume depletion. *Neurology*, 56(12):1746–1748, 2001.

[148] McKeown, M. J., Hansen, L. K. and Sejnowski, T. J. Independent component analysis of functional MRI: what is signal and what is noise? *Curr Opin Neurobiol.*, 13(5):620–629, 2010.

[149] McKeown, M. J., Jung, T. P., Scott, M., Brown, G., Kindermann, S. S. and Sejnowski, T. J. Spatially independent activity patterns in functional MRI data during the Stroop color-naming task. *Proc. Natl. Acad. Sci. USA*, 95:803–810, 1998.

[150] Greitz, D., Wirestam, R., Franck, A., Nordell, B., Thomsen, C. and Stahlberg, F. Pulsatile brain movement and associated hydrodynamics studied by magnetic resonance phase imaging. The Monro-Kellie doctrine revisited. *Cereb. Cortex*, 34(5):370–380, 1992.

[151] Nunes, R. G., Jezzard, P. and Clare, S. Investigations on the efficiency of cardiac-gated methods for the acquisition of diffusion-weighted images. *J. Magn.. Reson.*, 177(1):102–110, 2005.

[152] Bottomley, P. A., Foster, T. H., Argersinger, R. E. and Pfeiffer, L. M. A review of normal tissue hydrogen NMR relaxation times and relaxation mechanisms from

1100 MHz: Dependence on tissue type, NMR frequency, temperature, species, excision, and age. *Med. Phys.*, 11:425 – 448, 1984.

[153] Traficante, D. D. Relaxation Can T_2 be longer than T_1? *Concepts in Magnetic Resonance*, 3:171–177, 1991.

[154] Logothetis, N. K. and Wandell, B. A. Interpreting The Bold Signal. *Annu. Rev. Physiol.*, 66(1):735–769, 2004.

[155] Renvall, V., Nangini, C. and Hari, R. All that glitters is not BOLD: inconsistencies in functional MRI. *AJNR Am. J. Neuroradiol.*, 29:4:3920, 2014.

[156] Solsona-Sancho, C. and Blasi-Cabus, J. M. Neuronal membrane and aging. Electrophysiological aspects. *Rev. Neurol.*, 29(11):1083–1088, 1999.

[157] Jernigan, T .L., Archibald, S. L., Berhow, M. T., Sowell, E. R., Foster, D. S. and Hesselink, J. R. Cerebral structure on MRI, part I: localization of age-related changes. *Biol. Psychiatry*, 29:55–67, 1991.

[158] Salat, D. H., Buckner, R. L., Snyder, A. Z., Greve, D. N., Desikan, R. S., Busa, E., Morris, J. C., Dale, A. M. and Fisch, B. Thinning of the cerebral cortex in aging. *Cereb. Cortex*, 14(7):721–730, 2004.

[159] Sabayan, B., van Buchem, M. A., Sigurdsson, S., Zhang, Q., Harris, T. B., Gudnason, V., Arai, A. E. and Launer, L. J. Cardiac Hemodynamics are Linked With Structural and Functional Features of Brain Aging: The Age, Gene/Environment Susceptibility (AGES)Reykjavik Study. *J. Am. Heart Assoc.*, (4):1–11, 2015.

[160] Iadecola, C. and Davisson, R. L. Hypertension and cerebrovascular dysfunction. *Cell. Metab.*, 7(6):476–484, 2008.

[161] Ueno, M., Tomimoto, H., Akiguchi, I., Wakita, H. and Sakamoto, H. Blood-brain barrier disruption in white matter lesions in a rat model of chronic cerebral hypoperfusion. *J. Cereb. Blood. Flow Metab.*, 22:97–104, 2002.

[162] Farkas, E., Luiten, P. G. and Bari, F. Permanent, bilateral common carotid artery occlusion in the rat: a model for chronic cerebral hypoperfusionrelated neurodegenerative diseases. *Brain.Res. Rev.*, 54:162–180, 2007.

[163] Yoshizaki, K., Adachi, K., Kataoka, S., Watanabe, A., Tabira, T., Takahashi, K. and Wakita, H. Chronic cerebral hypoperfusion induced by right unilateral common carotid artery occlusion causes delayed white matter lesions and cognitive impairment in adult mice. *Exp. Neurol.*, 210:585–591, 2008.

[164] Shibata, M., Yamasaki, N., Miyakawa, T., Kalaria, R. N., Fujita, Y., Ohtani, R., Ihara, M., Takahashi, R and Tomimoto, H. Selective impairment of working memory in a mouse model of chronic cerebral hypoperfusion. *Stroke*, 38:2826–2832, 2007.

[165] Sowell, E. R., Thompson, P. M. and Toga, A. W. Mapping changes in the human cortex throughout the span of life. *Neuroscientist*, (10):372–392, 2004.

[166] Ziegler, D. A., Piguet, O., Salat, D. H., Prince, K., Connally, E. and Corkin, S. Cognition in healthy aging is related to regional white matter integrity, but not cortical thickness. *Neurobiol. Aging*, 31(11):1912–1926, 2008.

[167] Liu, Y., Zhu, X., Feinberg, D., Guenther, M., Gregori, J., Weiner, M. W. and Schuff, N. Arterial spin labeling MRI study of age and gender effects on brain perfusion hemodynamics. *Magn. Reson. Med.*, 68(3):912–922, 2012.

[168] Mitra, P. Chronux website. http://chronux.org, 2015. Accessed: 2015-08-05.

[169] Mitra, P. and Bokil, H. *Observed Brain Dynamics*. Oxford University Press, New York, 2008.

[170] Press, W. H., Teukolsky, S. A., Vetterling, W. T and Flannery, B. P. *Section 13.4.3. Multitaper Methods and Slepian Functions*. Numerical Recipes: The Art of Scientific Computing (3rd ed.), New York: Cambridge University Press.

[171] Lin, T. Physiology of the circulation. *in Fundamentals of Anaesthesia, eds Pinnock C., Lin T., Smith T., editors. (London: Greenwich Medical Media;),*, pages 331–360, 1999.

[172] Hayen, A., Herigstad, M., Kelly, M., Okell, T. W., Murphy, K., Wise, R. G. et al. The effects of altered intrathoracic pressure on resting cerebral blood flow and its response to visual stimulation. *Neuroimage*, 66:479–488, 2012.

[173] Raj, D., Anderson, A. W. and Gore, J. C. Respiratory effects in human functional magnetic resonance imaging due to bulk susceptibility changes. *Phys. Med. Biol.*, 46:3331–3340, 2001.

[174] Wise R. G., Ide K., Poulin M. J., Tracey I. Resting fluctuations in arterial carbon dioxide induce significant low frequency variations in BOLD signal. *Neuroimage*, 21:1652–1664, 2004.

[175] Videbech, P. PET measurements of brain glucosemetabolism and blood flow in major depressive disorder: a critical review. *Acta Psychiatr. Scand.*, 101:10–20, 2000.

[176] Shah, S. A., Doraiswamy, P. M., Husain, M. M. et al. Posterior fossa abnormalities in major depression: a controlled magnetic resonance imaging study. *Acta Psychiatry Scand.*, 85:474–479, 1992.

[177] Dolan, R. J., Calloway, S. P., Thacker, P. F. and Mann, A. H. The cerebral cortical appearance in depressed subjects. *Psychol. Med.*, 16:775–779, 1986.

[178] Rabins, P. V., Pearlson, G. D., Aylward, E., Kumar, A. J. and Dowell, J. Cortical magnetic resonance imaging changes in elderly in patients with major depression. *Am. J. Psychiatry*, 148:617–620, 1991.

[179] Drevets, W. C., Videen, T. O., Price, J. L., Preskorn, S. H., Carmichael, S. T. and Raichle, M. E. A functional anatomical study of unipolar depression. *Arch. Gen. Psychiatry*, 12:3628–3541, 1992.

[180] Baxter, L. R. J., Phelps, M. E, Mazziotta, J. C. et al. Cerebral metabolic rates for glucose in mood disorders: studies with positron emission tomography and Fluorodeoxyglucose F18. *Arch. Gen. Psychiatry*, 42:441–447, 1985.

[181] Rogers, M. A., Bradshaw, J. L., Pantelis, C. et al. Frontaostriatal deficits in unipolar major depression. *Brain Res. Bull.*, 47:297–310, 1998.

[182] Elliott, R., Baker, S. C., Rogers, R. P. et al. Pre-frontal dysfunction in depressed patients performed a complexed planning task: a study using positron imaging tomography. *Psychol. Med.*, 27:931–942, 1997.

[183] Baumann, B., Danos, P., Krell, D. et al. Reduced volume of limbic system-affiliated basal ganglia in mood disorders: preliminary data from a postmortem study. *J. Neuropsychiatry*, 11:71–8, 1999.

[184] Koenigs, M. and Grafman, J. The functional neuroanatomy of depression: Distinct roles for ventromedial and dorsolateral prefrontal cortex. *Behav. Brain Res.*., 201(2):239–243, 2009.

[185] Buxton, R. B., Wong, E. C. and Frank, L. R. Dynamics of blood flow and oxygenation changes during brain activation: the balloon model. *Magn. Reson. Med.*, 39:855–864, 1998.

[186] Kwong, K. K., Belliveau, J. W., Chesler, D. A., Goldberg, I. E., Weisskoff, R. M., Poncelet, B. P., Kennedy, D. N., Hoppel, B. E., Cohen, M. S., Turner, R. Dynamic magnetic resonance imaging of human brain activity during primary sensory stimulation. *Proc. Natl. Acad. Sci. USA*, 89:5675–5679, 1992.

[187] Buxton, R. B. and Frank, L. R. A model for the coupling between cerebral blood flow and oxygen metabolism during neural stimulation. *J. Cereb. Blood Flow Metab.*, 17:64–72, 1997.

[188] Kundu, P., Inati, S. J., Evans, J. W., Luh, W. M. and Bandettini, P. A. Differentiating BOLD and non-BOLD signals in fMRI time series using multi-echo EPI. *NeuroImage*, 60:1759–1770, 2012.

[189] Bright, M. G. and Murphy, K. Reliable quantification of BOLD fMRI cerebrovascular reactivity despite poor breath-hold performance. *NeuroImage*, 83:559–568, 2013.

[190] Lombardi, F., and Parati, G. An update on: cardiovascular and respiratory changes during sleep in normal and hypertensive subjects. *Cardiovasc. Res.*, 45(1):200–211, 2000.

[191] Sayk, F., Becker, C., Teckentrup, C., Fehm, H. L., Struck, J., Wellhoener, J. P. and Dodt, C. To Dip or Not to Dip. On the Physiology of Blood Pressure Decrease During Nocturnal Sleep in Healthy Humans. *Hypertension*, 49(5):1070–1076, 2007.

[192] Guggisberg, A. G., Mathis, J., Herrmann, U. S. and Hess, C. W. The functional relationship between yawning and vigilance. *Behav. Brain Res.*, 179(1):159–166, 2007.

[193] Friston, K., Ashburner, J., Kiebel, S., Nichols, T. and Penny, W. *Statistical Parametric Mapping*. Elsevier Ltd, 2007.

[194] Wildey, C. and MacFarlane, D. Head tracking for real-time motion correction in the MRI environment using a single camera. *Optics InfoBase Conference Papers. Optical Society of America*, 2009.

[195] Bench, C. J., Friston, K. J., Frackowiak, R. S. and Dolan, R. J. Regional cerebral blood flow in depression measured by positron emission tomography: the relationship with clinical dimensions. *Psychol. Med.*, 23:579–590, 1993.